CFD ANALYSIS OF THE FLOW OVER THE WING EQUIPPED WITH PASSIVE HIGH-LIFT DEVICES

Master's Degree in Aeronautical Engineering

Final Master's Degree Thesis

By:
Pablo Guillermo Cid Escobar - pabcies@etsid.upv.es

First external director (Universitatea Politehnica din București):
Marius Stoia-Djeska

UPV director (Universitat Politècnica de València):
Sergio Hoyas Calvo

04/06/2021

Acknowledgements

I want to express my gratitude first of all to my parents for the education they have instilled in me, to Marius Stoia-Djeska for giving me the opportunity to do this work, to Sergio Hoyas Calvo for being my UPV tutor, to thank my classmates that I have had during the two years of the master's degree, to Marius Gabriel Cojocaru and the CONVERGE CFD support team, the Universitat Politècnica de València professors for the learning that I have had and finally the Universitatea Politehnica din București for giving me the opportunity to study in the Erasmus+ program.

Abstract

This master's thesis is focused on the study of the flow over the wing equipped with passive high-lift devices. It starts with a 2D study and continues with a 3D study. The 2D study has been done by means of numerical CFD (Computational Fluid Dynamics) simulations using CONVERGE CFD. The 3D study was carried out using FlightStream software. The objective of the work is to improve the configuration of an airfoil with passive high-lift leading and trailing edge devices for take-off and finally to equip these devices to a wing.

Contents

Acknowledgments **I**

Abstract **III**

List of Figures **VII**

List of Tables **XI**

List of Acronyms **XIII**

1 Introduction **1**

2 Objectives **5**

3 Previous work **7**

4 Method **13**

4.1 2-D analysis 13
  4.1.1 Numerical simulation 13
  4.1.2 RANS model used 14
  4.1.3 Characteristics of the airfoil and passive high-lift devices 16
  4.1.4 Description of the mesh 19
    4.1.4.1 Initial conditions 19
    4.1.4.2 Boundary conditions 20
    4.1.4.3 Grid control 22
    4.1.4.4 Convergence process 24
    4.1.4.5 Validation of results 27
4.2 3-D analysis 31
  4.2.1 Numerical simulation 31
  4.2.2 Wing characteristics 31
  4.2.3 Description of the mesh 32

5 Results **35**

5.1 2-D analysis 35

5.1.1 High-lift trailing edge devices 35
5.1.2 High-lift leading edge devices 38
5.2 3-D analysis 42

6 Conclusions 47

References 50

A Annex A: Use of the software 53

B Annex B: Coordinates of the airfoil and the high-lift devices 67

List of Figures

1 a) Passive high-lift trailing edge devices. b) Passive high-lift leading edge devices. Adapted image. [4] . . . 2
2 a) Contribution of the high-lift trailing edge devices. b) Contribution of the high-lift leading edge devices. [4] . . . 3
3 Bombardier CRJ-900 NG (CL-600-2D24) approaching runway. [6] . . . 4
4 Study flaps. [4] . . . 7
5 a) Contribution of flaps that do not extend. b) Contribution of flaps that extend. [4] . . . 8
6 NACA 0012 airfoil. [10] . . . 8
7 C_l comparison with turbulent models ($Re = 500000$). [9] . . . 9
8 C_d comparison with turbulent models ($Re = 500000$). [9] . . . 9
9 C_m comparison with turbulent models ($Re = 500000$). [9] . . . 10
10 Velocity representation (m/s), NACA0012 airfoil ($\alpha = 6°$). [9] . . . 10
11 Comparative graph C_l - α of the NACA 0012 airfoil with all study flaps. [9] 11
12 Comparative graph C_l - C_d of the NACA 0012 airfoil with all study flaps. [9] 12
13 NACA 0012 airfoil with a plain flap (20%c 20°). . . . 17
14 NACA 0012 airfoil with a plain flap (30%c 15°). . . . 17
15 NACA 0012 airfoil with a plain flap (40%c 10°). . . . 17
16 NACA 0012 airfoil with a leading edge flap (15%c 20°) and a plain flap (20%c 20°). . . . 18
17 NACA 0012 airfoil with a leading edge flap (20%c 15°) and a plain flap (20%c 20°). . . . 18
18 NACA 0012 airfoil with a leading edge flap (25%c 10°) and a plain flap (20%c 20°). . . . 19
19 Five problem zones. . . . 21
20 Boundary layer. [17] . . . 23
21 Pressure Forces X (NACA 0012. Base Grid=9m, Embed Scale=13). . . . 25
22 Pressure Forces Y (NACA 0012. Base Grid=9m, Embed Scale=13). . . . 25
23 Mesh used. . . . 27
24 Comparison of C_l values. . . . 28

25 Comparison of C_d values. 29
26 Comparison of C_m values. 29
27 NACA0012 airfoil ($\alpha = 10°$). a) Velocity representation (m/s). b) Pressure representation (Pa). c) Turbulent viscosity representation (m^2/s). 30
28 Wing measurements in CatiaV5. 31
29 Wing mesh in FlightStream. 33
30 Comparison of the C_l values. Analysis of the different high-lift trailing edge devices. 35
31 Comparison of the C_d values. Analysis of the different high-lift trailing edge devices. 36
32 Comparison of the C_m values. Analysis of the different high-lift trailing edge devices. 37
33 NACA0012 airfoil with a plain flap 20%c 20° ($\alpha = 10°$). a) Velocity representation (m/s). b) Pressure representation (Pa). c) Turbulent viscosity representation (m^2/s). 38
34 Comparison of the C_l values. Analysis of the different high-lift leading edge devices. 39
35 Comparison of the C_d values. Analysis of the different high-lift leading edge devices. 40
36 Comparison of the C_m values. Analysis of the different high-lift leading edge devices. 40
37 NACA0012 airfoil with a leading edge flap 15%c 20° and with a plain flap 20%c 20° ($\alpha = 10°$). a) Velocity representation (m/s). b) Pressure representation (Pa). c) Turbulent viscosity representation (m^2/s). 41
38 Wing results with undeflected high-lift devices. 42
39 Residuals of the wing with undeflected high-lift devices case. 43
40 Wing results with deflected high-lift devices. 43
41 Residuals of the wing with deflected high-lift devices case. 44
42 Comparative C_L - C_D graph of the wing with deflected and undeflected high-lift devices. 44
43 Wing with undeflected high-lift devices in FlightStream. Velocity representation (m/s). ($\alpha = 10°$). 45

44 Wing with deflected high-lift devices in FlightStream. Velocity representation (m/s). ($\alpha = 10°$). . . . 45

45 Velocity representation (m/s). . . . 46

46 Reduction of vortex size with the use of winglets. [22] . . . 46

47 CAD created in CatiaV5. . . . 53

48 Airfoil imported into CONVERGE Studio. . . . 53

49 Geometry with the boundary conditions created in CONVERGE Studio. 54

50 Case setup creation in CONVERGE Studio. . . . 54

51 Materials options in CONVERGE Studio. . . . 55

52 Simulation parameters in CONVERGE Studio. . . . 55

53 Boundary conditions in CONVERGE Studio. . . . 56

54 Initial conditions in CONVERGE Studio. . . . 56

55 $k - \omega$ SST model parameters in CONVERGE Studio. . . . 57

56 Grid control (base grid, fixed embedding and grid scaling) in CONVERGE Studio. . . . 57

57 Grid control (adaptative mesh refinement) in CONVERGE Studio. . . . 58

58 Post variables and outputs in CONVERGE Studio. . . . 58

59 Final validation in CONVERGE Studio. . . . 59

60 Use of the *Diagnosis dock*. . . . 59

61 Use of the command window. . . . 60

62 Pressure Forces Y, NACA 0012. . . . 60

63 Obtaining the *.plt* files. . . . 61

64 Tecplot software. . . . 61

65 Wing obtained in CatiaV5. . . . 62

66 CAD of the wing in FlightStream. . . . 62

67 Configuring the trailing edge in FlightStream. . . . 63

68 Configuring wake termination nodes in FlightStream. . . . 63

69 Case configuration in FlightStream. . . . 64

70 Obtaining loads in FlightStream. . . . 64

71 Solver initialization in FlightStream. . . . 64

72 Velocity field around the wing for the angle of attack 10° in FlightStream. 65

73 Solving the case for different angles of attack in FlightStream. . . . 65

List of Tables

1 Plain flap configurations. 16
2 Leading edge flap configurations. 18
3 Some values of characteristic variables of the problem. 19
4 Values that are imposed in *Region 0* created. 20
5 Boundary conditions for the airfoil in CONVERGE CFD. 21
6 Boundary conditions for the inflow in CONVERGE CFD. 22
7 Boundary conditions for the outflow in CONVERGE CFD. 22
8 Convergence tolerances for the equations. 24
9 Convergence process of the base grid ($\alpha = 10°$, Embed Scale = 12). . . . 26
10 Convergence process of the embed scale ($\alpha = 10°$, Base grid = 9m). . . . 26
11 Characteristics of the mesh used. 26
12 Tessellation edge size analysis on the upper and lower surfaces ($\alpha = 10°$). 32
13 Tessellation edge size analysis on the wing edge ($\alpha = 10°$). 32
14 Wing tessellation edge sizes in FlightStream. 32
15 Coordinates of the NACA 0012 airfoil. 67
16 Coordinates of the NACA 0012 airfoil with a plain flap (20%c 20°). . . . 68
17 Coordinates of the NACA 0012 airfoil with a plain flap (30%c 15°). . . . 69
18 Coordinates of the NACA 0012 airfoil with a plain flap (40%c 10°). . . . 70
19 Coordinates of the NACA 0012 airfoil with a leading edge flap (15%c 20°) and a plain flap (20%c 20°). 71
20 Coordinates of the NACA 0012 airfoil with a leading edge flap (20%c 15°) and a plain flap (20%c 20°). 72
21 Coordinates of the NACA 0012 airfoil with a leading edge flap (25%c 10°) and a plain flap (20%c 20°). 73

List of Acronyms

- AMR: Adaptive mesh refinement.
- CAD: Computer-aided design.
- CFD: Computational Fluid Dynamics.
- DES: Detached Eddy Simulation.
- DNS: Direct Numerical Simulation.
- LES: Large Eddy Simulation.
- MPI: Message Passing Interface.
- NACA: National Advisory Committee for Aeronautics.
- PISO: Pressure Implicit with Splitting of Operator.
- RANS: Reynolds-Averaged Navier-Stokes.
- RNG: Renormalization Group.
- SIMPLE: Semi-Implicit Method for Pressure-Linked Equations.
- SST: Shear Stress Transport.

1 Introduction

A high-lift device is an aeronautical device designed to increase lift in certain phases of an aircraft's flight. The high-lift devices are divided into active and passive.

The additional wing lift contributed by high-lift devices is obtained through:

- Boundary layer control resulting from improved pressure distributions, reenergizing or removing low energy boundary layers (active high-lift devices).
- Increased airfoil camber (passive high-lift devices).
- An increment of the effective wing area in the case of flaps extending the chord when deflected (passive high-lift devices). [1]

On the one hand, the active high-lift devices increase lift with suction or blowing of the boundary layer. This process increases the amount of flow movement in the near zones of the airfoil surface, and thus the adverse pressure gradient that the boundary layer can withstand without sloughing is greater. By controlling the boundary layer, the maximum value of the lift coefficient, $C_{l\,\mathbf{max}}$, is increased, since the value of the angle of attack of the entry stall can be increased without detachment of the boundary layer. [2]

Also, the active high-lift devices can blow from the trailing edge. A separate blowing element or air from the motors is used. Bleed air from the engines is used for injection into the flap slots to increase the airspeed. The deflection of the flow over the trailing edge in the direction opposite to gravity produces an increase in lift. [2]

On the other hand, the passive high-lift devices are essentially movable elements that permit the pilot to change the geometry and aerodynamic characteristics of the wing sections to control the motion of the airplane or to improve the performance in some desired manner. [3]

The passive high-lift devices can be leading edge or trailing edge. When the high-lift trailing edge devices are deflected clockwise, the lift coefficient, drag coefficient and moment coefficient for the aerodynamic centre increase, with the increase of the moment coefficient in the dive direction. When deflected counterclockwise, the lift and dive moment coefficients decrease but also generate an increase in the aerodynamic drag coefficient. As the mechanical complexity of the high-lift elements increases, the increase in the lift coefficient is achieved with a smaller increase in the aerodynamic drag coefficient. [2]

The high-lift trailing edge devices do not increase the angle of stall. They tend to reduce the stall angle by increasing the pressure drop over the top of the airfoil, which promotes flow separation. To increase the stall angle, some form of leading edge device is required. In addition, the use of the leading edge devices generates an aerodynamic pitching moment, compensating for the diving moment generated by the trailing edge devices. [4]

Trailing edge devices include plain flaps, split flaps, slotted flaps, Fowler flaps... On the other hand, leading edge devices include leading-edge flaps, slots, slats, Krueger flaps... These devices are shown in Figure 1.

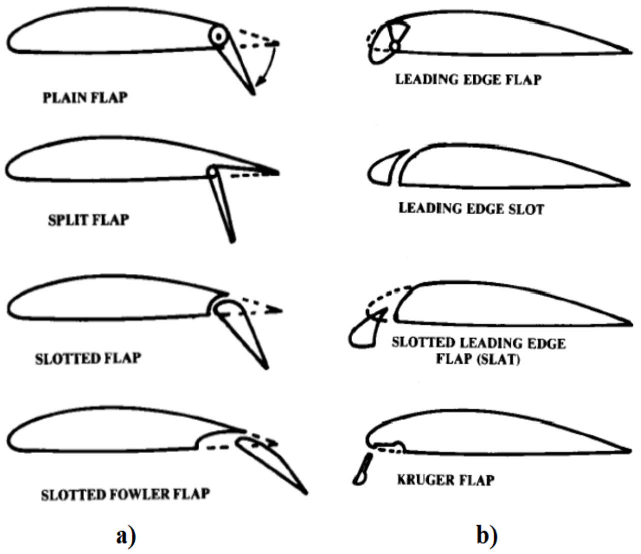

Figure 1: a) Passive high-lift trailing edge devices. b) Passive high-lift leading edge devices. Adapted image. [4]

Figure 2a shows the lift contribution of different high-lift trailing devices. It can be seen that the zero lift angle is reduced with the use of the plain flap. Besides, it can be seen that the use of the plain flap produces an increase in lift. However, when the airfoil has the plain flap deflected it stalls at a lower angle of attack. It should also be noted that the slope of the curve is maintained. Moreover, it can be seen that with the use of a slotted flap the stall angle increases.

On the other hand, Figure 2b shows the lift contribution of different high-lift leading devices. A leading-edge flap or slat delays the stall, but also has the effect of reducing the lift at a given angle of attack. This is because the droop in the leading edge acts as a reduction in the effective angle of attack as measured from the leading edge to the trailing edge. Leading-edge devices alone do little to improve lift for take-off and landing because they are effective only at fairly high angles of attack. Nevertheless, they are very useful when used in combination with trailing-edge flaps because they prevent premature airflow separation caused by the flaps.

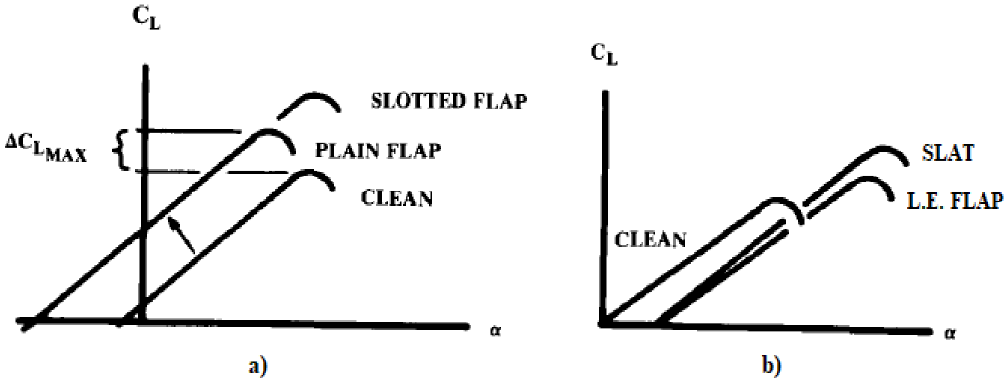

Figure 2: a) Contribution of the high-lift trailing edge devices. b) Contribution of the high-lift leading edge devices. [4]

The very beginning of high-lift can be traced back to the years 1917-1920, but even after 30 years, most of the design data were compiled in just four publications, but there was little understanding of the underlying aerodynamic principles at work. It was not until 1972 that the theoretical treatise of A.M.O. Smith provided a clear and comprehensive insight into the fundamentals of a multi-element foil. [5]

The majority of today's aircraft require the use of high-lift devices during take-off, approach and landing manoeuvres, as these are performed at low speeds, making it necessary to increase the lift coefficients of the airfoil. Figure 3 shows a Bombardier CRJ-900 NG aircraft approaching the runway.

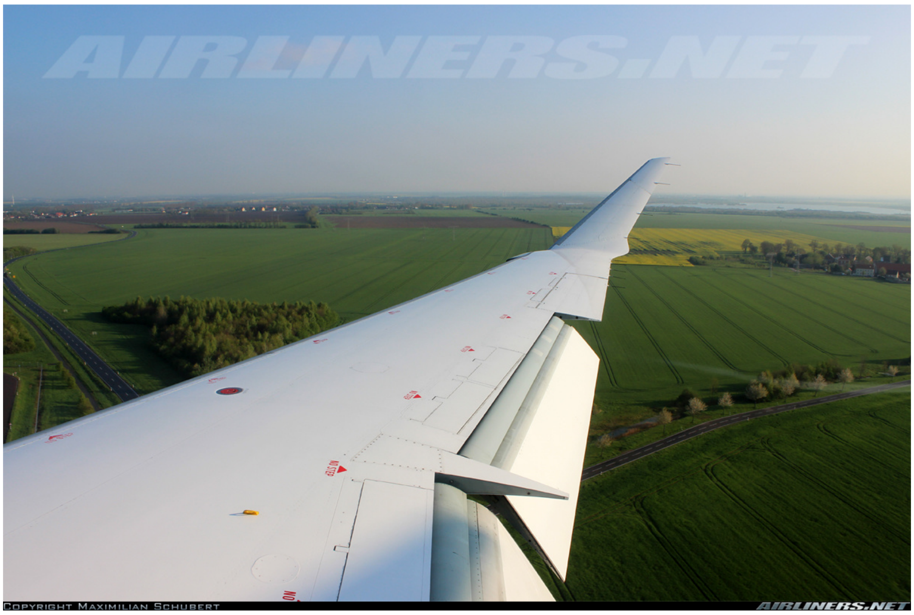
AIRLINERS.NET
COPYRIGHT MAXIMILIAN SCHUBERT
AIRLINERS.NET

Figure 3: Bombardier CRJ-900 NG (CL-600-2D24) approaching runway. [6]

This thesis focuses on the analysis of a wing with passive high-lift devices in the take-off configuration.

2 Objectives

The objective of this work is to perform an analysis of the flow around a wing equipped with passive high-lift devices in the take-off configuration.

First, a 2D CFD analysis to improve an airfoil configuration with high-lift leading and trailing edge devices for take-off is performed. CONVERGE CFD software is used for this purpose. [7]

In second place, a 3D CFD analysis of a wing with the airfoil equipped with the chosen high-lift devices is performed. FlightStream software is used for this purpose. [8]

3 Previous work

In my previous work, an analysis of the effect on the lift and drag produced by the use of passive high-lift trailing edge (flaps) on an airfoil was carried out. [9]

Passive high-lift trailing edge devices can be classified into devices that do not increase the chord when deflected and those that do. With the deflection of all high-lift trailing edge devices, the curvature is varied.

The study of an airfoil with different high-lift trailing edge devices was done using CFD (Computational Fluid Dynamics) numerical simulations with OpenFOAM (Open Field Operation and Manipulation).

Figure 4 shows the flaps that were analysed, three flaps that do not increase the chord on deflection (plain flap, split flap and slotted flap) and three flaps that increase the chord of the airfoil on deflection (Fowler flap, double slotted Fowler flap and triple slotted Fowler flap). A flap deflection angle δ of 20° was used with a length of 25% of the airfoil chord, this is a take-off configuration.

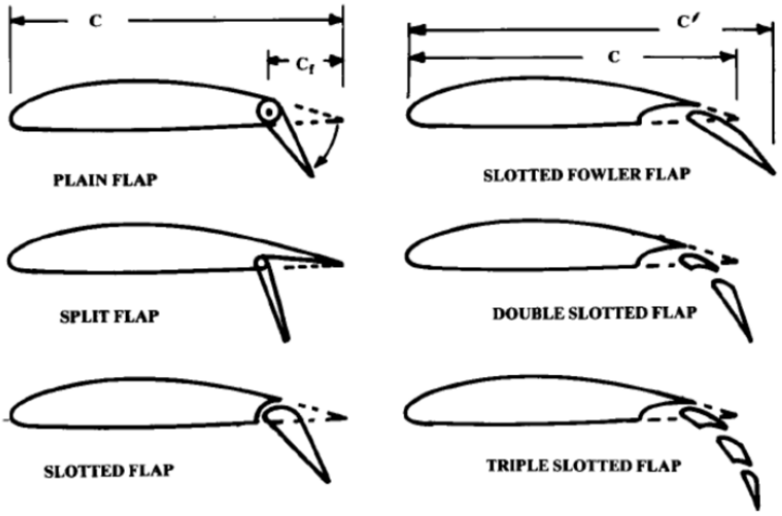

Figure 4: Study flaps. [4]

Flaps that do not extend like the plain, split or slotted flap, act by increasing the camber, which causes the zero lift angle to shift to the left on the lift graph and increases the maximum lift. The slope of the lift curve remains unchanged, and the stall angle is reduced somewhat. This is depicted in Figure 5.

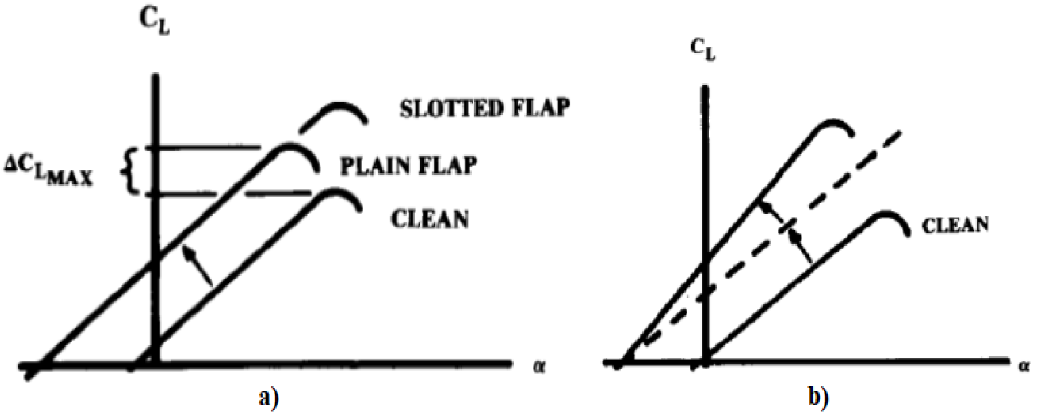

Figure 5: a) Contribution of flaps that do not extend. b) Contribution of flaps that extend. [4]

An extending flap such as the Fowler type acts similarly to the other flaps in terms of zero lift angle and stall angle. However, the chord of the airfoil increases as the flap deflects and more lift is generated for a given angle of attack compared to flaps that do not extend. As the reference chord is maintained, this increase occurs because the new C_l is equal to C_l multiplied by the new chord divided by the original chord. Figure 5b shows the increase in the slope of the lift curve with the use of the Fowler flap. The double slotted and triple slotted Fowler flaps act similarly to the Fowler flap but the maximum lift increases.

The study airfoil was the NACA 0012 airfoil, chosen because it is standardised, symmetrical and of reduced thickness. It is shown in Figure 6.

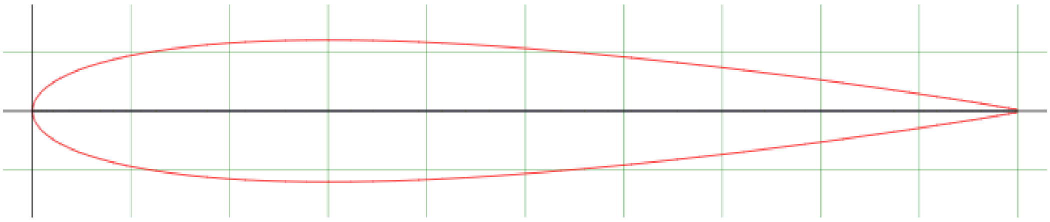

Figure 6: NACA 0012 airfoil. [10]

It was decided to use a RANS model since RANS turbulence models require less computational cost compared to LES, DES and DNS models. Within the RANS models, the $k-\varepsilon$ and $k-\omega$ SST models have been analysed as they are widely used (two-equation models).

After performing a convergence process with the two turbulent models, Figure 7, Figure 8 and Figure 9 show the values obtained for C_l, C_d and C_m varying the angle of attack. The results were compared with other simple software and experimental results. [11]

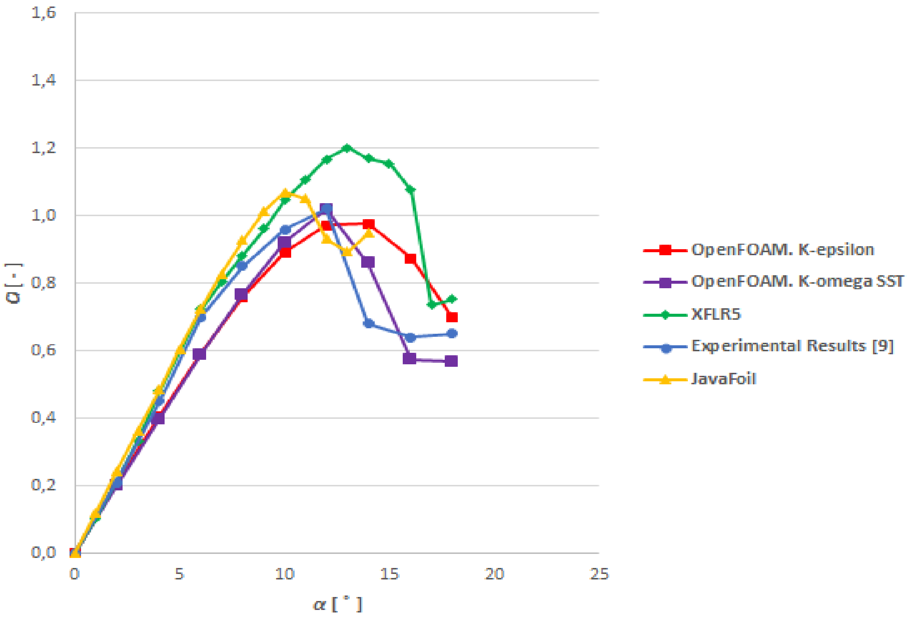

Figure 7: C_l comparison with turbulent models ($Re = 500000$). [9]

In Figure 7, C_l, it can be seen that the results for small angles of attack are similar and for larger angles of attack they differ. It can be seen that the results of the $k - \omega$ SST model are close to the experimental results.

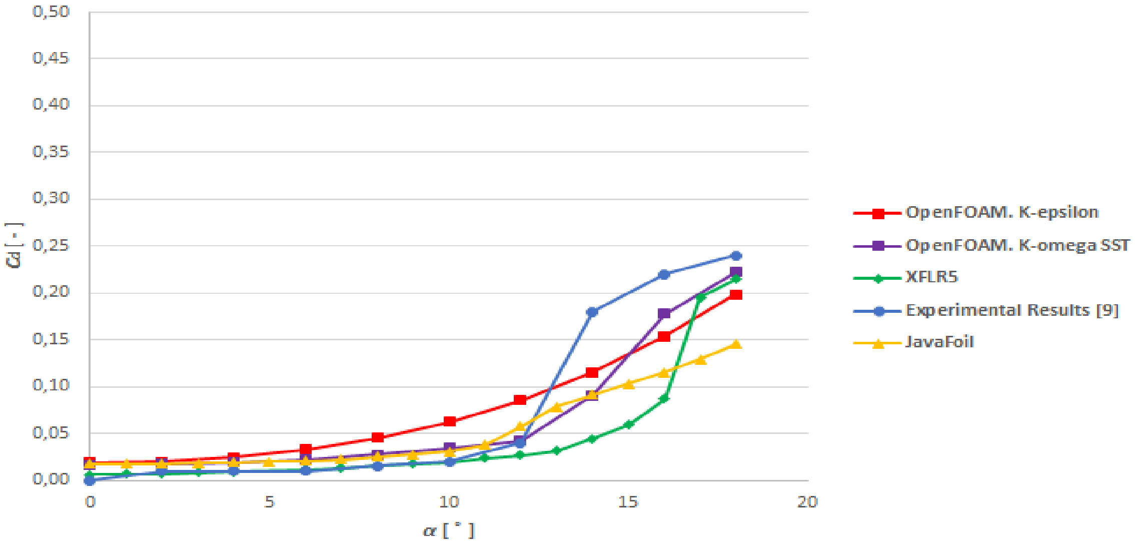

Figure 8: C_d comparison with turbulent models ($Re = 500000$). [9]

In Figure 8, it can be seen that the C_d values for the $k-\varepsilon$ model are much higher, while better results are obtained with $k-\omega$ SST. As for the C_m results, Figure 9, it can be seen that they are similar.

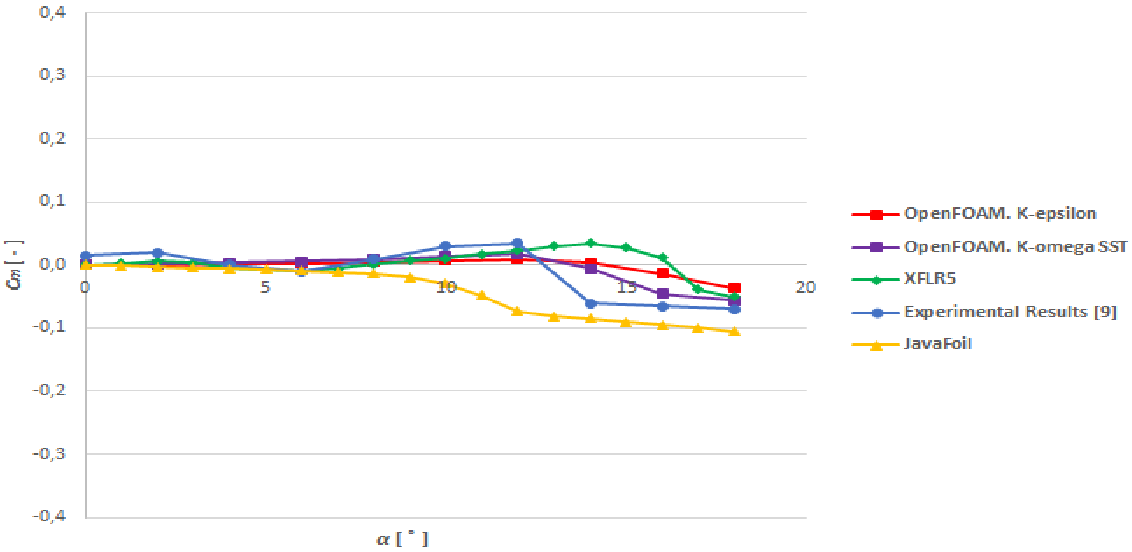

Figure 9: C_m comparison with turbulent models ($Re = 500000$). [9]

The results were more reliable and better fitted to the experimental data with the $k-\omega$ SST model. With the $k-\varepsilon$ model the stall input shape differed from the experimental case and was overestimating the C_d values. Thus, it was decided to use the $k-\omega$ SST model. ParaView software was used to represent the behaviour obtained, an example is shown in Figure 10.

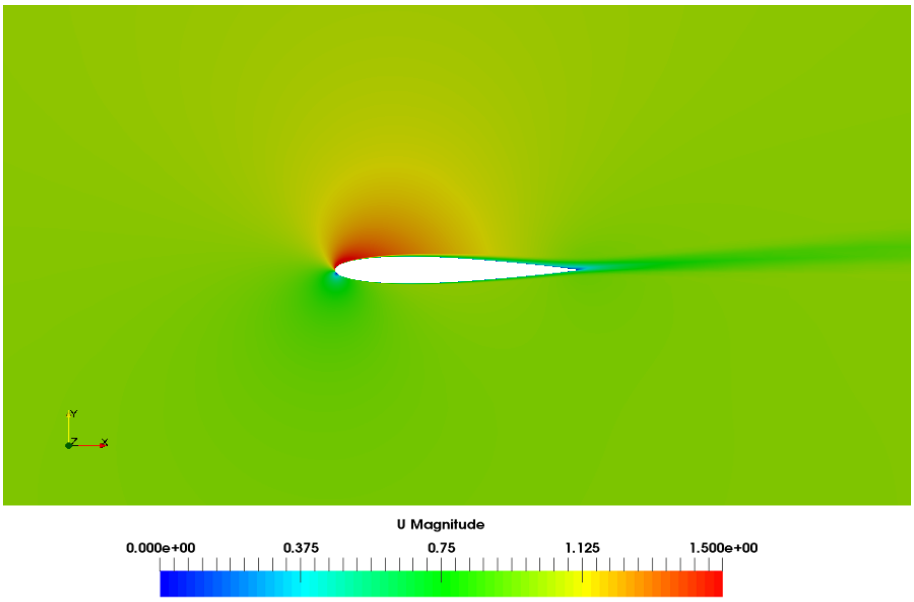

Figure 10: Velocity representation (m/s), NACA0012 airfoil ($\alpha = 6°$). [9]

Finally, the results of all the case studies, the main objective of the work, were compared. Figure 11 shows the C_l values with positive angles of attack of all the case studies.

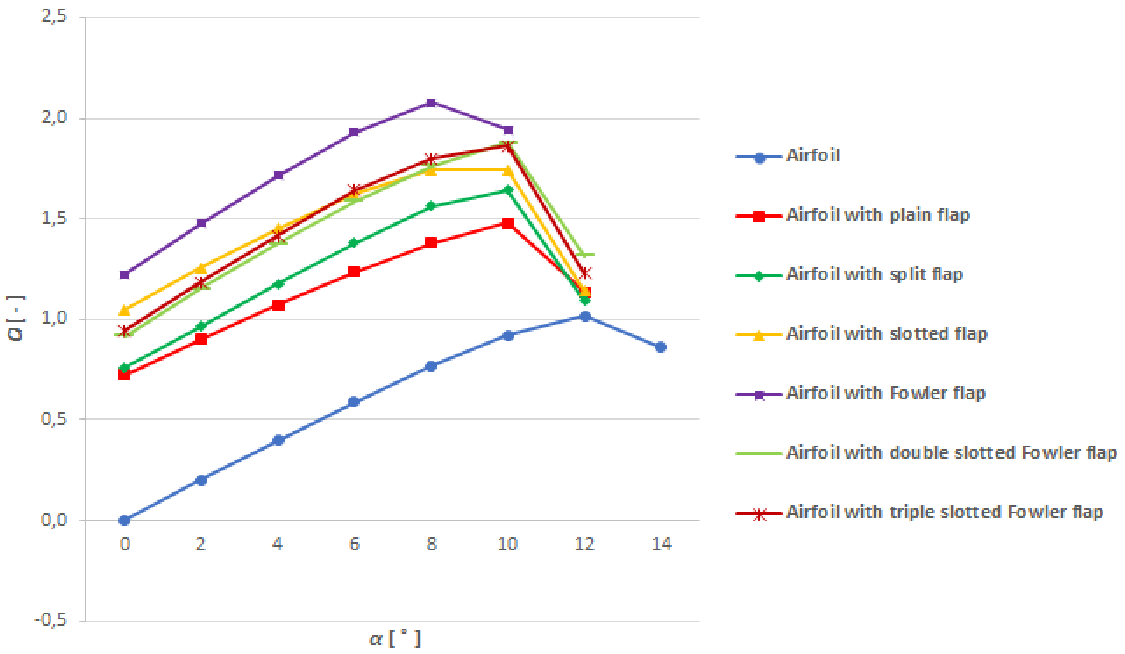

Figure 11: Comparative graph C_l - α of the NACA 0012 airfoil with all study flaps. [9]

It can be seen that with the use of all flaps the lift of the airfoil increases, and the stall angle decreases. It can be seen how the slope of the normal flap curve is maintained with that of the airfoil without flap and how the incorporation of the slot in the plain flap generates an increase in lift.

As for the group of flaps that increase the chord of the airfoil when deflected, it can be seen that they are the ones that generate a higher maximum lift coefficient and that their slopes increase. With the configurations designed for the double and triple slotted Fowler flap, no increase in lift is achieved compared to the simple Fowler for this configuration (take-off). Nevertheless, for the landing configuration, these flaps can be more useful by generating higher C_l with higher deflection. The design of these types of flaps has a great complexity since many parameters influence, such as the angles and positions that the different sections of the flap have. A detailed study of these parameters was not carried out as the work was too extensive. Despite this, it was achieved that they stall for a higher angle of attack compared to the simple Fowler. In addition, they generate higher lift compared to flaps that do not extend.

In Figure 12, C_l is represented with C_d of all the case studies. It can be seen how all flaps generate an increase in the lift without increasing drag too much, being the Fowler type flaps the ones that generate the highest lift.

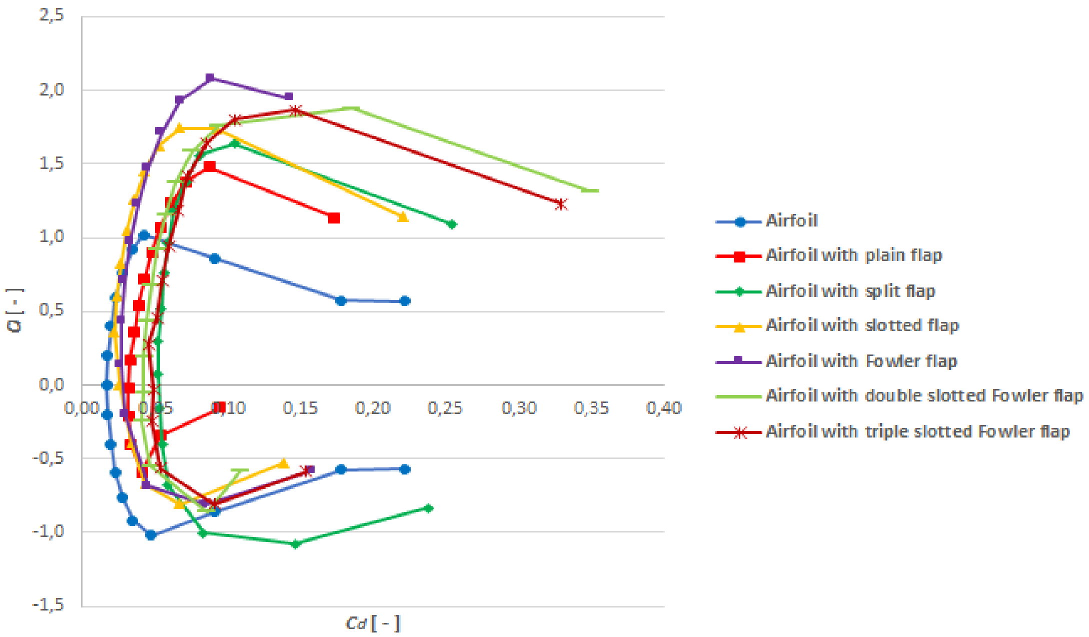

Figure 12: Comparative graph C_l - C_d of the NACA 0012 airfoil with all study flaps. [9]

As already mentioned, for each point of each polar, the slope of the straight line passing through that point and the origin is the aerodynamic efficiency of the airfoil. It is seen that the simple Fowler flap is the best according to the graph obtained in that sense.

4 Method

This chapter shows the method used to obtain the results of the work. The chapter is divided into 2D analysis and 3D analysis and all the characteristics of the methods are shown.

4.1 2-D analysis

4.1.1 Numerical simulation

The 2D CFD analysis is performed using CONVERGE CFD software. This software is a Convergent Science software that features truly autonomous meshing, state-of-the-art physical models, a robust chemistry solver, and the ability to easily accommodate complex moving geometries, so you can take on the hard CFD problems. [7]

Annex A shows how to use the CONVERGE CFD software to obtain the results of the work.

CONVERGE offers several iterative algorithms for the solution of mass, momentum, energy, species, and scalar transport. CONVERGE offers pressure-velocity coupling using a modified Pressure Implicit with Splitting of Operator (PISO) method of Issa (1986). The PISO algorithm as implemented in CONVERGE starts with a predictor step where the momentum equation is solved. After the predictor, a pressure equation is derived and solved, which leads to a correction, which is applied to the momentum equation. This process of correcting the momentum equation and re-solving can be repeated as many times as necessary to achieve the desired accuracy. After the momentum predictor and first corrector step have been completed, the other transport equations are solved in series. [12]

Furthermore, CONVERGE offers pressure-velocity coupling using a modified Semi-Implicit Method for Pressure-Linked Equations (SIMPLE) method of Patankar (1980). The modified SIMPLE algorithm differs from the PISO algorithm described above in that the momentum equation is solved within the iterative algorithm, rather than as a predictor step. At each iteration, SIMPLE solves the momentum equation, then a derived pressure equation. As with PISO, after the pressure solution is used to update the velocity, the other transport equations are solved in series. The solution is more "expensive" with SIMPLE and in this work it has been decided to use the PISO solver since correct results are obtained.

4.1.2 RANS model used

In Reynolds-Averaged Navier-Stokes (RANS) turbulence models, the flow variables (e.g., velocity) are decomposed into an ensemble mean and a fluctuating term. [12]

Thus, the velocity and pressure components are replaced by:

$$\begin{gathered} u_i = \overline{u_i} + u_i' \\ p = \overline{p} + p' \end{gathered} \tag{1}$$

Substituting the decompositions of Equation 1 into the Navier-Stokes equation for incompressible flow and averaging, yields the RANS equations:

$$\begin{gathered} \frac{\partial \overline{u_i}}{\partial x_i} = 0 \\ \frac{\partial \overline{u_i}}{\partial t} + \overline{u_j}\frac{\partial \overline{u_i}}{\partial x_j} = -\frac{1}{\rho}\frac{\partial \overline{p}}{\partial x_i} + \frac{1}{\rho}\frac{\partial}{\partial x_j}(\overline{\tau_{ij}'} - \rho\overline{u_i'u_j'}) \end{gathered} \tag{2}$$

with:

$$\overline{\tau_{ij}'} = 2\mu\overline{S_{ij}} = \mu\left(\frac{\partial \overline{u_i}}{\partial x_j} + \frac{\partial \overline{u_j}}{\partial x_i}\right) \tag{3}$$

$$-\rho\overline{u_i'u_j'} = \overline{\tau_{ij}'}_t = 2\mu_t\overline{S_{ij}} \tag{4}$$

The following RANS turbulence models are available in CONVERGE: Standard $k-\varepsilon$, RNG (Renormalization Group) $k-\varepsilon$, Rapid Distortion RNG $k-\varepsilon$ (Han and Reitz, 1995), Realizable $k-\varepsilon$, Standard $k-\omega$ 1998 (Wilcox, 1998), Standard $k-\omega$ 2006 (Wilcox, 2006), $k-\omega$ SST and Spalart-Allmaras (1994). [12]

Following my previous work, it was concluded that the results from the $k-\omega$ SST are closer to the experimental results than those of $k-\varepsilon$. In this work, the $k-\omega$ SST model is used.

The RANS $k-\omega$ shear stress transport (SST) model combines the advantages of a standard $k-\omega$ model and a standard $k-\varepsilon$ model. In general, the $k-\omega$ SST model performs well when simulating external flows. [12]

The $k-\omega$ SST model in CONVERGE expresses the turbulent viscosity as:

$$\mu_t = \frac{\rho a_1 k}{max[a_1\omega, SF_2]'} \tag{5}$$

where:

$$S = \sqrt{2S_{ij}S_{ij}} \tag{6}$$

The transport equation for k and for ω are shown in Equation 7 and Equation 8:

$$\frac{\partial \rho k}{\partial t} + \frac{\partial \rho u_j k}{\partial x_j} = P - \beta^* \rho \omega k + \frac{\partial}{\partial x_j}\left[(\mu + \sigma_k \mu_t)\frac{\partial k}{\partial x_j}\right] \tag{7}$$

$$\frac{\partial \rho \omega}{\partial t} + \frac{\partial \rho u_j \omega}{\partial x_j} = \frac{\alpha}{\nu_t}P - \beta \rho \omega^2 + \frac{\partial}{\partial x_j}\left[(\mu + \sigma_\omega \mu_t)\frac{\partial \omega}{\partial x_j}\right] + 2(1-F_1)\frac{\rho \sigma_{\omega 2}}{\omega}\frac{\partial k}{\partial x_j}\frac{\partial \omega}{\partial x_j} \tag{8}$$

The expression for the mean strain rate tensor S_{ij} is as shown in Equation 9 and the expression for the production term P is Equation 10.

$$S_{ij} = \frac{1}{2}\left(\frac{\partial \tilde{u}_i}{\partial x_j} + \frac{\partial \tilde{u}_j}{\partial x_i}\right) \tag{9}$$

$$P = \min\left[\tau_{ij}\frac{\partial u_i}{\partial x_j}, 10\beta^* \rho \omega k\right] \tag{10}$$

Each constant in the transport equations for k and ω (such as σ_k) is a blend of inner and outer constants. For some constant ϕ, Equation 11 below defines the blending function:

$$\phi = F_1\phi_1 + (1-F_1)\phi_2 \tag{11}$$

CONVERGE calculates F_1 and F_2 using the expressions below:

$$F_1 = \tanh\left(\min\left[\max\left[\frac{\sqrt{k}}{\beta^*\omega d}, \frac{500\nu}{d^2\omega}\right], \frac{4\rho\sigma_{\omega 2}k}{CD_{k\omega}d^2}\right]^4\right) \tag{12}$$

$$F_2 = \tanh\left(\max\left[2\frac{\sqrt{k}}{\beta^*\omega d}, \frac{500\nu}{d^2\omega}\right]^2\right), \tag{13}$$

where:

$$CD_{k\omega} = \max\left[2\rho\sigma_{\omega 2}\frac{1}{\omega}\frac{\partial k}{\partial x_j}\frac{\partial \omega}{\partial x_j}, 10^{-10}\right] \tag{14}$$

Finally, Equation 15 and Equation 16 below defines the inner and outer model constants and parameters used in the $k - \omega$ SST model:

$$\alpha_1 = \frac{5}{9} \quad \alpha_2 = 0.44 \quad \sigma_{k1} = 0.85 \quad \sigma_{\omega 1} = 0.500 \quad \beta_1 = 0.075 \tag{15}$$

$$\sigma_{k2} = 1.00 \quad \sigma_{\omega 2} = 0.856 \quad \beta_2 = 0.0828 \quad \beta^* = 0.09 \quad \kappa = 0.41 \quad \alpha_1 = 0.31 \tag{16}$$

4.1.3 Characteristics of the airfoil and passive high-lift devices

Airfoil

The airfoil under study is the NACA 0012 airfoil, chosen because it is standardized, symmetrical and of reduced thickness. The airfoil is represented in Figure 6. In the 4-digit NACA airfoils: [13]

- The first digit describes the maximum camber as a percentage of the chord.
- The second digit describes the position of the maximum camber in tenths of the chord.
- The last two digits describe the maximum thickness as a percentage of the chord.

High-lift devices

The high-lift trailing edge device analysed is the plain flap. The effect of the plain flap with different lengths and deflection angles is compared. Table 1 shows the plain flap configurations analysed.

Length (%c)	Deflection angle (°)
20	20
30	15
40	10

Table 1: Plain flap configurations.

NACA 0012 airfoil with the different study plain flaps is shown below. Figure 13 shows the NACA 0012 airfoil with a plain flap with a length of 20%c and with a deflection angle of 20° drawn in CatiaV5. The coordinate system is located at 1/4 chord.

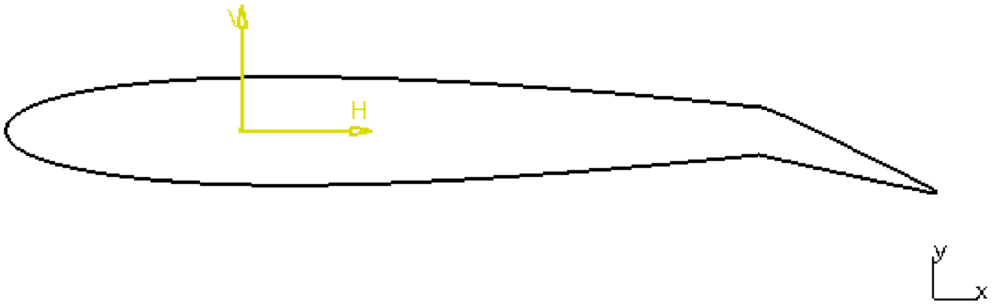

Figure 13: NACA 0012 airfoil with a plain flap (20%c 20°).

Figure 14 shows the NACA 0012 airfoil with a plain flap with a length of 30%c and with a deflection angle of 15° drawn in CatiaV5.

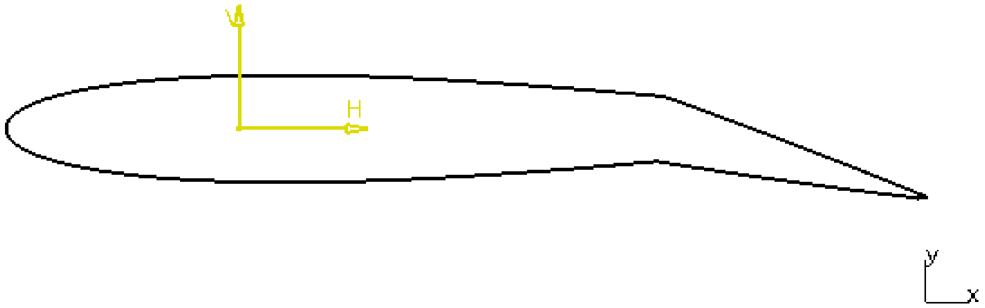

Figure 14: NACA 0012 airfoil with a plain flap (30%c 15°).

Finally, Figure 15 shows the NACA 0012 airfoil with a plain flap with a length of 40%c and with a deflection angle of 10° drawn in CatiaV5.

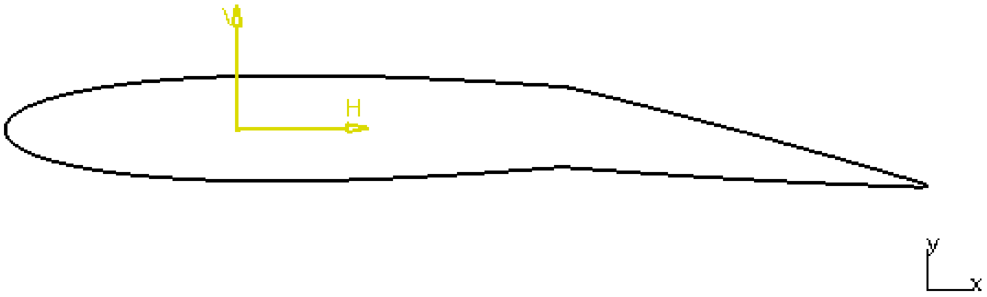

Figure 15: NACA 0012 airfoil with a plain flap (40%c 10°).

Once the plain flap configuration is chosen, different leading edge flaps are compared with the plain flap equipped, Table 2. The coordinates of all case studies are shown in Annex B.

Length (%c)	Deflection angle (°)
15	20
20	15
25	10

Table 2: Leading edge flap configurations.

NACA 0012 airfoil with the different study leading edge flaps is shown below. Figure 16 shows the NACA 0012 airfoil with a leading edge flap with a length of 15%c and with a deflection angle of 20° and a plain flap with a length of 20%c and with a deflection angle of 20° drawn in CatiaV5.

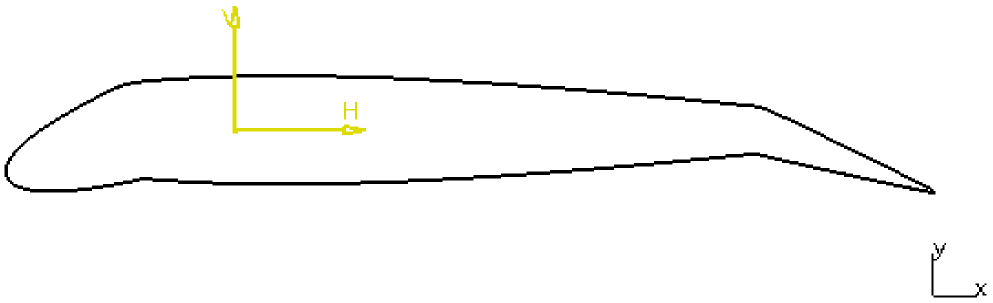

Figure 16: NACA 0012 airfoil with a leading edge flap (15%c 20°) and a plain flap (20%c 20°).

Figure 17 shows the NACA 0012 airfoil with a leading edge flap with a length of 20%c and with a deflection angle of 15° and a plain flap with a length of 20%c and with a deflection angle of 20° drawn in CatiaV5.

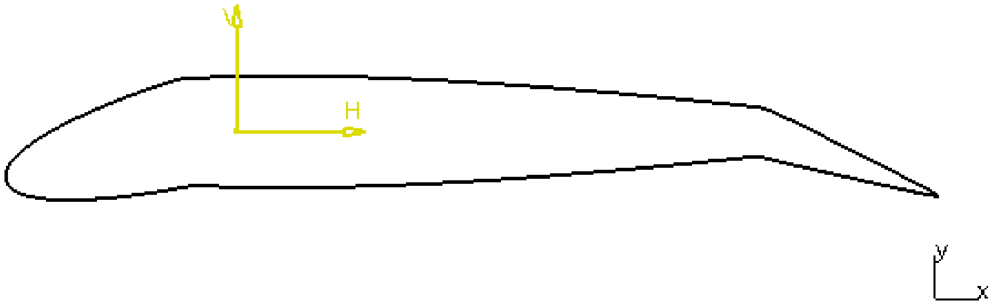

Figure 17: NACA 0012 airfoil with a leading edge flap (20%c 15°) and a plain flap (20%c 20°).

Finally, Figure 18 shows the NACA 0012 airfoil with a leading edge flap with a length of 25%c and with a deflection angle of 10° and a plain flap with a length of 20%c and with a deflection angle of 20° drawn in CatiaV5.

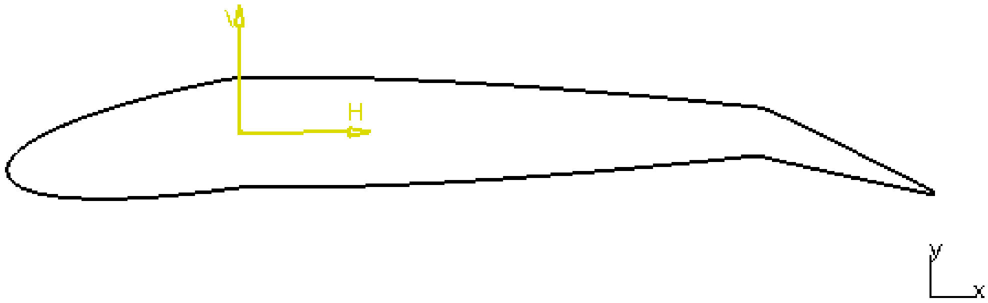

Figure 18: NACA 0012 airfoil with a leading edge flap (25%c 10°) and a plain flap (20%c 20°).

Some values of variables characteristic of the problem are shown in Table 3. The value of the Reynolds number has been chosen to compare the results with studies that have that value.

Variable	Value
U	$40\ \frac{\mathrm{m}}{\mathrm{s}}$
ρ	$1.225\ \frac{\mathrm{kg}}{\mathrm{m}^3}$
μ	$1.7894 \cdot 10^{-5}\ \frac{\mathrm{kg}}{\mathrm{m\,s}}$
L	2.1911 m
Re	6000000

Table 3: Some values of characteristic variables of the problem.

4.1.4 Description of the mesh

It has been decided to use a C-mesh with a quadtree grid. It has been decided to use the mesh of the CONVERGE example called *NACA 0012 airfoil 10 deg AOA inlaid transient RANS* to start realizing the mesh.

4.1.4.1 Initial conditions

Region 0 is created to define the initial conditions of the case. The initial conditions values are shown in Table 4.

Variable	Value
U	[40, 0, 0]
T	288.15 K
P	101325 Pa
Viscosity ratio	1
Lenght scale	0.0003 m

Table 4: Values that are imposed in *Region 0* created.

A velocity of 40 m/s has been chosen as it is a suitable velocity for the take-off of an aircraft such as the Cessna 172 aircraft. The maximum velocity with deflected flaps is 86 knots (44.242 m/s) for the Cessna 172 aircraft. [14]

The flow velocity in the x-direction is imposed and to change the angle of attack the airfoil is rotated.

Air species such as O_2 and N_2 with their corresponding mass fractions (O2=0.233 and N2=0.767) are created.

4.1.4.2 Boundary conditions

In a CFD analysis it is very important to keep in mind the boundary conditions. The problem consists of five distinct zones:

- Airfoil: *wall* type boundary condition is imposed on it. The region created *Region 0* is selected.
- Front: *two D* type boundary condition is imposed on it. This condition is imposed on the lateral faces to impose that the work is done in 2D. The region created *Region 0* is selected.
- Back: *two D* type boundary condition is imposed on it too.
- Inflow: the $inflow$ boundary condition is imposed on it. The region created *Region 0* is selected.
- Outflow: the $outflow$ boundary condition is imposed on it. The region created *Region 0* is selected.

Figure 19 shows the five problem zones.

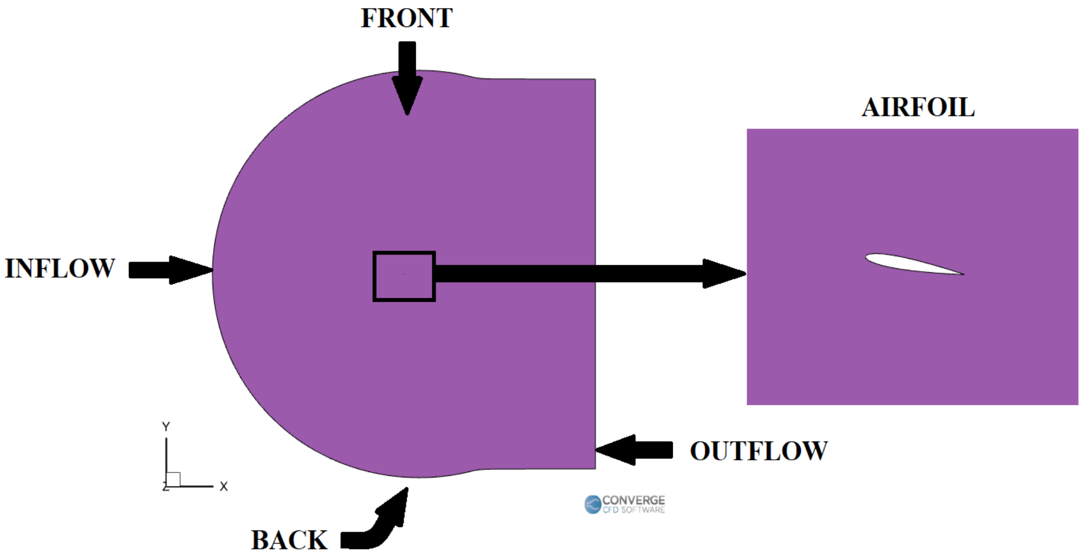

Figure 19: Five problem zones.

The boundary conditions can be Dirichlet or Neumann type. The Dirichlet type boundary condition specifies the value, it is given by: [12]

$$\phi = f \tag{17}$$

While the Neumann type boundary condition specifies the value of the first derivative: [12]

$$\frac{\partial \phi}{\partial x} = f \tag{18}$$

Table 5, Table 6 and Table 7 show the types of boundary conditions for the variables on the airfoil, inflow and outflow boundaries respectively.

Variable	Condition type	Value
Velocity	Law of wall	[0, 0, 0]
Pressure	Neumann	-
Temperature	Neumann	0
Species	Neumann	-
Passive	Neumann	-
Turbulence (k)	Neumann	0
Turbulence (ω)	Law of wall	-

Table 5: Boundary conditions for the airfoil in CONVERGE CFD.

Variable	Condition type	Value
Velocity	Dirichlet	[40, 0, 0]
Pressure	Neumann	0
Temperature	Dirichlet	288.15
Species	Dirichlet	Air=1
Passive	Dirichlet	-
Turbulence (k)	Intensity	0.01
Turbulence (ω)	Length scale	0.0003

Table 6: Boundary conditions for the inflow in CONVERGE CFD.

Variable	Condition type	Value
Velocity	Neumann	[0, 0, 0]
Pressure	Dirichlet	101325
Temperature	Neumann	0
Species	Neumann	-
Passive	Neumann	-
Turbulence (k)	Neumann	0
Turbulence (ω)	Neumann	0

Table 7: Boundary conditions for the outflow in CONVERGE CFD.

4.1.4.3 Grid control

Several important parameters are defined in the grid to be used. First, a value for the Base grid is chosen. The base grid size is the largest grid size available in the simulation. [15]

Moreover, fixed embedding is used to refine the portion of the grid near the airfoil. The base mesh and the embedding near the airfoil are decided based on the y^+ value. Y^+ is the non-dimensionalised wall distance that tells where the first cell is in the boundary layer. Y^+ can be defined in the following way:

$$y^+ = \frac{u_* y}{\nu} \tag{19}$$

where u is the friction velocity and y is the distance on the y-axis of the first cell. [16]

The boundary layer consists of different layers and the y^+ can distinguish them for the study. Figure 20 represents these layers.

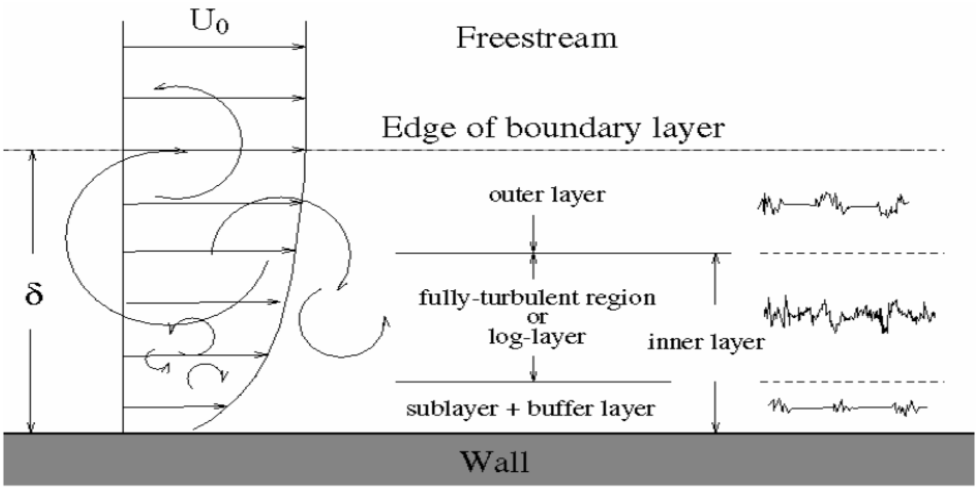
U_0
Freestream
Edge of boundary layer
outer layer
δ
fully-turbulent region
or
log-layer
inner layer
sublayer + buffer layer
Wall

Figure 20: Boundary layer. [17]

First, the outer layer is the layer furthest from the wall and any model usually calculates this area. The inner layer is the layer next to the wall. This layer consists of three sublayers: the logarithmic layer, the buffer layer and the viscous sublayer. In the logarithmic layer both viscous and turbulent stresses are relevant.

Depending on the turbulence model used, it will be necessary to calculate the boundary layer more or less accurately by using a larger or smaller value of the distance from the first cell to the wall in units of y^+. In the $k-\omega$ SST model, it is recommended to use y^+ values between 30 and 300 (logarithmic layer) when using wall functions, or values of $y^+ < 5$ to solve the viscous sublayer.

The Pointwise calculator is used to compute the height of the first mesh cell (Δs) of the wall required to achieve the desired y^+. [18]

With the Δs value, the embedding scale near to the airfoil is obtained. The embedding cell sizes are governed by: [15]

$$\Delta s = \frac{dx_{Base\ grid}}{2^{Embedding\ scale}} \tag{20}$$

Also, an adaptive mesh refinement (AMR) is used for velocity. AMR is an automatic mesh refinement based on local flow conditions.

4.1.4.4 Convergence process

A convergence process has been carried out to decide the characteristics of the mesh. The dimensions of the example domain in the CONVERGE CFD software have been used and the angle of attack of the airfoil in the study is 10°.

CONVERGE always ensures that at each time step the solution is converged to the prescribed tolerances by increasing the number of iterations and/or reducing further the time step. The residual is one of the most fundamental measures of an iterative solution's convergence, as it directly quantifies the error in the solution of the system of equations. The residuals for each of the equations during the simulation process can be seen in the file *converge.log*.

Table 8 shows the values of the tolerances used taking into account computational limitations and Marius-Gabriel Cojocaru's recommendations.

Equation	Convergence tolerance
Momentum	10^{-5}
Pressure	10^{-8}
Density	10^{-4}
Energy	10^{-4}
Species	10^{-4}
Passive	10^{-5}
Turbulent Kinetic Energy	20^{-3}
Specific dissipation rate	20^{-3}
Velocity variance scale	10^{-3}
Elliptic relaxation function	10^{-3}
Velocity Scale Ratio	10^{-3}
Radiation	10^{-8}
Wall dist	10^{-3}

Table 8: Convergence tolerances for the equations.

To obtain the forces and moments on the airfoil, the values obtained between second 1 and second 1.5 are averaged. An example of the pressure forces obtained is shown in Figure 21 and Figure 22.

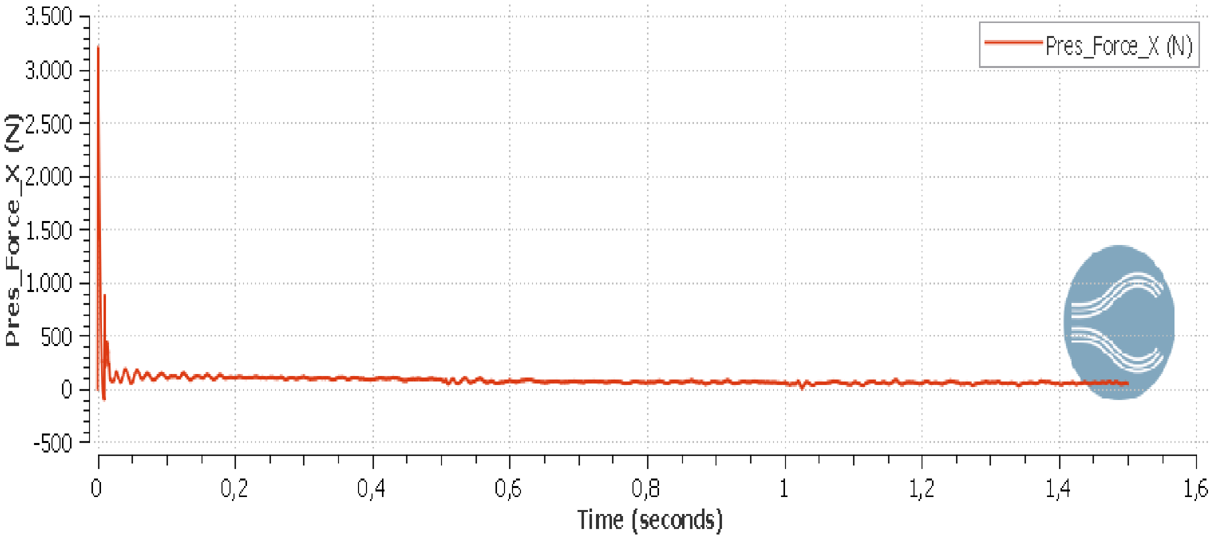

Figure 21: Pressure Forces X (NACA 0012. Base Grid=9m, Embed Scale=13).

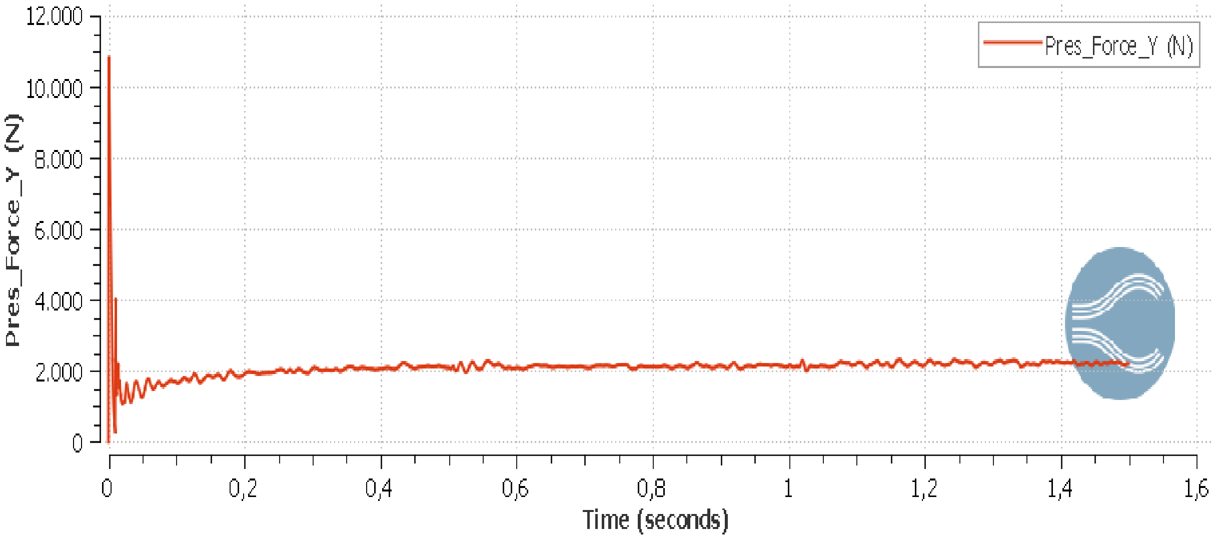

Figure 22: Pressure Forces Y (NACA 0012. Base Grid=9m, Embed Scale=13).

After adding the average values of pressure and viscous forces to obtain lift and drag and doing the same for momentum, the following equations are used to obtain the coefficients:

$$C_l = \frac{2L}{\rho c U^2} \tag{21}$$

$$C_d = \frac{2D}{\rho c U^2} \tag{22}$$

$$C_m = \frac{2M}{\rho c^2 U^2} \tag{23}$$

First, three meshes with three grid base values (10m, 9m and 8m) were compared. An embed scale of 12 has been used. The values of y^+, computation time and the lift coefficient C_l, drag coefficient C_d and moment coefficient C_m are shown in Table 9.

Base Grid (m)	y^+ average	Δs (m)	Time (h)	C_l	C_d	C_m
10	147.21	0.00144	4.816	0.997 (1.276 %)	0.039 (8.728 %)	-0.011 (16.268 %)
9	132.22	0.00129	5.200	0.999 (1.107 %)	0.037 (3.789 %)	-0.010 (11.779 %)
8	115.86	0.00113	6.366	1.010	0.036	-0.009

Table 9: Convergence process of the base grid ($\alpha = 10°$, Embed Scale = 12).

It is important to take into account computational limitations. A personal computer is used with an Intel(R) Core(TM) i7-6500U CPU 2.50GHz, 2592 MHz with two main cores.

The results obtained from the coefficients have been compared with those obtained with the 8m base grid and the error percentages have been calculated. After analyzing these errors and the computation time, it was decided to choose a value of 9m for the base grid.

Next, a comparison of three grids with three values of embed scale (12, 13 and 14) has been made. The base grid used is the 9m grid. Table 10 shows the results obtained.

Embed Scale	y^+ average	Δs (m)	Time (h)	C_l	C_d	C_m
12	132.22	0.00129	5.20	0.999 (3.617 %)	0.037 (7.184 %)	-0.010 (7.473 %)
13	60.41	0.00059	6.48	1.027 (0.895 %)	0.036 (3.034 %)	-0.004 (3.290 %)
14	31.15	0.00030	10.21	1.036	0.035	0.002

Table 10: Convergence process of the embed scale ($\alpha = 10°$, Base grid = 9m).

After analyzing the results, it was decided to use an embed scale of 13. Thus, the mesh used has the following characteristics:

y^+ average	60.41
Δs (m)	0.000589
Base Grid (m)	9
Embed Scale	13
Embed layers	2

Table 11: Characteristics of the mesh used.

As for the number of embed layers, 2 is a good choice. Besides, another box-type fixed embedding with scale 9 is used around the airfoil. The AMR has a maximum embedding level of 10 and a subgrid criterion of 0.15 m/s. [15]

Figure 23 shows the mesh used in this work. It can be observed the box-type fixed embedding used around the airfoil and how the mesh cells are of smaller dimensions in the vicinity of the airfoil and in the area where the trail appears.

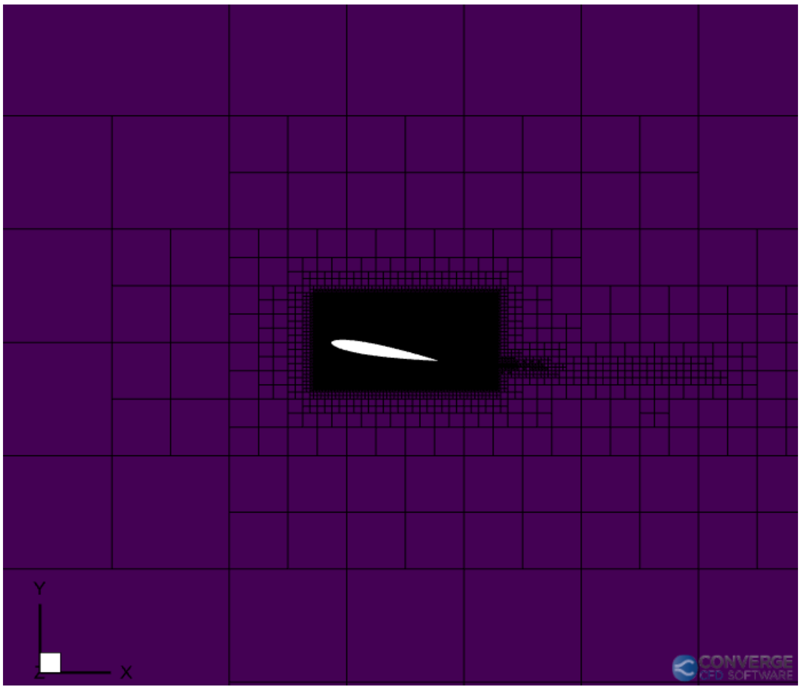

Figure 23: Mesh used.

4.1.4.5 Validation of results

An important part of the work is the validation of the results. To confirm that a correct mesh is used and that the parameters used in the case are correct, a validation of the results is performed by comparing them with experimental results. In addition, the results are compared with another software called XFLR5. XFLR5 is an analysis tool for airfoils, wings and planes operating at low Reynolds Numbers. [19]

XFLR5 cannot be used for complex airfoil geometries, has some shortcomings and uses the panel method, with results for large deflection angles being unreliable. However, it allows for time-saving calculations and information on aerodynamic behaviour.

Again, it is reminded that there are computational limitations but it can be seen below that the results can be considered correct for this university work.

Figure 24 shows the C_l values obtained with the mesh used along with results obtained with XFLR5 and with experimental results. [3]

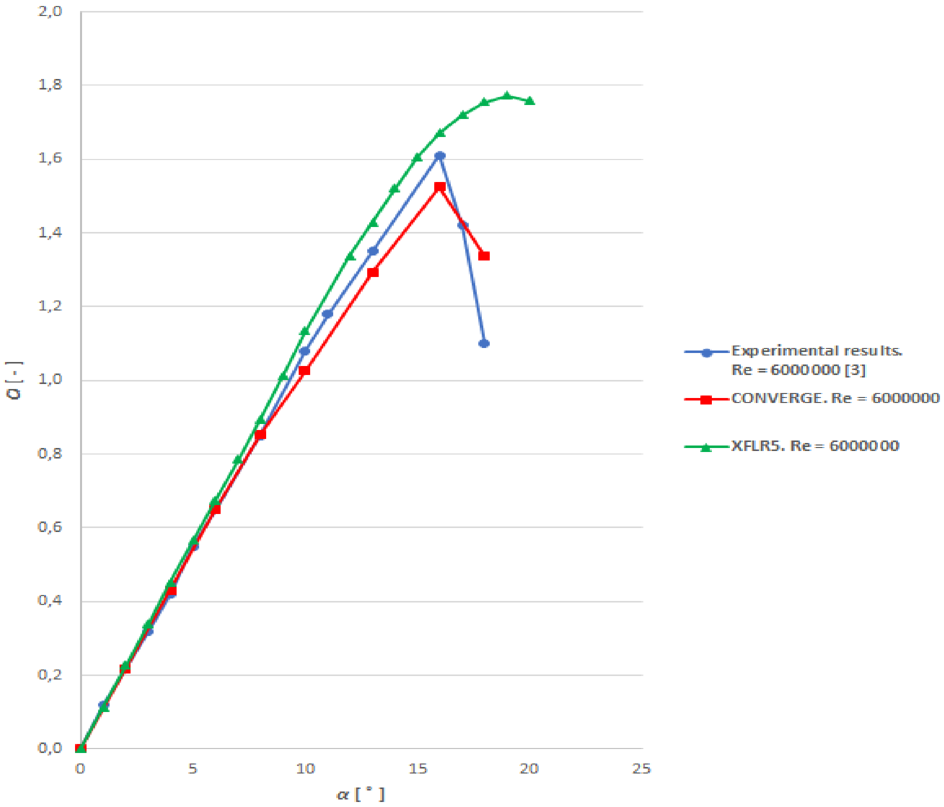

Figure 24: Comparison of C_l values.

Figure 24 shows that the obtained C_l values can be considered correct. With the CONVERGE CFD software, the airfoil stalls with the same angle of attack as in the experimental results, which are the reference results. There is some difference in values with high angles of attack, however, with the computational limitations that we have, these results are considered valid. Moreover, it can be seen that the CONVERGE results are more realistic than the results obtained with the XFLR5 software.

Figure 25 shows the comparison of C_d values. The C_d values differ somewhat at large angles of attack but the results obtained are considered valid.

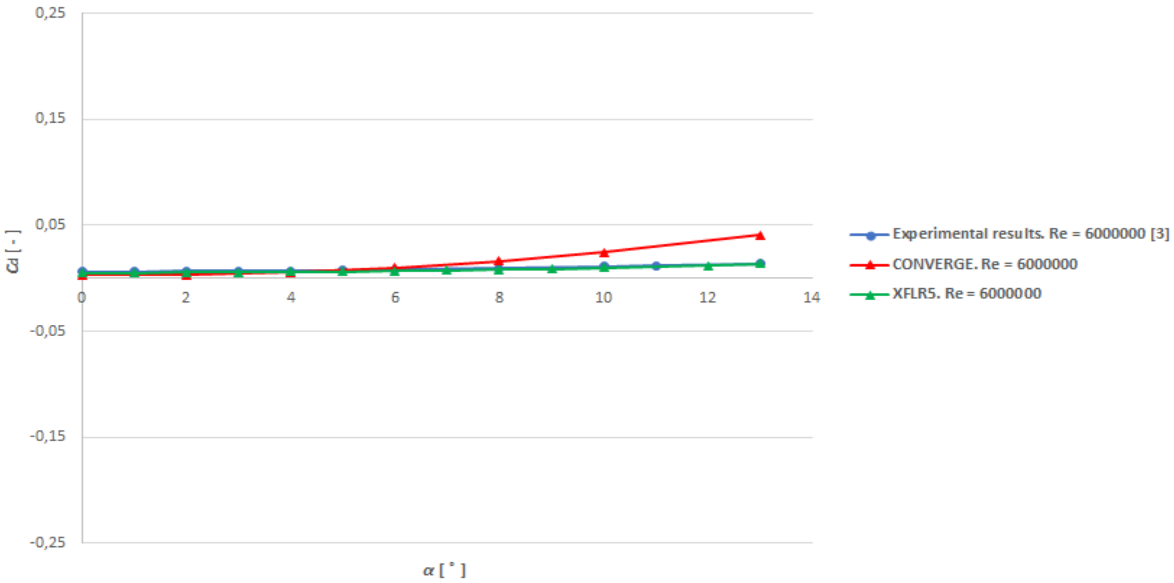

Figure 25: Comparison of C_d values.

Figure 26 shows the comparison of C_m values. It can be seen that the results obtained for C_m are similar to the experimental results.

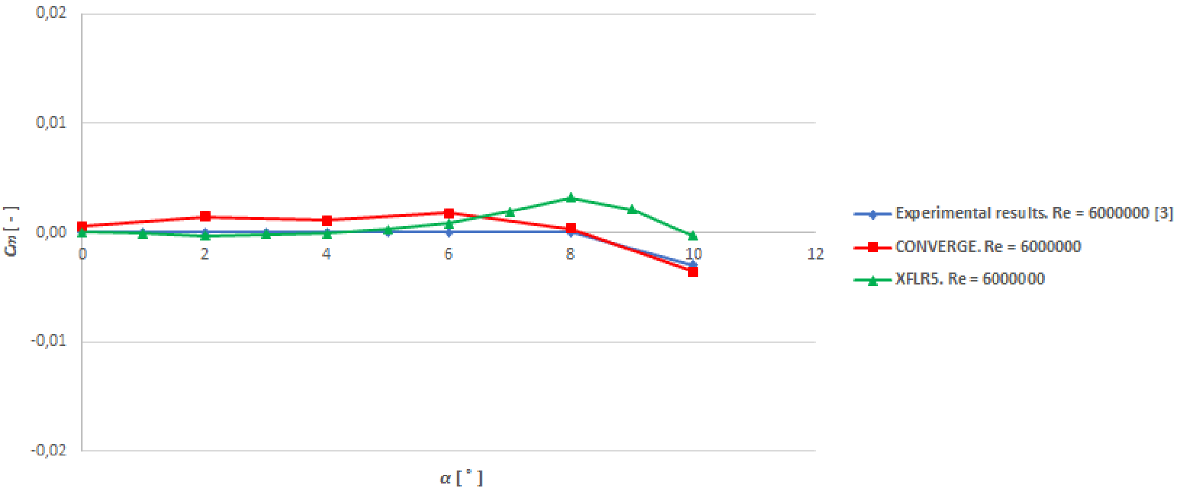

Figure 26: Comparison of C_m values.

It is concluded that the configuration and the mesh used to perform the simulations are valid.

Tecplot for CONVERGE software is used to visualize the simulations. Tecplot for CONVERGE is included with the CONVERGE license. Figure 27 shows representations of different variables of the airfoil simulation for an angle of attack of 10°.

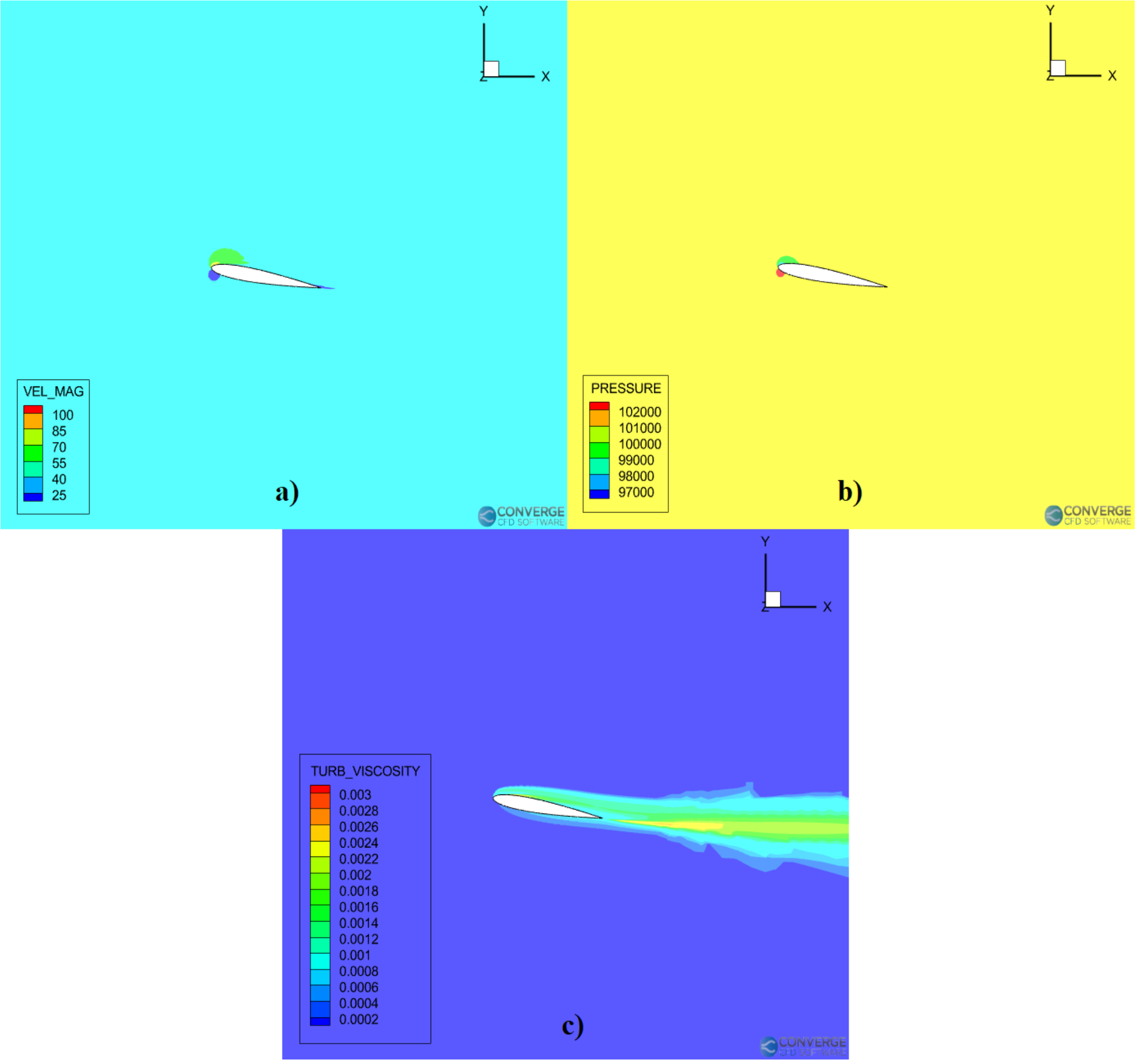

Figure 27: NACA0012 airfoil ($\alpha = 10°$). a) Velocity representation (m/s). b) Pressure representation (Pa). c) Turbulent viscosity representation (m^2/s).

Figure 27a represents the velocity. For an angle of attack of 10°, the increase in velocity can be seen on the upper surface of the airfoil at the leading edge. Also, you can see a zone of reduced velocity at the trailing edge and on the lower surface at the leading edge. Nevertheless, in Figure 27b you can see that the pressure is higher on the lower surface at the leading edge than on the upper surface.

On the other hand, Figure 27c shows the turbulent viscosity and it can be seen that it is higher at the trailing edge of the airfoil.

4.2 3-D analysis

4.2.1 Numerical simulation

It is important to perform a 3D analysis with the aircraft wing because it is closer to reality. FlightStream has been used for this analysis.

FlightStream is a DAR Corporation software and it is a high fidelity aerodynamics tool perfectly suited for aircraft designers. The unique vorticity based flow solver, which uses only a surface mesh, produces accurate solutions in a fraction of the time required by full volume mesh CFD solvers. The solver is capable of modelling and analyzing aircraft, propellers, high-lift devices and jet engine effects. [8]

High-Lift devices such as flaps, slats, spoilers, etc can be modelled in FlightStream to analyze how the flow over the wing interacts with these complex geometries. Annex A shows how to use the FlightStream software to obtain the results of the work.

4.2.2 Wing characteristics

The study wing has the NACA 0012 airfoil equipped with the leading flap with a length of 15%c and with a deflection angle of 20° and with the plain flap with a length of 20%c and with a deflection angle of 20°. It has been decided that the wing should have an 11m span, which is the span of the Cessna 172 aircraft wing. The wing is shown in Figure 28.

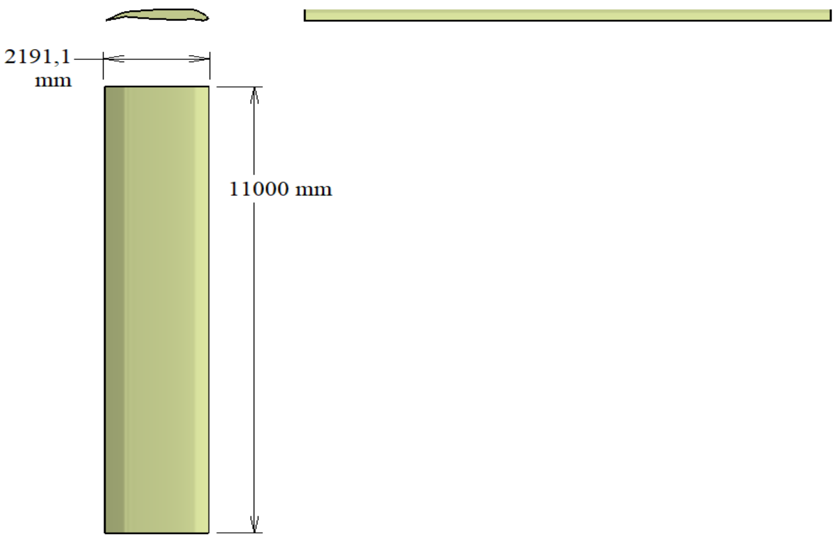

Figure 28: Wing measurements in CatiaV5.

4.2.3 Description of the mesh

FlightStream can automatically generate an unstructured surface mesh based on the imported CAD model. [8]

A convergence process has been performed to choose the mesh. An angle of attack of 10° has been used. First, for a wing edge tessellation edge size value of 0.05, the influence of the tessellation edge size value on the upper and lower wing surfaces of the wing has been studied. The case values of 0.058 are used as a reference to calculate the error percentages. This can be seen in Table 12.

Tessellation edge size	C_L (% error)	C_{Di} (% error)	C_{Do} (% error)	C_D (% error)
0.062	0.748 (1.267%)	0.0315 (1.254%)	0.01 (0%)	0.0415 (0.955%)
0.060	0.753 (0.594%)	0.0317 (0.627%)	0.01 (0%)	0.0417 (0.477%)
0.058	0.758	0.0319	0.01	0.0419

Table 12: Tessellation edge size analysis on the upper and lower surfaces ($\alpha = 10°$).

It was decided to use a tessellation edge size on the upper and lower surface of 0.06 since correct values were obtained. Subsequently, the influence of the tessellation edge size on the wing edge, Table 13, was studied. The case values of 0.03 are used as a reference to calculate the error percentages.

Tessellation edge size	C_L (% error)	C_{Di} (% error)	C_{Do} (% error)	C_D (% error)
0.05	0.753 (0.293%)	0.0317 (2.160%)	0.01 (0%)	0.0417 (1.651%)
0.04	0.752 (0.200%)	0.0317 (2.160%)	0.01 (0%)	0.0417 (1.651%)
0.03	0.751	0.0324	0.01	0.0424

Table 13: Tessellation edge size analysis on the wing edge ($\alpha = 10°$).

A tessellation edge size value of 0.04 has been chosen for the wing edge. Table 14 shows the values of the wing tessellation edge sizes used in FlightStream.

Wing area	Tessellation edge size
Upper surface	0.06
Lower surface	0.06
Wing edge	0.04

Table 14: Wing tessellation edge sizes in FlightStream.

It is important to equip the wing with the wake termination nodes and the trailing edge. Figure 29 shows the mesh used. The reference system is located at $1/4\%c$ of the airfoil in the centre of the wing.

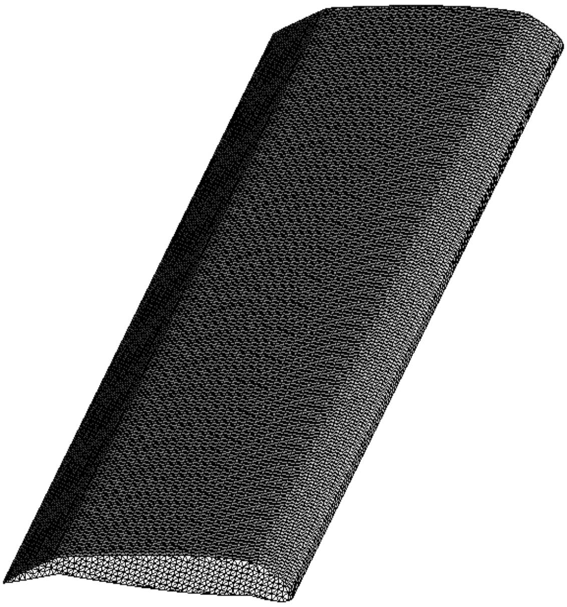

Figure 29: Wing mesh in FlightStream.

5 Results

This chapter describes the results, both numerical and graphical, obtained in the different study cases.

5.1 2-D analysis

The results obtained from the airfoil with the different high-lift devices under study are shown below.

5.1.1 High-lift trailing edge devices

First, the results obtained with the three high-lift trailing edge devices are compared. Figure 30 shows the C_l value for each angle of attack of the airfoil without flap and with the flaps.

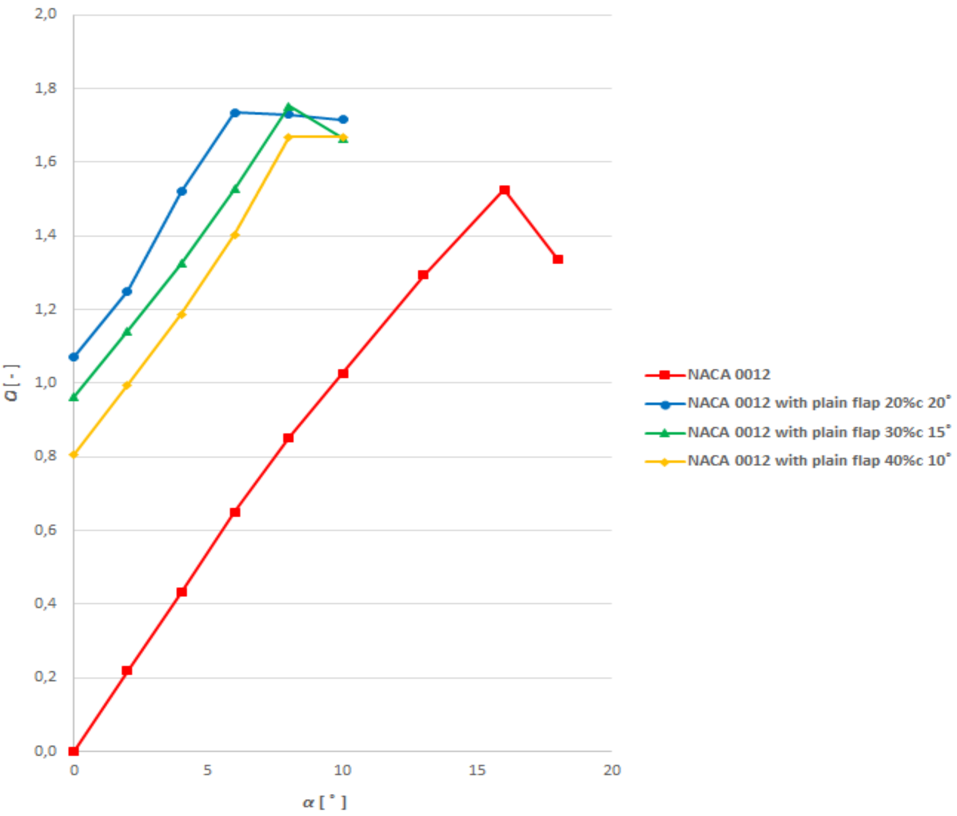

Figure 30: Comparison of the C_l values. Analysis of the different high-lift trailing edge devices.

Figure 30 shows that with the three high-lift trailing edge devices an increase in the C_l value for an angle of attack is obtained. Nevertheless, in all three cases the airfoil stalls earlier than in the case of the airfoil without flap. This can be solved by incorporating a high-lift leading edge device.

The high-lift trailing edge device with a length of 20%c and deflected 20° is the one with which the greatest increase in C_l is obtained.

Figure 31 shows the obtained values of C_d. It can be seen that with the incorporation of the flaps the value of C_d increases compared to that of the airfoil without flap for an angle of attack, however, this is not a large increase. The C_d values with each flap are similar.

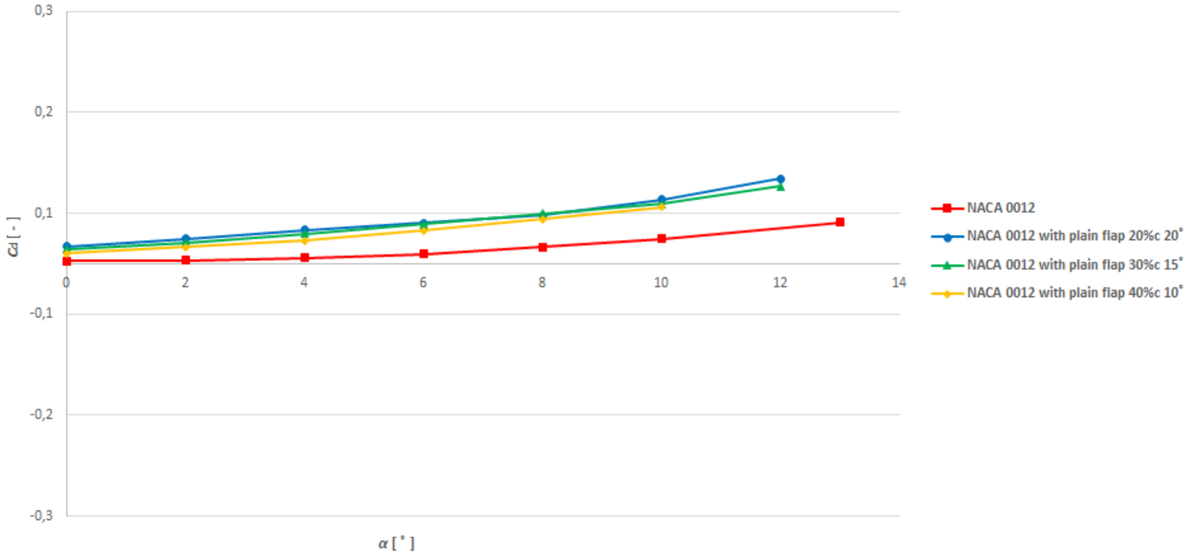

Figure 31: Comparison of the C_d values. Analysis of the different high-lift trailing edge devices.

Finally, Figure 32 shows the obtained values of C_m. It can be seen that with the incorporation of any of the flaps the value of C_m increases. Besides, it can be seen that with the increase of the angle of attack the value of C_m is reduced.

The increase in the C_m value with the incorporation of the high-lift devices makes it necessary to use the horizontal stabiliser to generate a moment in the opposite direction.

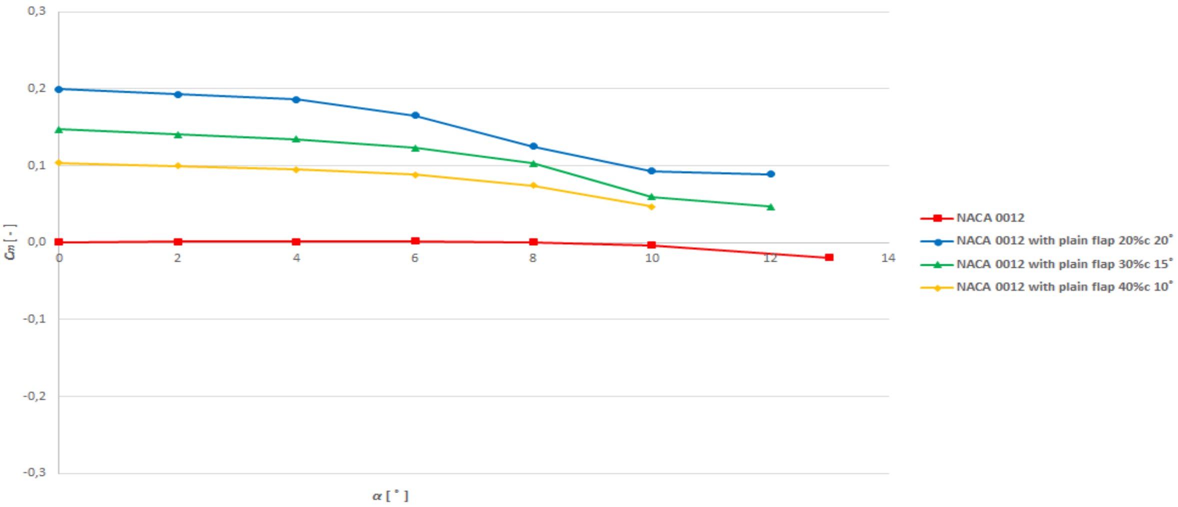

Figure 32: Comparison of the C_m values. Analysis of the different high-lift trailing edge devices.

It was decided to choose the high-lift trailing edge device with a length of 20%c and deflected 20° since it is the one with which a greater increase of C_l is obtained and the values of C_d are similar with the three flaps. The incorporation of a high-lift leading edge device is intended to increase the stall angle.

Figure 33 on the following page shows representations of different variables of the airfoil simulation with the high-lift trailing edge device chosen for an angle of attack of 10°.

In Figure 33a it can be seen that, for this angle of attack, the incorporation of the high-lift trailing edge device generates an increase in the velocity on the upper surface at the leading edge but there is also a further decrease in the velocity on the upper surface of the flap. The airfoil is in a state close to stall if we look at Figure 30. In Figure 33b it can be seen that with the incorporation of the device there is a greater difference in pressures.

On the other hand, in Figure 33c it can be seen that the turbulent viscosity is higher compared to the case of the airfoil without flap for this angle of attack.

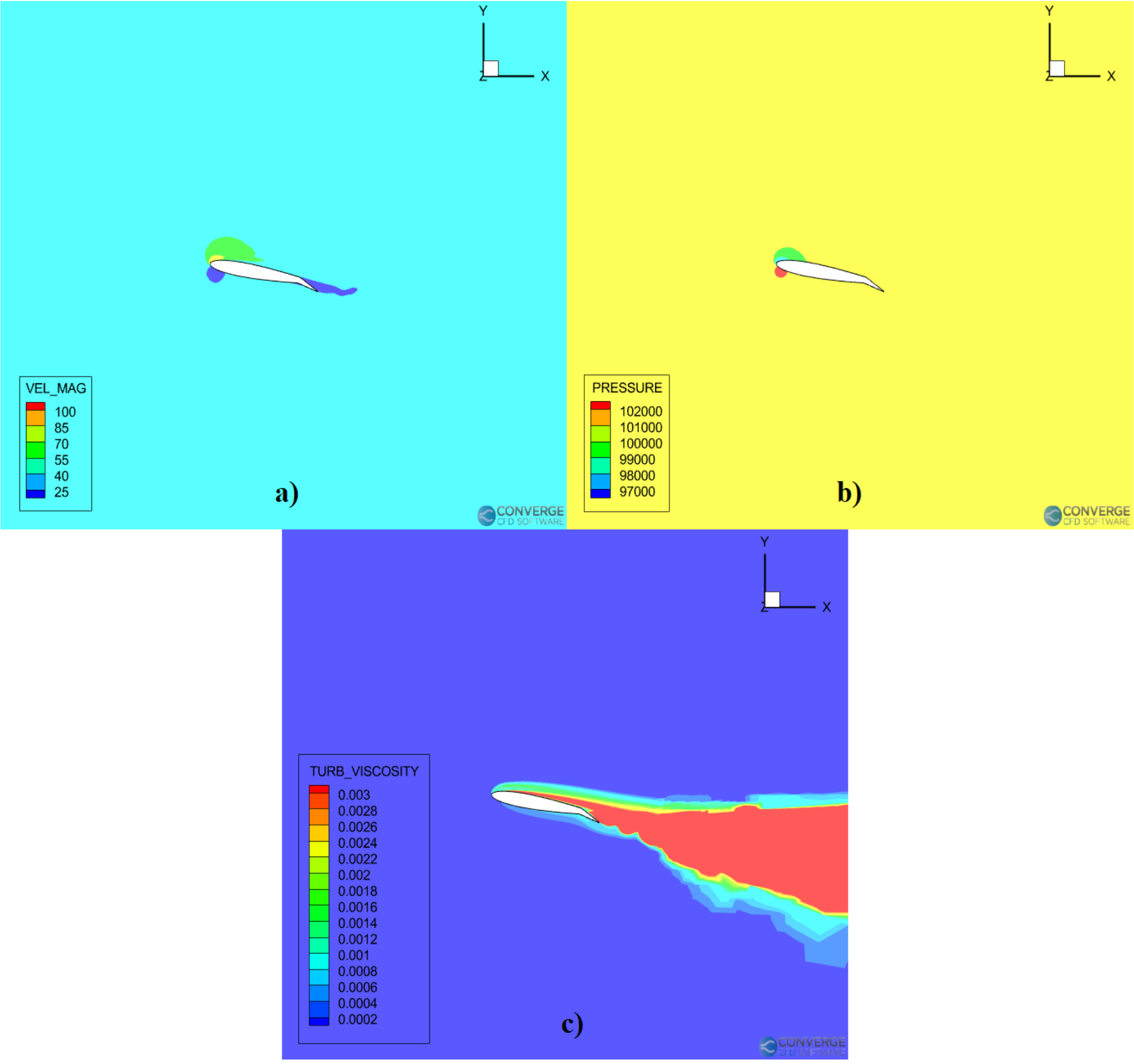

Figure 33: NACA0012 airfoil with a plain flap 20%c 20° ($\alpha = 10°$). a) Velocity representation (m/s). b) Pressure representation (Pa). c) Turbulent viscosity representation (m^2/s).

5.1.2 High-lift leading edge devices

The results obtained with the three high-lift leading edge devices are compared. Figure 34 shows the C_l value for each angle of attack of the airfoil without the leading edge flap and with it. In all cases, the previously selected high-lift trailing edge is deflected.

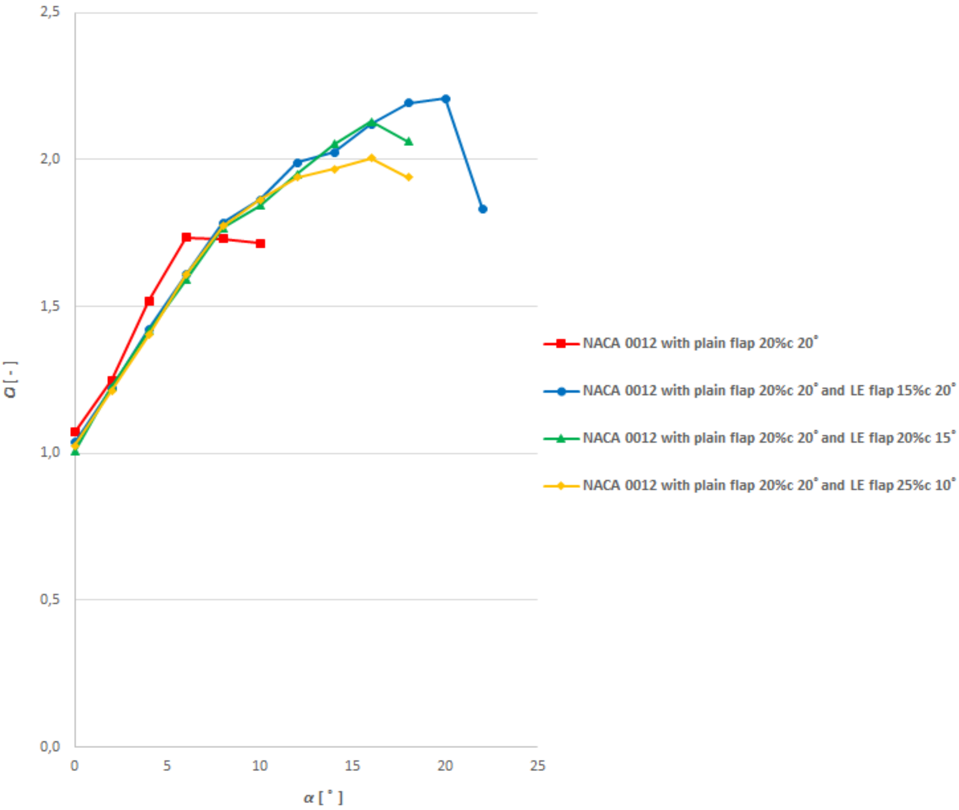

Figure 34: Comparison of the C_l values. Analysis of the different high-lift leading edge devices.

Figure 34 shows that with the three high-lift leading edge devices the C_{lmax} value increases and the airfoil stalls later than in the case of the airfoil without a leading flap. This solves the problem of having a low stall angle when only one high-lift trailing edge device is deflected.

With the high-lift leading edge device with a length of $15\%c$ and with a deflection angle of $20°$, the highest C_{lmax} and largest stall angle is achieved.

Figure 35 on the following page shows the obtained values of C_d. It can be seen that with the incorporation of the high-lift leading edge flap it is possible to reduce the C_d values. The results of the three cases are similar but with large angles of attack the C_d values with the leading edge flap with a length of $15\%c$ and with a deflection angle of $20°$ being slightly lower.

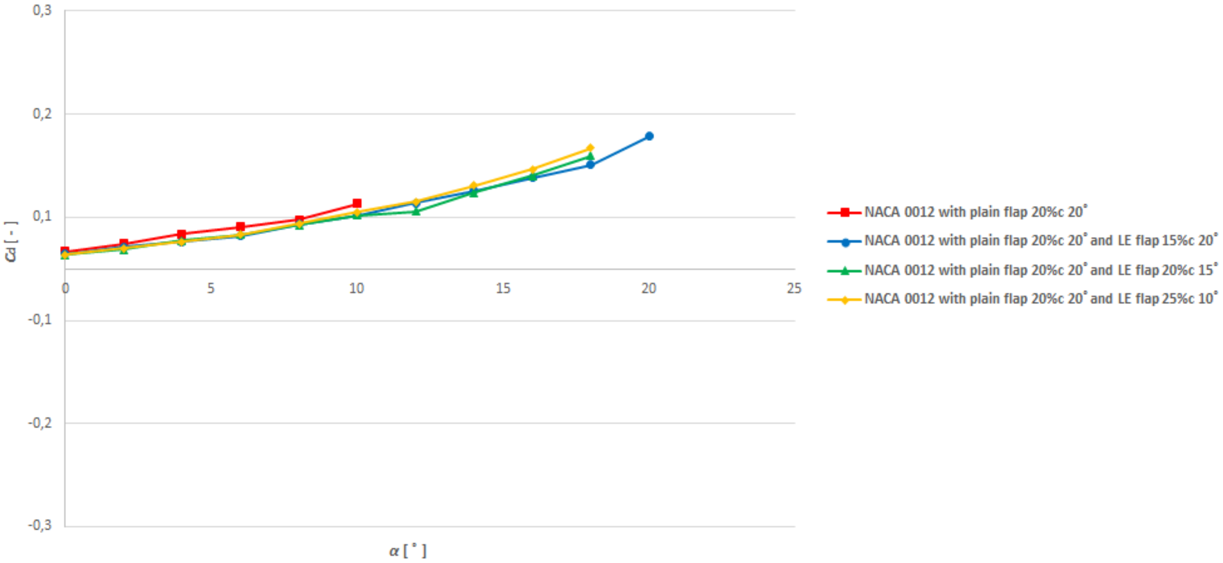

Figure 35: Comparison of the C_d values. Analysis of the different high-lift leading edge devices.

Finally, Figure 36 shows the obtained values of C_m. It can be seen that the C_m values increase and again the use of the horizontal stabiliser to generate a moment in the opposite direction should be analysed.

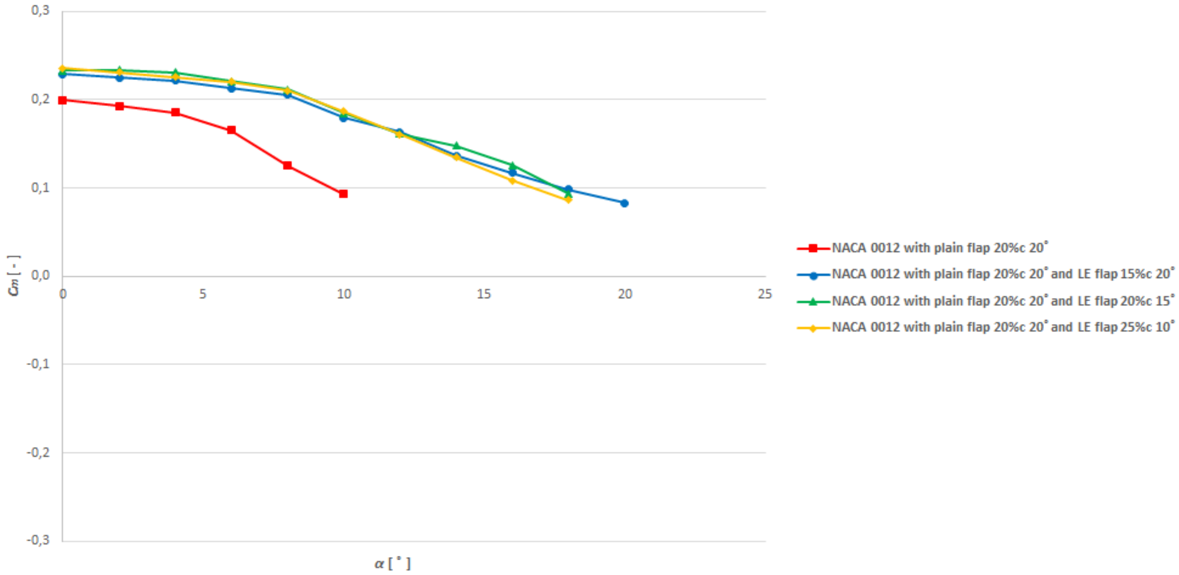

Figure 36: Comparison of the C_m values. Analysis of the different high-lift leading edge devices.

Thus, it was decided to choose the high-lift leading edge device with a length of 15%c and deflected 20° since it is the one with the highest C_{lmax} obtained, it stalls with a higher angle of attack and the C_d values are slightly lower.

Figure 37 shows representations of different variables of the airfoil simulation with the high-lift trailing edge and leading edge devices chosen for an angle of attack of 10°

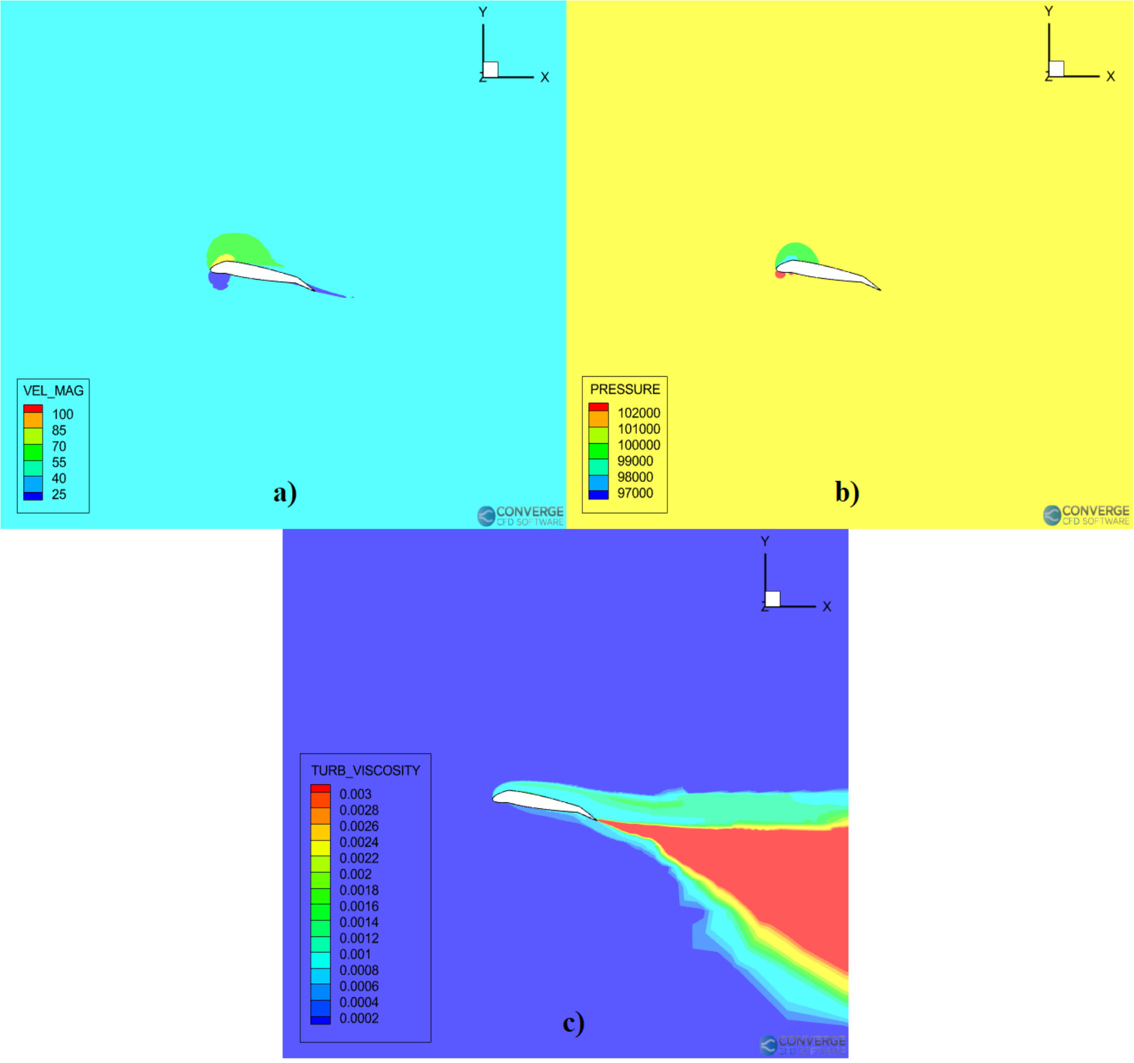

Figure 37: NACA0012 airfoil with a leading edge flap 15%c 20° and with a plain flap 20%c 20° ($\alpha = 10°$). a) Velocity representation (m/s). b) Pressure representation (Pa). c) Turbulent viscosity representation (m^2/s).

In Figure 37a it can be seen that with the use of the leading edge flap there is an increase in velocity on the upper surface at the leading edge and a reduction in velocity on the upper surface of the flap.

In Figure 37b it can be seen that with the incorporation of the leading edge flap there is an increase in the pressure difference.

Finally, if Figure 33c is compared with Figure 37c, a reduction in turbulent viscosity can be seen on the upper surface of the airfoil.

5.2 3-D analysis

An aircraft's wing is the lifting surface with the chosen airfoil section, which can vary spanwise. The lift generated by the wing sustains the weight of the aircraft to make flight possible. [20]

Figure 38 shows the C_L and C_D values obtained with the wing with the undeflected devices using FlightStream software. Also, Figure 38 shows a zoom of the values with zero angle of attack.

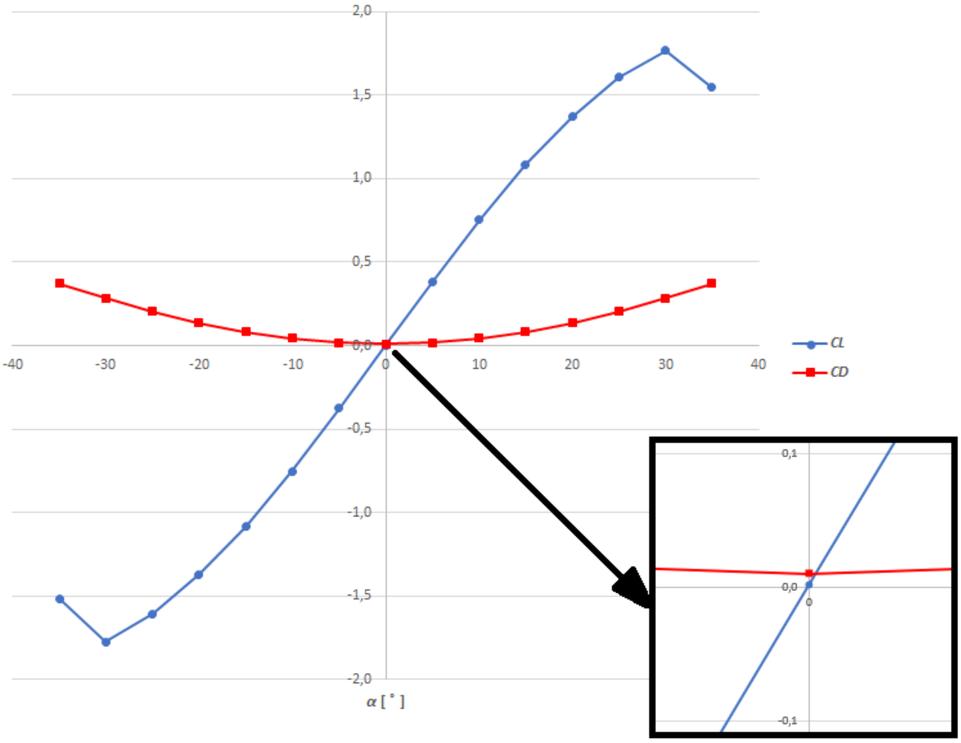

Figure 38: Wing results with undeflected high-lift devices.

An important issue is to analyze the simulation residuals to ensure that converged values are obtained. As mentioned above, the residual is one of the most fundamental measures of an iterative solution's convergence, as it directly quantifies the error in the solution of the system of equations. For CFD, residual levels of 10^{-4} are considered to be loosely converged, levels of 10^{-5} are considered to be well converged, and levels of 10^{-6} are considered to be tightly converged. [21]

Figure 39 shows the residuals obtained and how low values are obtained, concluding that the results are correct.

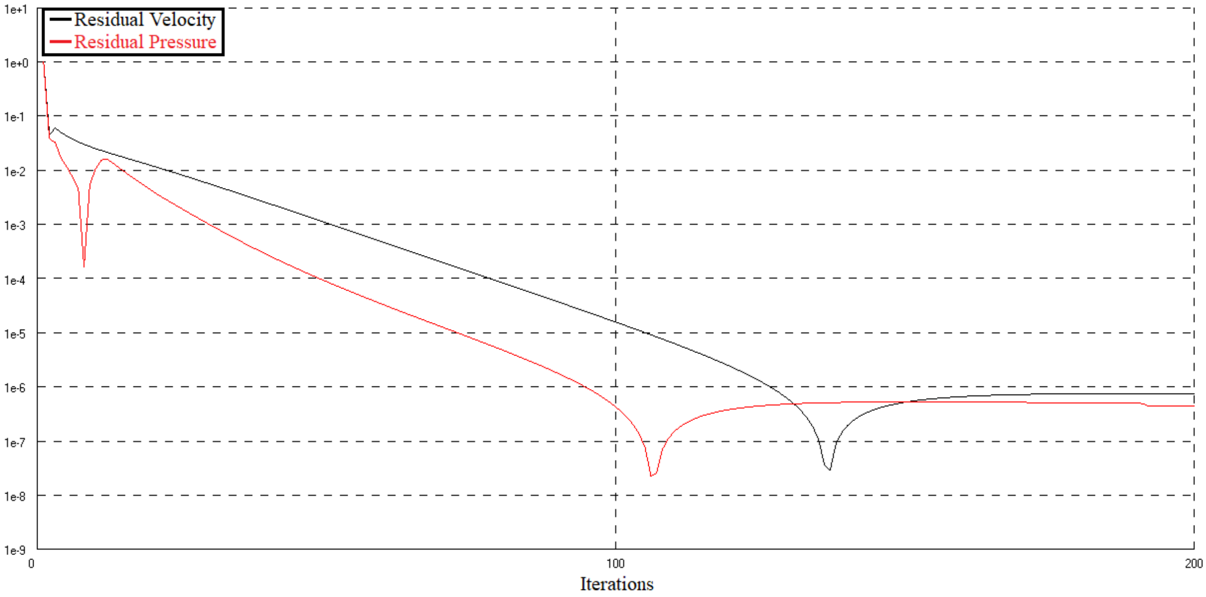

Figure 39: Residuals of the wing with undeflected high-lift devices case.

After obtaining the results for the wing with the undeflected high-lift devices, the wing with the deflected devices is simulated. Figure 40 shows the C_L and C_D values obtained. Again a zoom of the values is shown.

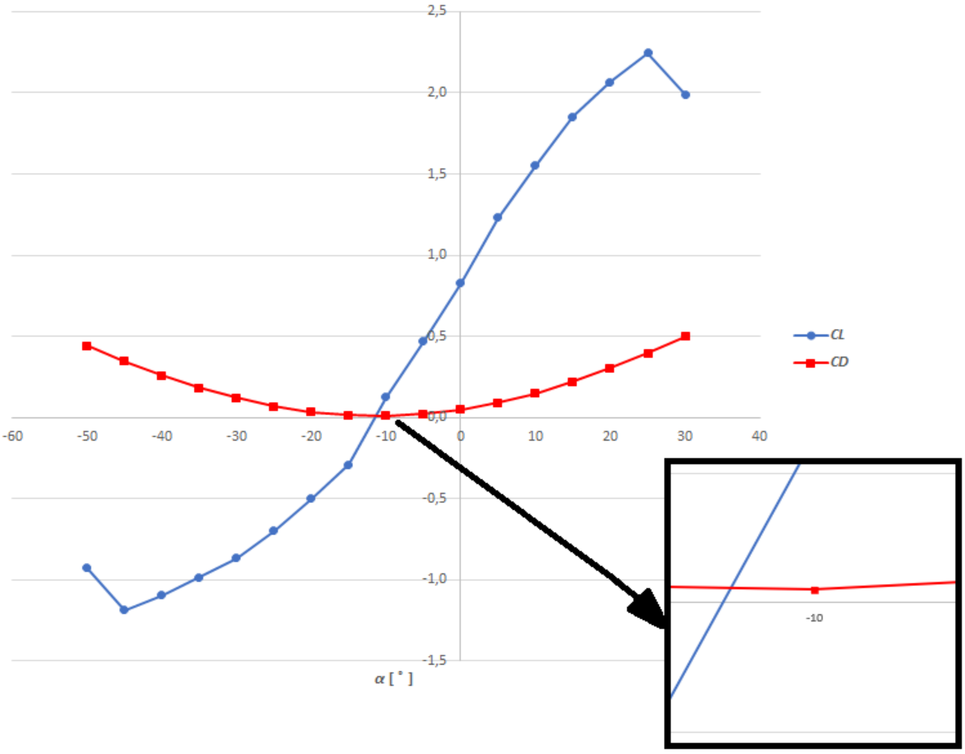

Figure 40: Wing results with deflected high-lift devices.

Figure 41 shows the residuals obtained for this case and again concludes that the results are correct.

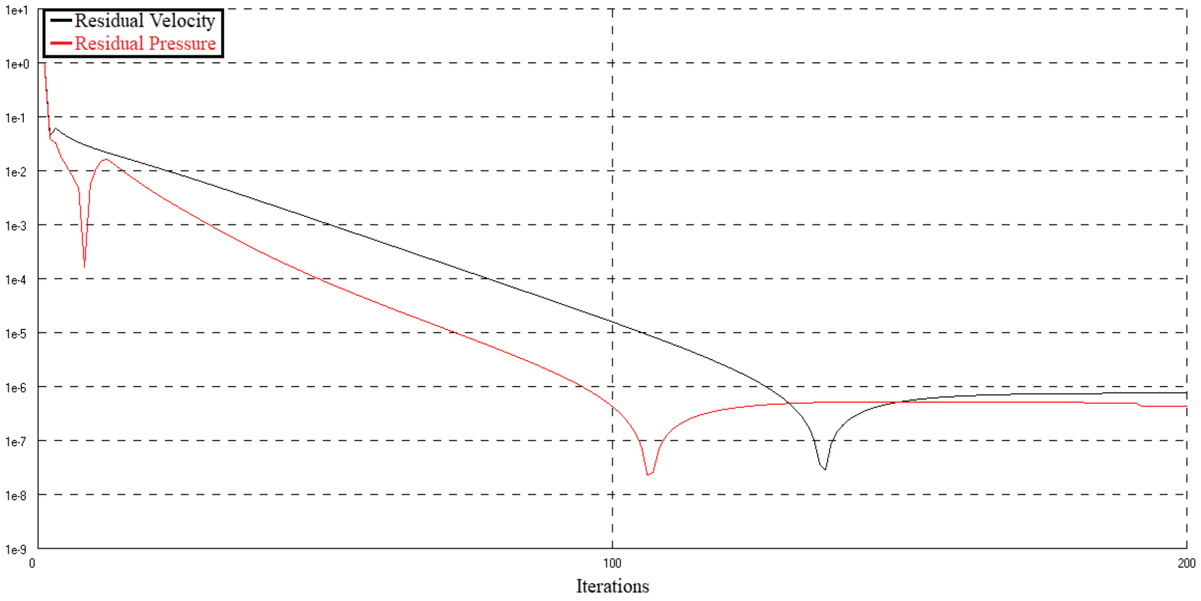

Figure 41: Residuals of the wing with deflected high-lift devices case.

The results obtained in both cases are compared below. In Figure 42 it can be seen that with deflected high-lift devices the C_L values are increased without increasing the C_D values too much.

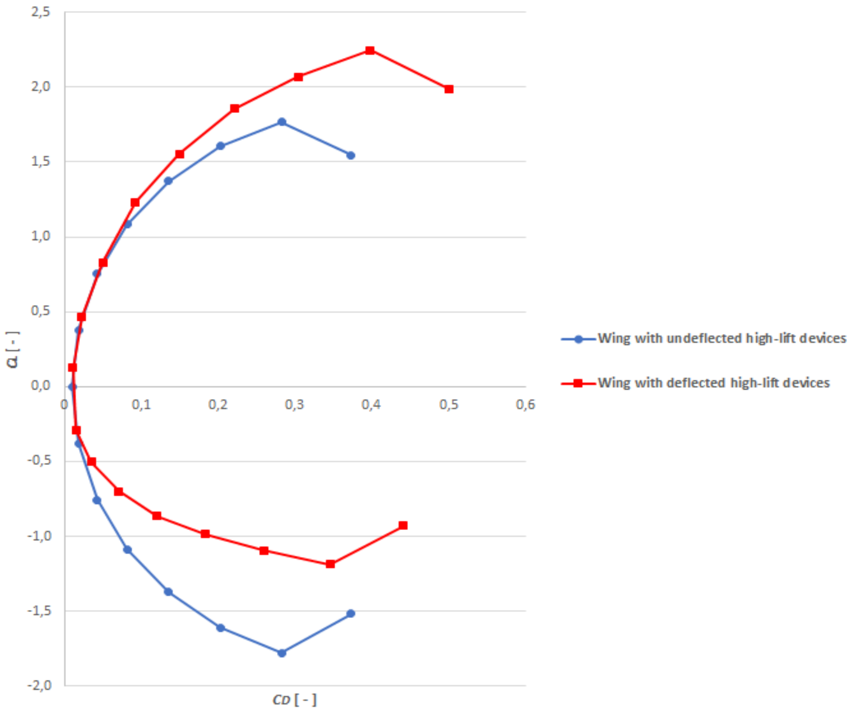

Figure 42: Comparative C_L - C_D graph of the wing with deflected and undeflected high-lift devices.

For each point of each polar, the slope of the straight line passing through that point and the origin is the aerodynamic efficiency of the airfoil. It is observed that with deflected high-lift devices, higher aerodynamic efficiency is obtained.

After analyzing the results obtained, representations of the wing simulation are shown. Figure 43 shows the simulation of the wing with undeflected high-lift devices.

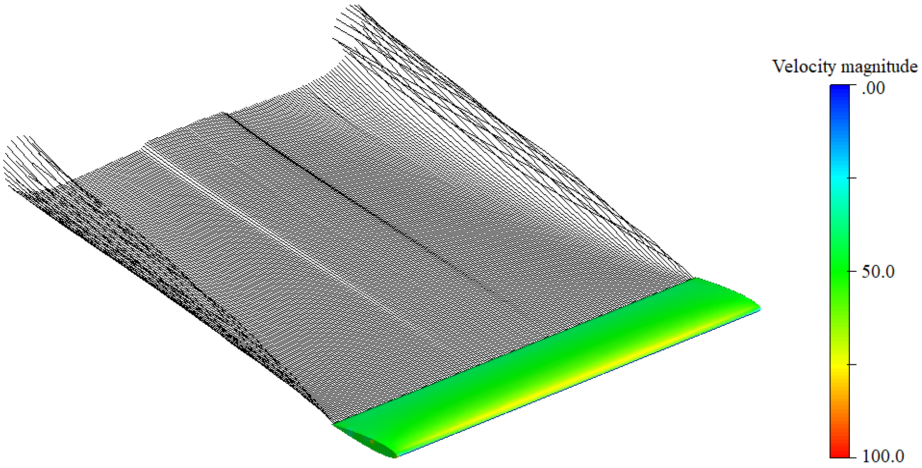

Figure 43: Wing with undeflected high-lift devices in FlightStream. Velocity representation (m/s). ($\alpha = 10°$).

Figure 43 shows that vortices are generated at the wing tips. A 3D finite wing produces vortex flow as a result of tip effects. The high pressure from the lower surface rolls up at the free end of the finite wing, creating the tip vortex. [20] Figure 44 shows the simulation of the wing with the deflected high-lift devices.

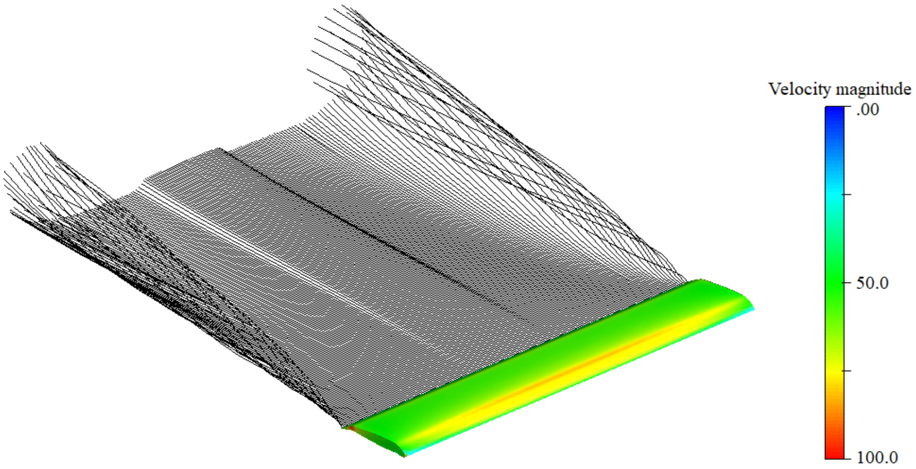

Figure 44: Wing with deflected high-lift devices in FlightStream. Velocity representation (m/s). ($\alpha = 10°$).

In Figure 44 it can be seen that the vortices are larger with the addition of the high-lift devices. The difference in the vortices can best be seen in Figure 45. The vortices generated are related to the values of the induced drag coefficient, which is higher with deflected high-lift devices.

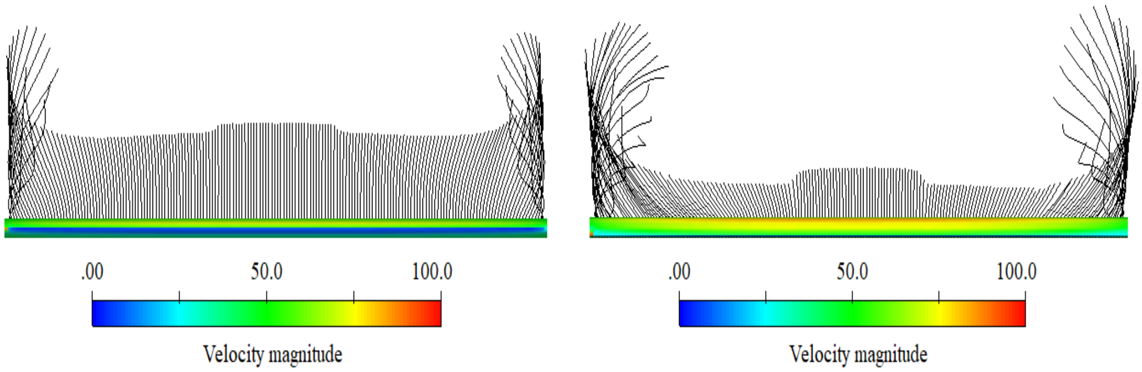

(a) Undeflected high-lift devices.

(b) Deflected high-lift devices.

Figure 45: Velocity representation (m/s).

In both cases, the wing has a cut-off tip and it offers less drag than a rounded-off tip. A smoothly-rounded tip easily permits the air to flow around the tip. A tip with a sharp edge makes it more difficult, thus reducing the induced drag. [4]

Most of the new low-drag wing tips use some form of sharp edge. A widely used device is the winglet which is a curved and twisted device so that the rotating vortex flow in the wingtip creates a lift force on the winglet that has a forward component. This forward lift component acts as a "negative" drag, reducing the overall drag of the wing, Figure 46. [4]

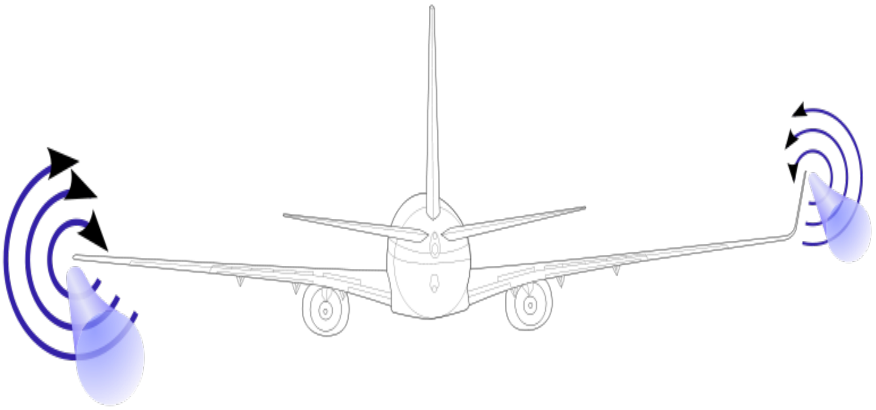

Figure 46: Reduction of vortex size with the use of winglets. [22]

6 Conclusions

CFD analysis has great potential and offers many advantages. Simulation provides low cost compared to full-scale or reduced-scale model tests. There is also the freedom to impose boundary conditions and information is obtained for different variables at any point in space, which is more complicated in experiments. Even so, the results must be accompanied by real experiments such as those performed in wind tunnels to be validated.

First of all, CONVERGE CFD software allows to perform CFD simulations quite accurately. It has also been proven that Tecplot for CONVERGE allows to visualize the simulations performed by obtaining graphical results of different parameters.

With the 2D CFD analysis performed in this work, it has been possible to study the influence of the passive high-lift trailing edge and leading edge devices on the lift, drag and moment of an airfoil. It has been demonstrated that CONVERGE can be used quite reliably to study how the different parameters of these devices affect numerically in real cases.

In the 2D CFD analysis, the PISO solver has been used since it gives correct results and is less "expensive" than the SIMPLE solver. As for the turbulent model, $k-\omega$ SST has been used since it gives results closer to the experimental results compared to the $k-\varepsilon$. This was one of the analyses performed in my previous work.

The high-lift devices are used in take-off, approach and landing manoeuvres. Several conclusions have been obtained with the use of high-lift devices from the work which is detailed below.

With the incorporation of high-lift trailing edge devices, the value of C_l for a given angle of attack increases. Nevertheless, the airfoil stalls earlier than in the case of the airfoil without flap. The addition of the study flaps increases the C_d values but not by much. Moreover, the C_m value increases with the addition of any of the flaps but with the increase of the angle of attack the value of C_m decreases. The increase in the value of C_m with the incorporation of the high-lift trailing edge devices makes it necessary to use the horizontal stabiliser to generate a moment in the opposite direction.

It has been decided to choose the high-lift trailing edge device with a length of 20%c and deflected 20° as it gives the highest C_l increase and the C_d values are similar for all three flaps.

As for the leading edge devices, with all three study devices the C_{lmax} value increases and the airfoil stalls later than in the case of the airfoil without a leading edge flap. This solves the problem of having a low stall angle when only one high-lift trailing edge device is deflected. Furthermore, it has been shown that with the addition of the high-lift leading edge flap it is possible to reduce the C_d values. Again the use of the horizontal stabiliser to generate a moment in the opposite direction should be analysed.

Thus, it has been decided to choose the high-lift leading edge device with a length of 15%c and deflected 20° as it has the highest C_{lmax}, stalls at a higher angle of attack and the C_d values are slightly lower.

After the choice of the passive high-lift leading and trailing edge devices, a 3D analysis was performed with FlightStream software. FlightStream allows to perform 3D CFD simulations that simulate situations quickly and easily.

The residuals of the simulations performed have been analysed. The residual is a fundamental measure of convergence of an iterative solution and it has been used to confirm that the results are correct.

With deflected high-lift devices on the wing, the C_L values are increased without increasing the C_D values too much. It is observed that with deflected high-lift devices on the wing a higher aerodynamic efficiency is obtained for take-off performance.

Finally, it has been shown that vortices are generated at the wing tips. The vortices generated are related to the values of the induced drag coefficient, which are higher with deflected high-lift devices.

As for future work, slotted high-lift devices could be incorporated into the airfoil to improve aerodynamic efficiency. In addition, the wing could be improved by incorporating aileron sections, having flaps with a certain wing length and having the mechanical devices that allow the flaps to deflect. Also, wings with variable chord, wing sweep, wing dihedral or with wing tips could be analysed and compared.

It should be noted that studies and experiments are being carried out with deformable wings that modify their curvature and allow the configuration of the aircraft to be optimised at each phase of the flight.

References

[1] Torenbeek, E. (1982). *Synthesis of Subsonic Airplane Design.* Delft: Delft University Press.

[2] Gordillo, J.M. and Riboux, G. (2012). *Introducción a la Aerodinámica Potencial.* Madrid: Paraninfo.

[3] Abbott, I.H. and Von Doenhoff, A.E. (1959). *Theory Of Wing Sections.* New York: Dover Publications, Inc.

[4] Raymer, D.P. (1992). *Aircraft Design: A Conceptual Approach.* (2ª ed.). EEUU: AIAA Education Series.

[5] AGARD - Advisory Group For Aerospace Research & Development (1992). *High-Lift System Aerodynamics.* Canada: North Atlantic Treaty Organization.

[6] Airliners. Bombardier CRJ-900 NG (CL-600-2D24) - Lufthansa Regional (Lufthansa CityLine). URL: `https://www.airliners.net/photo/Lufthansa-Regional-Lufthansa-CityLine/Bombardier-CRJ-900-NG-CL-600-2D24/2640222?qsp=eJwtjDEOwkAMBP/imgokinTwgVDwAcu3QMTBWbYlOEX5O3ch3eysNDNJeQe%2Bca0KGsjBJg/akbLxy2mY6Yn6KZYa0y2zeju9WJxrE4kDJxFoIG1%2BtATrF1zWzr139x1hl/86HNtMk2vmtYLgKdOy/ACCTi72`, consulted on 20/03/2021.

[7] CONVERGE CFD SOFTWARE. HIGH-PERFORMANCE COMPUTING. URL: `https://convergecfd.com`, consulted on 21/03/2021.

[8] FlightStream. Aerodynamic Modeling Software. URL: `https://www.darcorp.com/flightstream-aerodynamics-software/`, consulted on 21/03/2021.

[9] Cid Escobar, P.G. (2018). *Análisis CFD del efecto de los dispositivos hipersustentadores pasivos de borde de salida en un perfil aerodinámico.* Universidad de Cádiz: Cádiz.

[10] Airfoil Tools. NACA 0012 AIRFOILS. URL: `http://airfoiltools.com/airfoil/details?airfoil=n0012-il`, consulted on 14/03/2021.

[11] Critzos, C.C.; Heyson, H.H. and Boswinkle, R.W.Jr. (1955). *Technical Note 3361. Aerodynamic characteristics of NACA 0012 airfoil section at angles of attack from 0º to 180º.* National Advisory Committee for Aeronautics.

[12] CONVERGE CFD SOFTWARE. *CONVERGE MANUAL.* CONVERGE CFD Manual Series.

[13] Wilhelm Riegels, F. (1958). *Aerofoil Sections.* Munich: London Butterworths.

[14] Cessna Aircraft Company (1978). *Skyhawk. Cessna Model 172N. Pilot's Operating Handbook.* Kansas: Cessna.

[15] CONVERGE CFD SOFTWARE. *Grid Control. Introduction to CONVERGE. Session 6/16.*

[16] CFD Online. Y plus wall distance estimation. URL: `https://www.cfd-online.com/Wiki/Y_plus_wall_distance_estimation`, consulted on 07/05/2021.

[17] Bakker, A. (2006). *Lecture 11 - Boundary Layers and Separation.* Applied Computational FluidDynamics.

[18] Pointwise. Compute Grid Spacing for a Given Y^+. URL: `https://www.pointwise.com/yplus/`, consulted on 06/05/2021.

[19] XFLR5. General description. URL: `http://www.xflr5.tech/xflr5.htm`, consulted on 01/06/2021.

[20] Kundu, A.K. (2010). *Aircraft Design.* New York: Cambridge University Press.

[21] Engineering. 3 Criteria for Assessing CFD Convergence. URL: `https://www.engineering.com/story/3-criteria-for-assessing-cfd-convergence`, consulted on 01/06/2021.

[22] Aviation. What do winglets do to increase aircraft performance? URL:`https://aviation.stackexchange.com/questions/2111/what-do-winglets-do-to-increase-aircraft-performance`, consulted on 01/06/2021.

A Annex A: Use of the software

This Annex explains how to use the software used in the work.

CONVERGE CFD

Firstly, the CAD file previously created is imported. Catia V5 has been used to obtain the CAD. In Catia V5 the coordinates of the airfoil are imported. Then, the points are joined with splines, the airfoil is projected a distance equal to 1 meter, and finally, the upper and lower surfaces of the airfoil are filled. It is necessary that the airfoil has a length in the Z-direction as the software works in 3D, Figure 47.

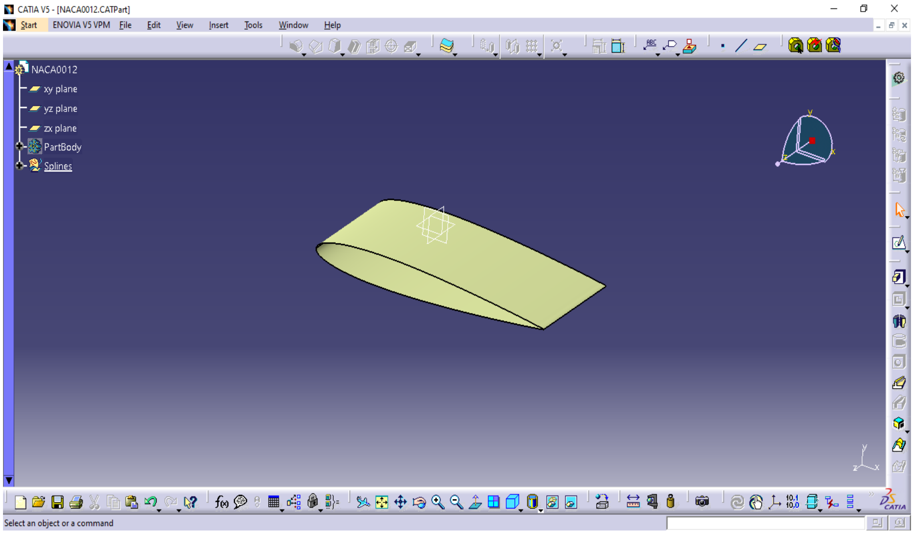
CATIA V5 - [NACA0012.CATPart]
Start
ENOVIA V5 VPM
File
Edit
View
Insert
Tools
Window
Help
NACA0012
xy plane
yz plane
zx plane
PartBody
Splines
Select an object or a command

Figure 47: CAD created in CatiaV5.

After importing the CAD file into CONVERGE Studio, Figure 48, the geometry of the domain is created.

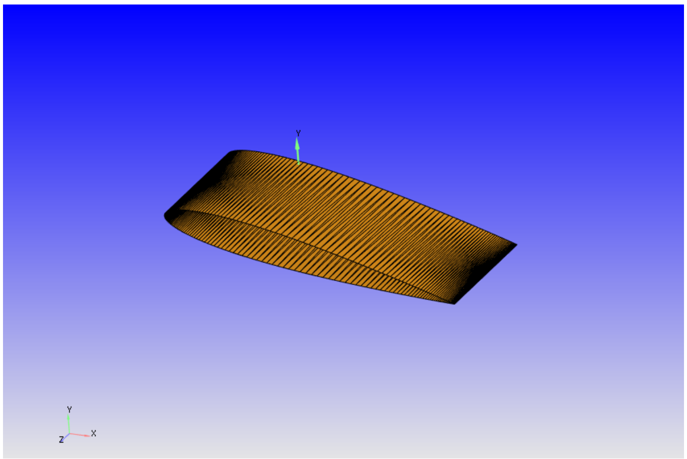

Figure 48: Airfoil imported into CONVERGE Studio.

The *Geometry Dock* section is used to create the geometry. After creating the geometry, the boundary conditions are created, Figure 49.

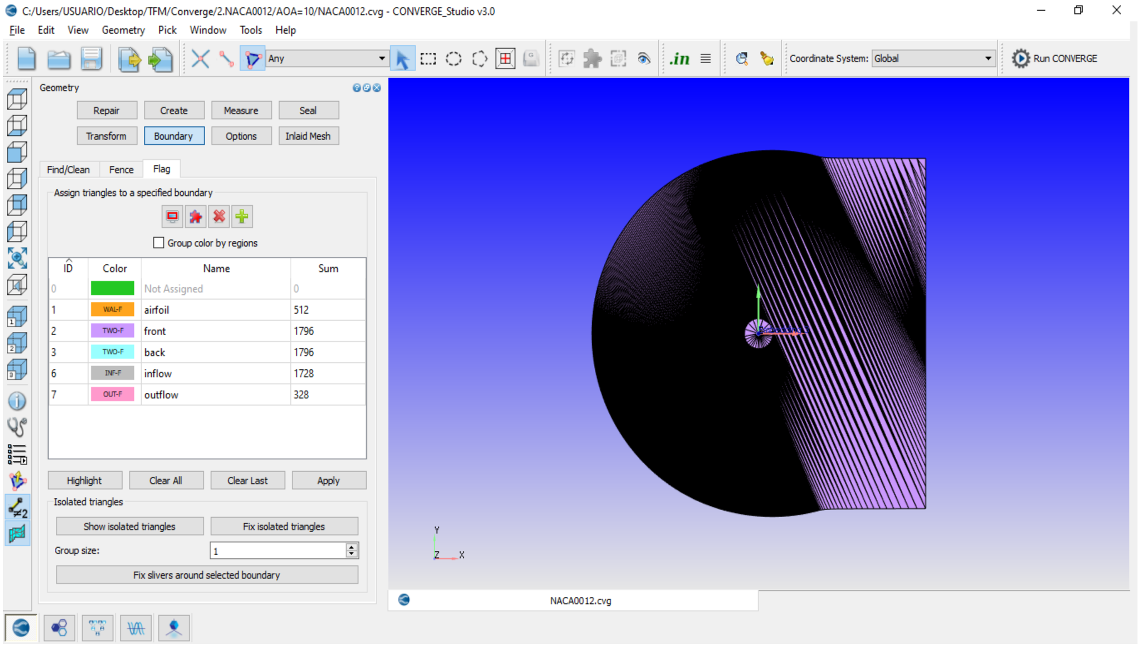
C:/Users/USUARIO/Desktop/TFM/Converge/2.NACA0012/AOA=10/NACA0012.cvg - CONVERGE_Studio v3.0
File
Edit
View
Geometry
Pick
Window
Tools
Help
Any
Coordinate System:
Global
Run CONVERGE
Geometry
Repair
Create
Measure
Seal
Transform
Boundary
Options
Inlaid Mesh
Find/Clean
Fence
Flag
Assign triangles to a specified boundary
☐ Group color by regions
Highlight
Clear All
Clear Last
Apply
Isolated triangles
Show isolated triangles
Fix isolated triangles
Group size:
1
Fix slivers around selected boundary
Y
Z
X
NACA0012.cvg

ID	Color	Name	Sum
0	🟩	Not Assigned	0
1	WAL-F	airfoil	512
2	TWO-F	front	1796
3	TWO-F	back	1796
6	INF-F	inflow	1728
7	OUT-F	outflow	328

Figure 49: Geometry with the boundary conditions created in CONVERGE Studio.

The Case Setup is then started. Click on the list of categories and for each category, select the relevant models or options for this case, Figure 50.

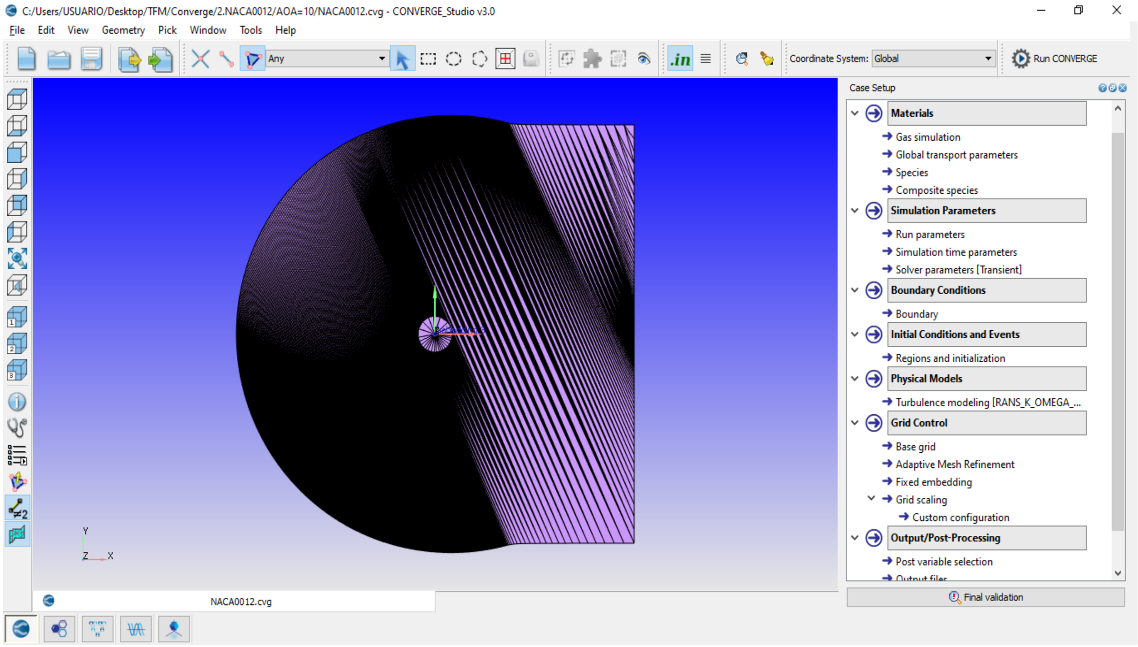
C:/Users/USUARIO/Desktop/TFM/Converge/2.NACA0012/AOA=10/NACA0012.cvg - CONVERGE_Studio v3.0
File
Edit
View
Geometry
Pick
Window
Tools
Help
Any
Coordinate System:
Global
Run CONVERGE
Case Setup
Materials
Gas simulation
Global transport parameters
Species
Composite species
Simulation Parameters
Run parameters
Simulation time parameters
Solver parameters [Transient]
Boundary Conditions
Boundary
Initial Conditions and Events
Regions and initialization
Physical Models
Turbulence modeling [RANS_K_OMEGA_...
Grid Control
Base grid
Adaptive Mesh Refinement
Fixed embedding
Grid scaling
Custom configuration
Output/Post-Processing
Post variable selection
Final validation
Y
Z
X
NACA0012.cvg

Figure 50: Case setup creation in CONVERGE Studio.

First of all, the *Materials* options are completed. Figure 51 shows the parameters chosen in this section.

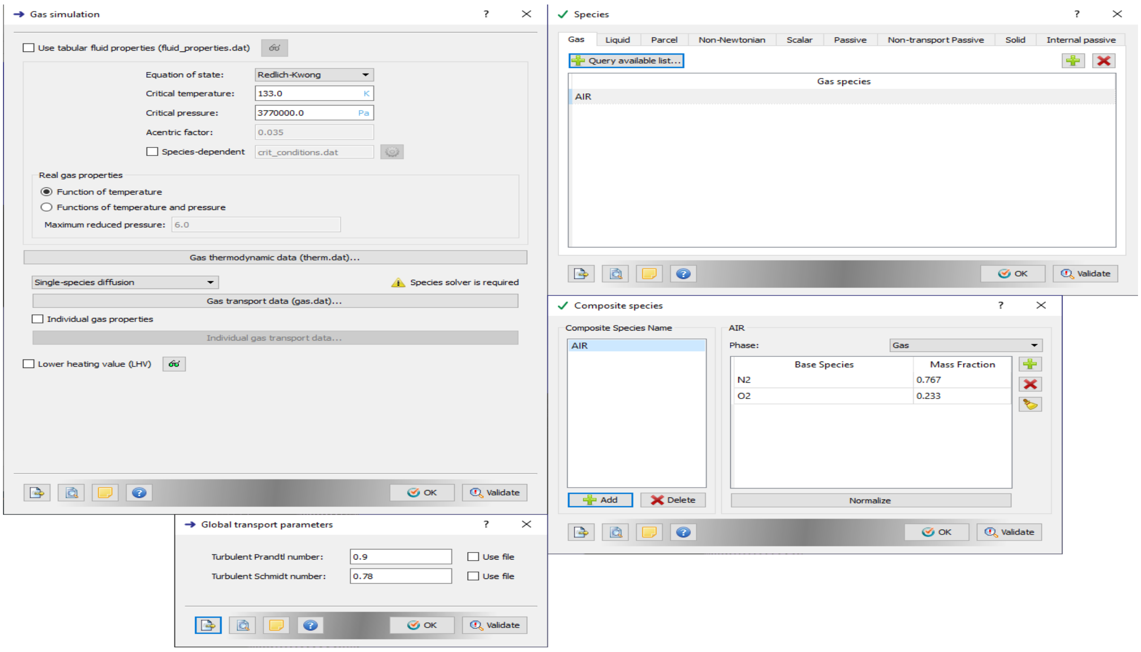
Gas simulation
Species
Gas
Liquid
Parcel
Non-Newtonian
Scalar
Passive
Non-transport Passive
Solid
Internal passive
Query available list...
Composite species
Add
Delete
Normalize
Global transport parameters
Gas thermodynamic data (therm.dat)...
Gas transport data (gas.dat)...
Individual gas transport data...
OK
Validate

Gas simulation

☐ Use tabular fluid properties (fluid_properties.dat)

Equation of state: Redlich-Kwong

Critical temperature: 133.0 K

Critical pressure: 3770000.0 Pa

Acentric factor: 0.035

☐ Species-dependent crit_conditions.dat

Real gas properties

● Function of temperature

○ Functions of temperature and pressure

Maximum reduced pressure: 6.0

Single-species diffusion — Species solver is required

☐ Individual gas properties

☐ Lower heating value (LHV)

Species — Gas species: AIR

Composite species

Composite Species Name: AIR

AIR — Phase: Gas

Base Species	Mass Fraction
N2	0.767
O2	0.233

Global transport parameters

Turbulent Prandtl number: 0.9 ☐ Use file

Turbulent Schmidt number: 0.78 ☐ Use file

Figure 51: Materials options in CONVERGE Studio.

The *Simulation Parameters* are then configured. A transient solver, the Navier Stokes solver PISO, is used. Figure 52 shows different parameters of the simulation.

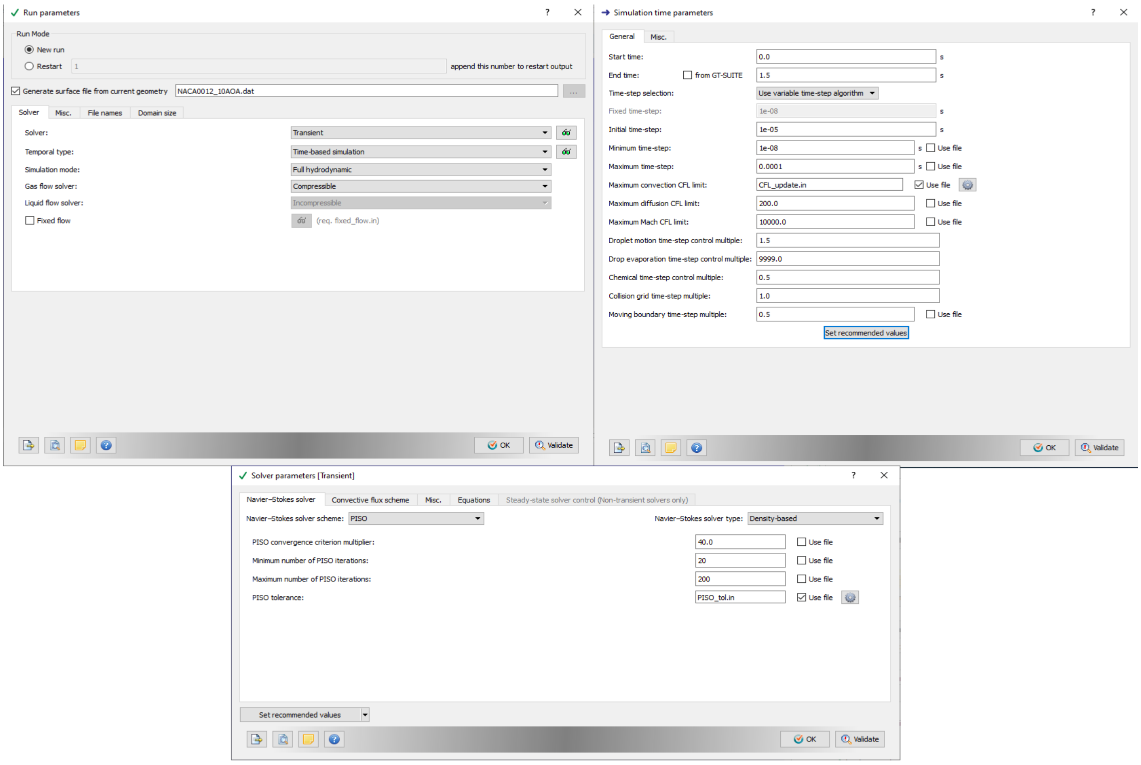
Run parameters
Solver
Misc.
File names
Domain size
Simulation time parameters
General
Misc.
Set recommended values
Solver parameters [Transient]
Navier–Stokes solver
Convective flux scheme
Misc.
Equations
Steady-state solver control (Non-transient solvers only)
OK
Validate

Run parameters

Run Mode

● New run

○ Restart 1 append this number to restart output

☑ Generate surface file from current geometry NACA0012_10AOA.dat

Solver: Transient

Temporal type: Time-based simulation

Simulation mode: Full hydrodynamic

Gas flow solver: Compressible

Liquid flow solver: Incompressible

☐ Fixed flow (req. fixed_flow.in)

Simulation time parameters

Start time: 0.0 s

End time: ☐ from GT-SUITE 1.5 s

Time-step selection: Use variable time-step algorithm

Fixed time-step: 1e-08 s

Initial time-step: 1e-05 s

Minimum time-step: 1e-08 s ☐ Use file

Maximum time-step: 0.0001 s ☐ Use file

Maximum convection CFL limit: CFL_update.in ☑ Use file

Maximum diffusion CFL limit: 200.0 ☐ Use file

Maximum Mach CFL limit: 10000.0 ☐ Use file

Droplet motion time-step control multiple: 1.5

Drop evaporation time-step control multiple: 9999.0

Chemical time-step control multiple: 0.5

Collision grid time-step multiple: 1.0

Moving boundary time-step multiple: 0.5 ☐ Use file

Solver parameters [Transient]

Navier–Stokes solver scheme: PISO

Navier–Stokes solver type: Density-based

PISO convergence criterion multiplier: 40.0 ☐ Use file

Minimum number of PISO iterations: 20 ☐ Use file

Maximum number of PISO iterations: 200 ☐ Use file

PISO tolerance: PISO_tol.in ☑ Use file

Figure 52: Simulation parameters in CONVERGE Studio.

The characteristics of the previously created boundary conditions continue to be completed in the section *Boundary Conditions*, Figure 53.

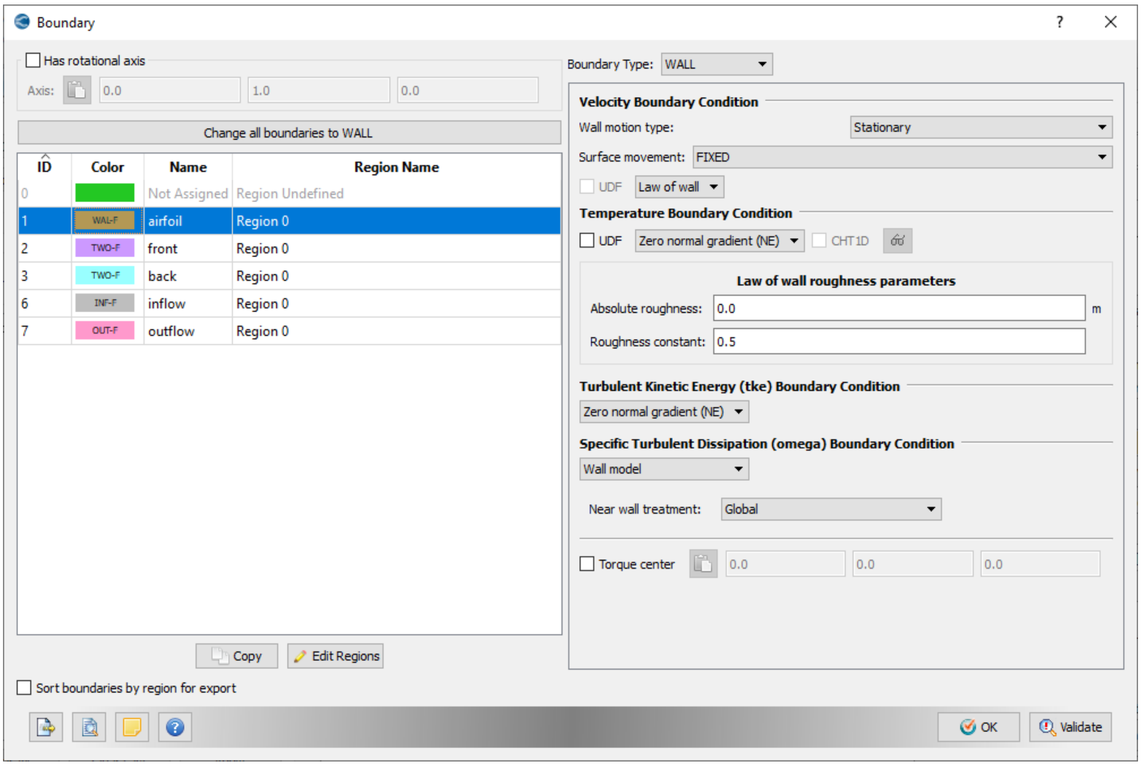

Boundary

☐ Has rotational axis

Axis: 0.0 1.0 0.0

Change all boundaries to WALL

ID	Color	Name	Region Name
0	🟩	Not Assigned	Region Undefined
1	WALL-F	airfoil	Region 0
2	TWO-F	front	Region 0
3	TWO-F	back	Region 0
6	INF-F	inflow	Region 0
7	OUT-F	outflow	Region 0

☐ Sort boundaries by region for export

Boundary Type: WALL

Velocity Boundary Condition

Wall motion type: Stationary

Surface movement: FIXED

☐ UDF Law of wall

Temperature Boundary Condition

☐ UDF Zero normal gradient (NE) ☐ CHT1D

Law of wall roughness parameters

Absolute roughness: 0.0 m

Roughness constant: 0.5

Turbulent Kinetic Energy (tke) Boundary Condition

Zero normal gradient (NE)

Specific Turbulent Dissipation (omega) Boundary Condition

Wall model

Near wall treatment: Global

☐ Torque center 0.0 0.0 0.0

Figure 53: Boundary conditions in CONVERGE Studio.

The region is also created with the initial conditions of the case, *Initial Conditions and Events* section, Figure 54.

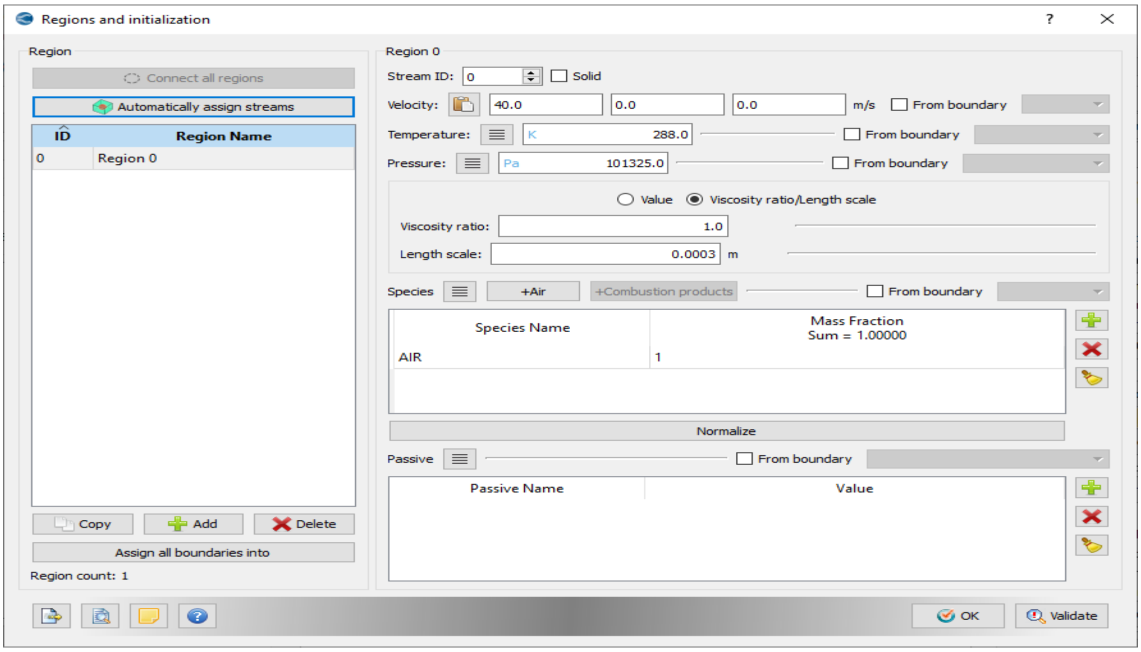

Regions and initialization

Region

ID	Region Name
0	Region 0

Region count: 1

Region 0

Stream ID: 0 ☐ Solid

Velocity: 40.0 0.0 0.0 m/s ☐ From boundary

Temperature: K 288.0 ☐ From boundary

Pressure: Pa 101325.0 ☐ From boundary

○ Value ● Viscosity ratio/Length scale

Viscosity ratio: 1.0

Length scale: 0.0003 m

Species +Air +Combustion products ☐ From boundary

Species Name	Mass Fraction Sum = 1.00000
AIR	1

Normalize

Passive ☐ From boundary

Passive Name	Value

Figure 54: Initial conditions in CONVERGE Studio.

As mentioned above, the turbulent model used is the $k - \omega$ SST model. Figure 55 shows the parameters used with this model.

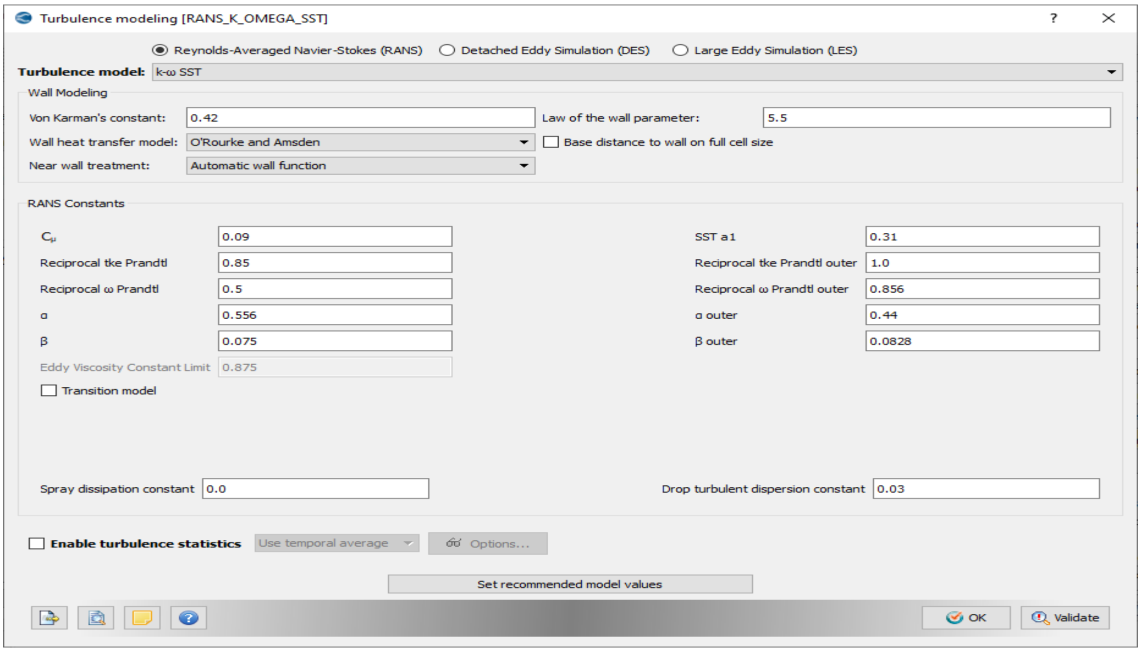
Turbulence modeling [RANS_K_OMEGA_SST]
Wall Modeling
RANS Constants
Set recommended model values
OK
Validate

● Reynolds-Averaged Navier-Stokes (RANS) ○ Detached Eddy Simulation (DES) ○ Large Eddy Simulation (LES)

Turbulence model: k-ω SST

Von Karman's constant: 0.42
Law of the wall parameter: 5.5
Wall heat transfer model: O'Rourke and Amsden
☐ Base distance to wall on full cell size
Near wall treatment: Automatic wall function

C_μ: 0.09
Reciprocal tke Prandtl: 0.85
Reciprocal ω Prandtl: 0.5
α: 0.556
β: 0.075
Eddy Viscosity Constant Limit: 0.875
☐ Transition model
SST a1: 0.31
Reciprocal tke Prandtl outer: 1.0
Reciprocal ω Prandtl outer: 0.856
α outer: 0.44
β outer: 0.0828
Spray dissipation constant: 0.0
Drop turbulent dispersion constant: 0.03

☐ **Enable turbulence statistics** Use temporal average Options...

Figure 55: $k - \omega$ SST model parameters in CONVERGE Studio.

The grid is configured in the *Grid Control* section. Figure 56 shows the configuration of the Base grid, Fix Embedding and Grid scaling.

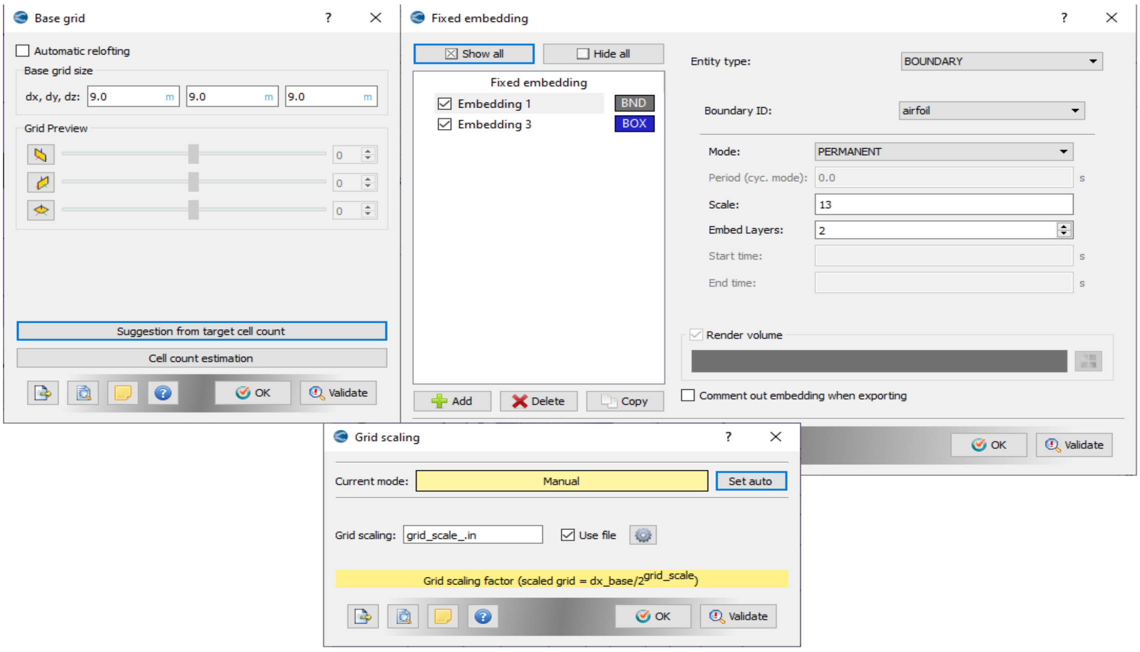
Base grid
Grid Preview
Suggestion from target cell count
Cell count estimation
OK
Validate
Fixed embedding
Show all
Hide all
Add
Delete
Copy
Grid scaling
Set auto

☐ Automatic relofting
Base grid size
dx, dy, dz: 9.0 m 9.0 m 9.0 m

Fixed embedding
☑ Embedding 1 BND
☑ Embedding 3 BOX

Entity type: BOUNDARY
Boundary ID: airfoil
Mode: PERMANENT
Period (cyc. mode): 0.0 s
Scale: 13
Embed Layers: 2
Start time: s
End time: s
☑ Render volume
☐ Comment out embedding when exporting

Current mode: Manual
Grid scaling: grid_scale_.in ☑ Use file
Grid scaling factor (scaled grid = dx_base/2^grid_scale)

Figure 56: Grid control (base grid, fixed embedding and grid scaling) in CONVERGE Studio.

The adaptative mesh refinement used is shown in Figure 57:

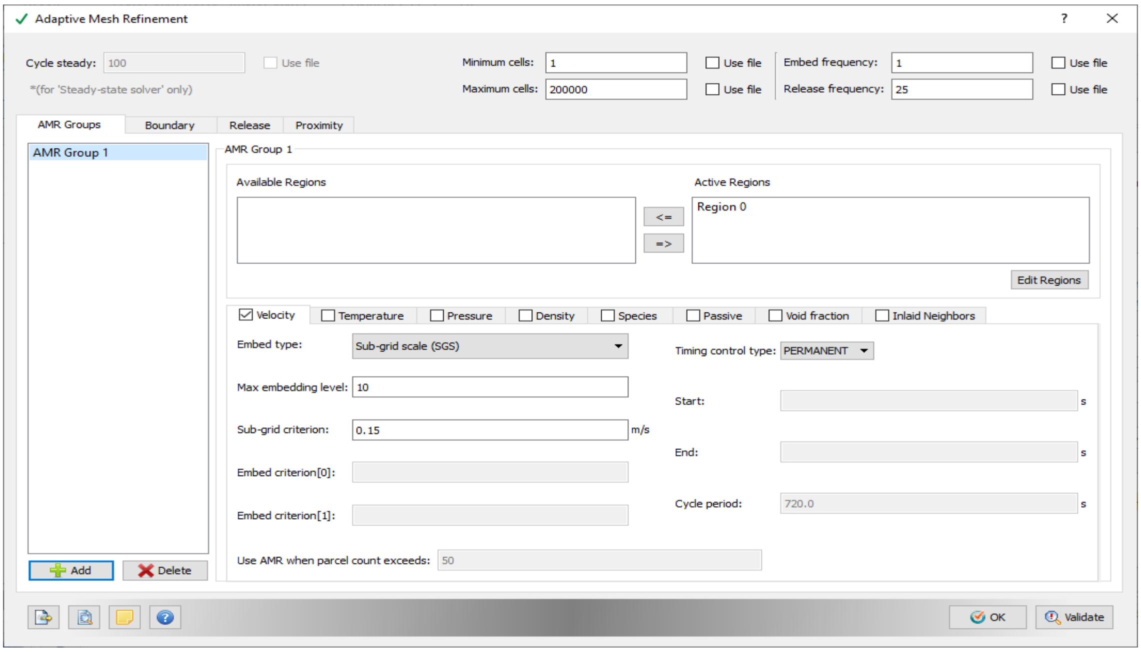
Adaptive Mesh Refinement
AMR Groups
Boundary
Release
Proximity
Add
Delete
OK
Validate
Edit Regions
<=
=>

Cycle steady: 100 ☐ Use file
*(for 'Steady-state solver' only)
Minimum cells: 1 ☐ Use file
Maximum cells: 200000 ☐ Use file
Embed frequency: 1 ☐ Use file
Release frequency: 25 ☐ Use file

AMR Group 1

Available Regions:
Active Regions: Region 0

☑ Velocity ☐ Temperature ☐ Pressure ☐ Density ☐ Species ☐ Passive ☐ Void fraction ☐ Inlaid Neighbors

Embed type: Sub-grid scale (SGS)
Max embedding level: 10
Sub-grid criterion: 0.15 m/s
Embed criterion[0]:
Embed criterion[1]:
Use AMR when parcel count exceeds: 50
Timing control type: PERMANENT
Start: s
End: s
Cycle period: 720.0 s

Figure 57: Grid control (adaptative mesh refinement) in CONVERGE Studio.

Finally, the post variables and outputs of the problem are chosen, Figure 58.

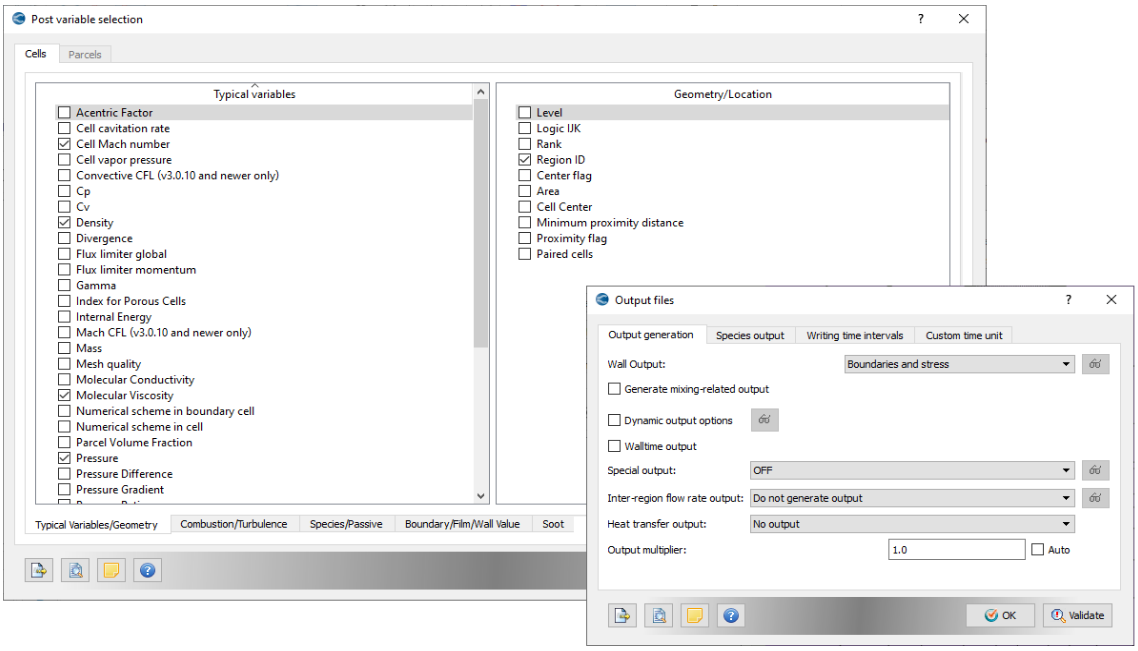
Post variable selection
Cells
Parcels
Typical Variables/Geometry
Combustion/Turbulence
Species/Passive
Boundary/Film/Wall Value
Soot
Output files
Output generation
Species output
Writing time intervals
Custom time unit
OK
Validate

Typical variables
☐ Acentric Factor
☐ Cell cavitation rate
☑ Cell Mach number
☐ Cell vapor pressure
☐ Convective CFL (v3.0.10 and newer only)
☐ Cp
☐ Cv
☑ Density
☐ Divergence
☐ Flux limiter global
☐ Flux limiter momentum
☐ Gamma
☐ Index for Porous Cells
☐ Internal Energy
☐ Mach CFL (v3.0.10 and newer only)
☐ Mass
☐ Mesh quality
☐ Molecular Conductivity
☑ Molecular Viscosity
☐ Numerical scheme in boundary cell
☐ Numerical scheme in cell
☐ Parcel Volume Fraction
☑ Pressure
☐ Pressure Difference
☐ Pressure Gradient

Geometry/Location
☐ Level
☐ Logic IJK
☐ Rank
☑ Region ID
☐ Center flag
☐ Area
☐ Cell Center
☐ Minimum proximity distance
☐ Proximity flag
☐ Paired cells

Wall Output: Boundaries and stress
☐ Generate mixing-related output
☐ Dynamic output options
☐ Walltime output
Special output: OFF
Inter-region flow rate output: Do not generate output
Heat transfer output: No output
Output multiplier: 1.0 ☐ Auto

Figure 58: Post variables and outputs in CONVERGE Studio.

After creating the Case Setup, it is important to perform the final validation that everything is correct, Figure 59. The export of the input files is carried out.

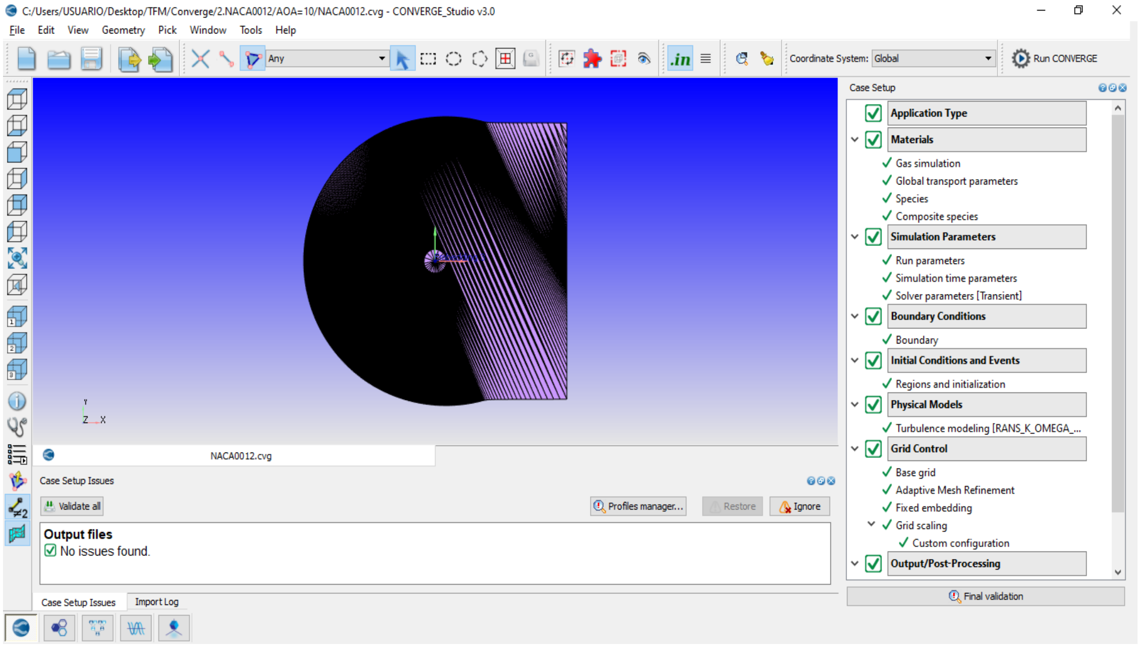
C:/Users/USUARIO/Desktop/TFM/Converge/2.NACA0012/AOA=10/NACA0012.cvg - CONVERGE_Studio v3.0
File Edit View Geometry Pick Window Tools Help
Any
Coordinate System: Global
Run CONVERGE
Case Setup
☑ Application Type
☑ Materials
✓ Gas simulation
✓ Global transport parameters
✓ Species
✓ Composite species
☑ Simulation Parameters
✓ Run parameters
✓ Simulation time parameters
✓ Solver parameters [Transient]
☑ Boundary Conditions
✓ Boundary
☑ Initial Conditions and Events
✓ Regions and initialization
☑ Physical Models
✓ Turbulence modeling [RANS_K_OMEGA_...
☑ Grid Control
✓ Base grid
✓ Adaptive Mesh Refinement
✓ Fixed embedding
✓ Grid scaling
✓ Custom configuration
☑ Output/Post-Processing
Final validation
NACA0012.cvg
Case Setup Issues
Validate all
Profiles manager...
Restore
Ignore
Case Setup Issues
Import Log

Output files
☑ No issues found.

Figure 59: Final validation in CONVERGE Studio.

In case there are problems with the triangles of the geometry, this can be visualised using the *Diagnosis Dock*. Figure 60 is an example where it can be seen that there are no problems with the geometry triangles.

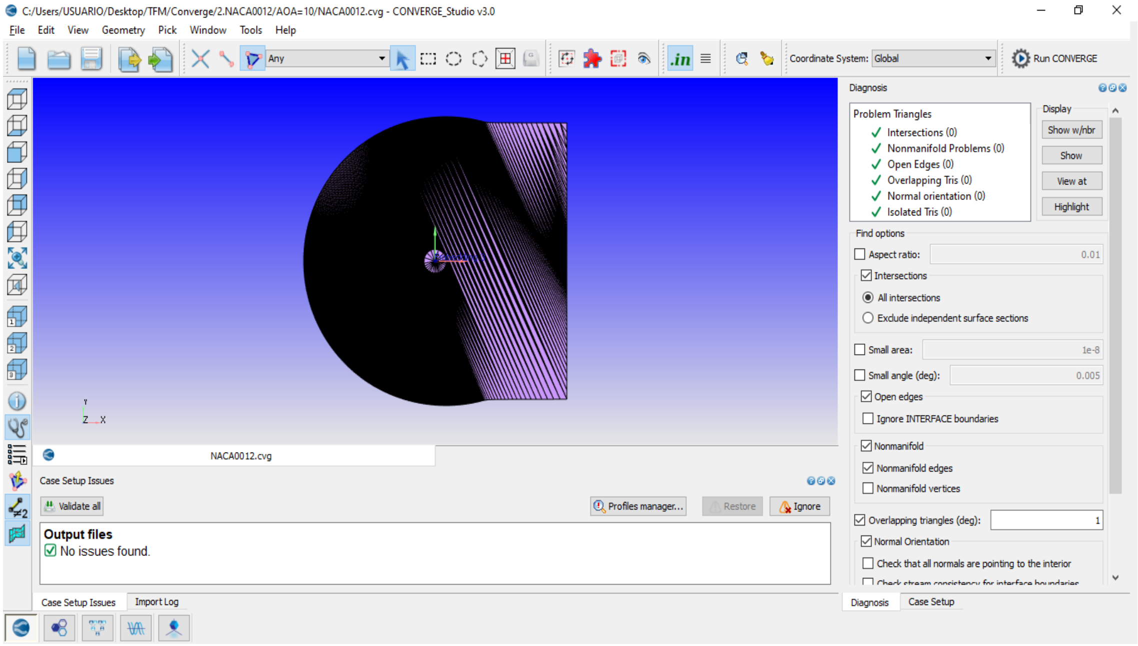
C:/Users/USUARIO/Desktop/TFM/Converge/2.NACA0012/AOA=10/NACA0012.cvg - CONVERGE_Studio v3.0
File Edit View Geometry Pick Window Tools Help
Any
Coordinate System: Global
Run CONVERGE
Diagnosis
Display
Show w/nbr
Show
View at
Highlight
Find options
NACA0012.cvg
Case Setup Issues
Validate all
Profiles manager...
Restore
Ignore
Case Setup Issues
Import Log
Diagnosis
Case Setup

Problem Triangles
✓ Intersections (0)
✓ Nonmanifold Problems (0)
✓ Open Edges (0)
✓ Overlapping Tris (0)
✓ Normal orientation (0)
✓ Isolated Tris (0)

☐ Aspect ratio: 0.01
☑ Intersections
● All intersections
○ Exclude independent surface sections
☐ Small area: 1e-8
☐ Small angle (deg): 0.005
☑ Open edges
☐ Ignore INTERFACE boundaries
☑ Nonmanifold
☑ Nonmanifold edges
☐ Nonmanifold vertices
☑ Overlapping triangles (deg): 1
☑ Normal Orientation
☐ Check that all normals are pointing to the interior

Output files
☑ No issues found.

Figure 60: Use of the *Diagnosis dock*.

To simulate the case, the command window is used. First, run *mpivars.bat* found in the installation folder to run the Intel MPI setup script. Then enter *mpiexec -n <number of processes> converge.exe*, Figure 61.

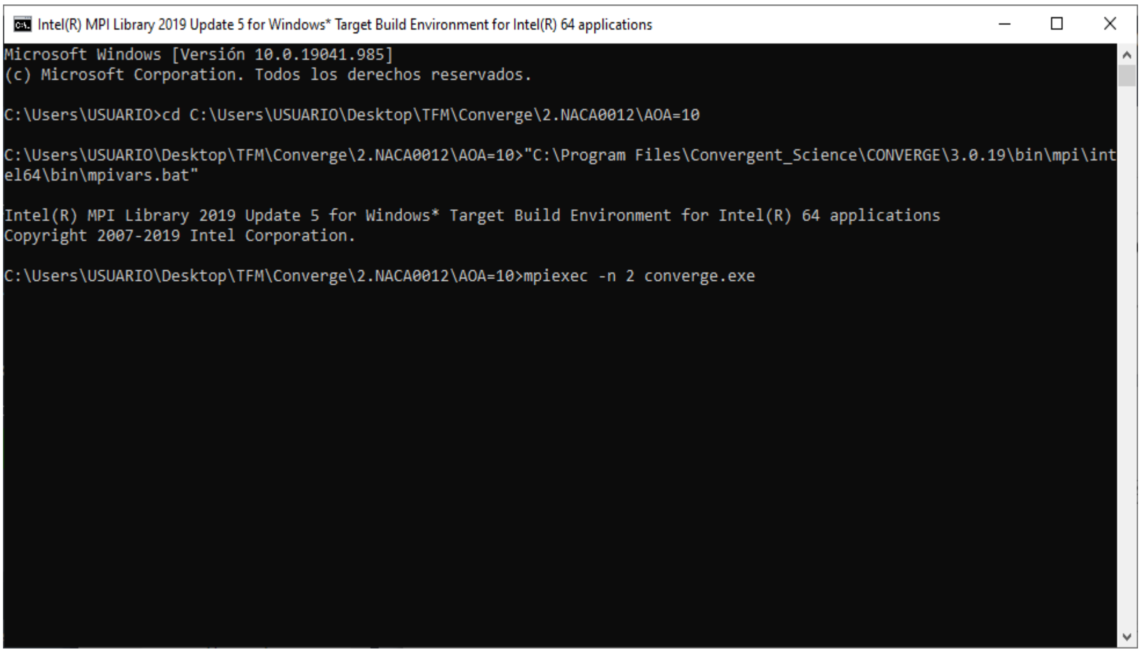

```
Microsoft Windows [Versión 10.0.19041.985]
(c) Microsoft Corporation. Todos los derechos reservados.

C:\Users\USUARIO>cd C:\Users\USUARIO\Desktop\TFM\Converge\2.NACA0012\AOA=10

C:\Users\USUARIO\Desktop\TFM\Converge\2.NACA0012\AOA=10>"C:\Program Files\Convergent_Science\CONVERGE\3.0.19\bin\mpi\int
el64\bin\mpivars.bat"

Intel(R) MPI Library 2019 Update 5 for Windows* Target Build Environment for Intel(R) 64 applications
Copyright 2007-2019 Intel Corporation.

C:\Users\USUARIO\Desktop\TFM\Converge\2.NACA0012\AOA=10>mpiexec -n 2 converge.exe
```

Figure 61: Use of the command window.

After simulating the case you have a series of *.out* files in the working folder. At the bottom of CONVERGE Studio, select the button *Line Plotting*. In this part of the programme, the results obtained can be represented (*.out* files). An example is shown in Figure 62.

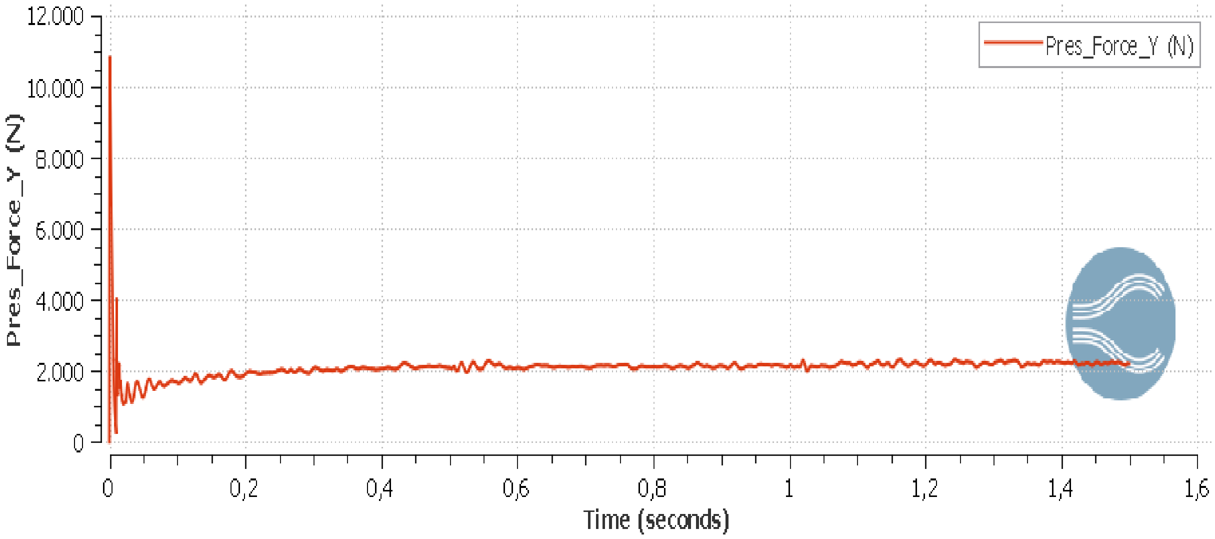

Figure 62: Pressure Forces Y, NACA 0012.

Finally, the post-processing representation of the case is obtained with Tecplot for CONVERGE software. In CONVERGE Studio, choose the button in the bottom window called *Post-Processing 3D*. The folder called Output is selected and the files obtained are converted, Figure 63. You get *.plt* files.

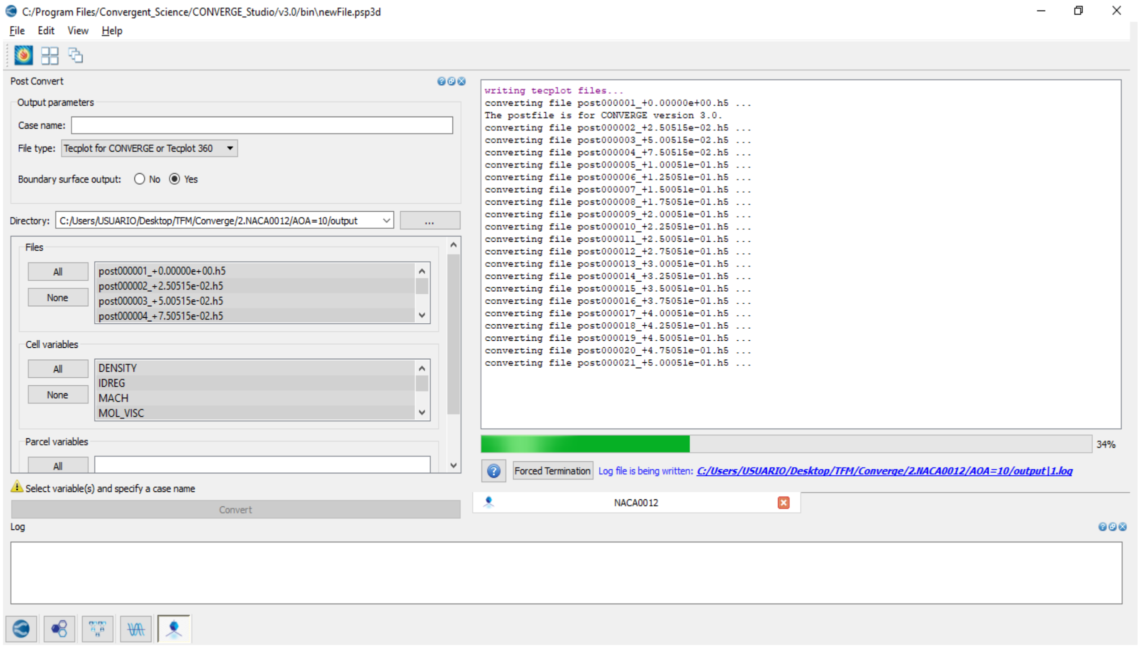

C:/Program Files/Convergent_Science/CONVERGE_Studio/v3.0/bin\newFile.psp3d

Post Convert

Output parameters

Case name:

File type: Tecplot for CONVERGE or Tecplot 360

Boundary surface output: ○ No ● Yes

Directory: C:/Users/USUARIO/Desktop/TFM/Converge/2.NACA0012/AOA=10/output

Files

post000001_+0.00000e+00.h5
post000002_+2.50515e-02.h5
post000003_+5.00515e-02.h5
post000004_+7.50515e-02.h5

Cell variables

DENSITY
IDREG
MACH
MOL_VISC

Parcel variables

⚠ Select variable(s) and specify a case name

```
writing tecplot files...
converting file post000001_+0.00000e+00.h5 ...
The postfile is for CONVERGE version 3.0.
converting file post000002_+2.50515e-02.h5 ...
converting file post000003_+5.00515e-02.h5 ...
converting file post000004_+7.50515e-02.h5 ...
converting file post000005_+1.00051e-01.h5 ...
converting file post000006_+1.25051e-01.h5 ...
converting file post000007_+1.50051e-01.h5 ...
converting file post000008_+1.75051e-01.h5 ...
converting file post000009_+2.00051e-01.h5 ...
converting file post000010_+2.25051e-01.h5 ...
converting file post000011_+2.50051e-01.h5 ...
converting file post000012_+2.75051e-01.h5 ...
converting file post000013_+3.00051e-01.h5 ...
converting file post000014_+3.25051e-01.h5 ...
converting file post000015_+3.50051e-01.h5 ...
converting file post000016_+3.75051e-01.h5 ...
converting file post000017_+4.00051e-01.h5 ...
converting file post000018_+4.25051e-01.h5 ...
converting file post000019_+4.50051e-01.h5 ...
converting file post000020_+4.75051e-01.h5 ...
converting file post000021_+5.00051e-01.h5 ...
```

34%

Log file is being written: C:/Users/USUARIO/Desktop/TFM/Converge/2.NACA0012/AOA=10/output\1.log

File
Edit
View
Help
All
None
All
None
All
Convert
Log
Forced Termination
NACA0012

Figure 63: Obtaining the *.plt* files.

Tecplot for CONVERGE software is used and the previously obtained *.plt* files are plotted. An example is shown in Figure 64.

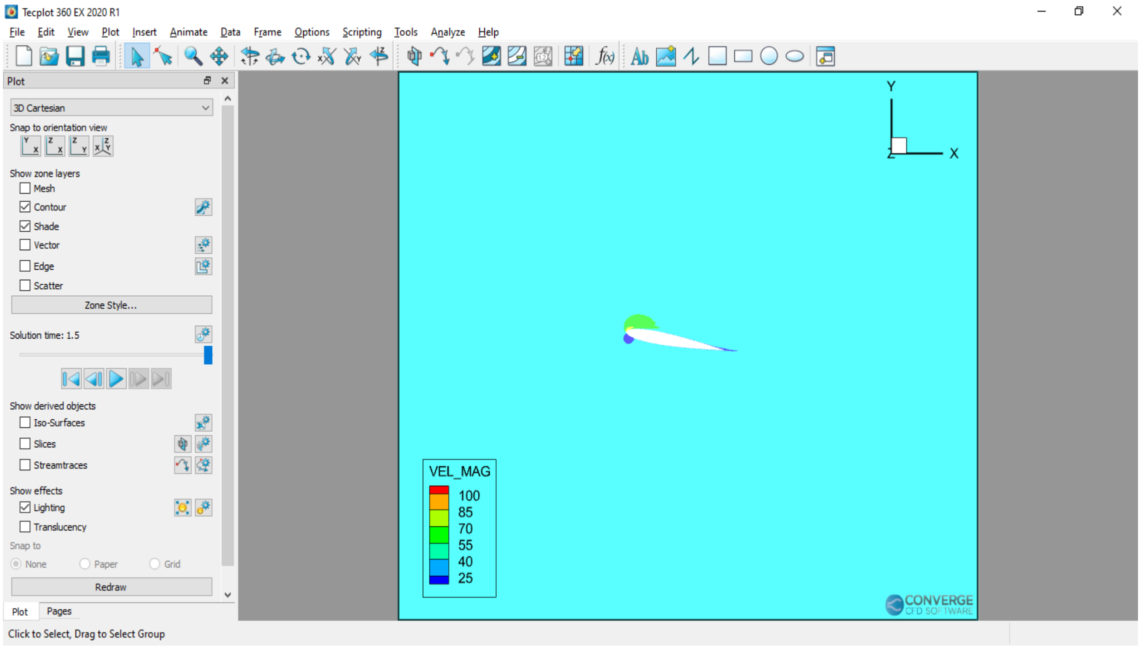

Tecplot 360 EX 2020 R1

Plot

3D Cartesian

Show zone layers
☐ Mesh
☑ Contour
☑ Shade
☐ Vector
☐ Edge
☐ Scatter

Solution time: 1.5

Show derived objects
☐ Iso-Surfaces
☐ Slices
☐ Streamtraces

Show effects
☑ Lighting
☐ Translucency

Snap to
○ None ○ Paper ○ Grid

Click to Select, Drag to Select Group

File
Edit
View
Plot
Insert
Animate
Data
Frame
Options
Scripting
Tools
Analyze
Help
Snap to orientation view
Zone Style...
Redraw
Plot
Pages
Y
X
Z
VEL_MAG
100
85
70
55
40
25
CONVERGE
CFD SOFTWARE

Figure 64: Tecplot software.

FlightStream

Firstly, the CAD file previously created is imported. Catia V5 has been used to obtain the CAD. In Catia V5 the coordinates of the airfoil are imported. Then, the points are joined with splines, the airfoil is projected to 11 meters, which is the wing's span, and finally, the spaces are filled with surfaces. Figure 65 shows the CAD used.

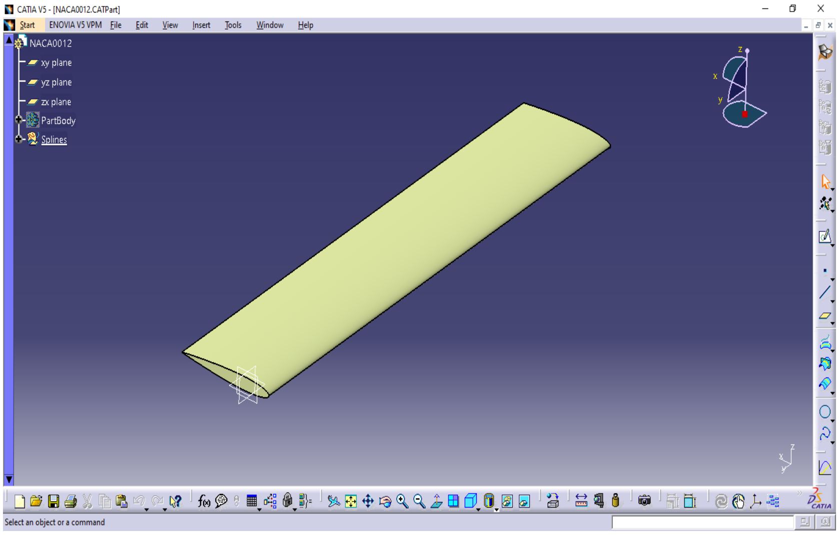
CATIA V5 - [NACA0012.CATPart]
Start
ENOVIA V5 VPM
File
Edit
View
Insert
Tools
Window
Help
NACA0012
xy plane
yz plane
zx plane
PartBody
Splines
x
y
z

Select an object or a command

Figure 65: Wing obtained in CatiaV5.

After importing the CAD file into FlightStream, Figure 66a, each part of the wing is selected (with the *Select faces* button selected), right-click and select: *Retesellate->Trimmed mesher* and a value is typed in *Tessellation edge size*. Figure 66b shows the wing with the modified mesh.

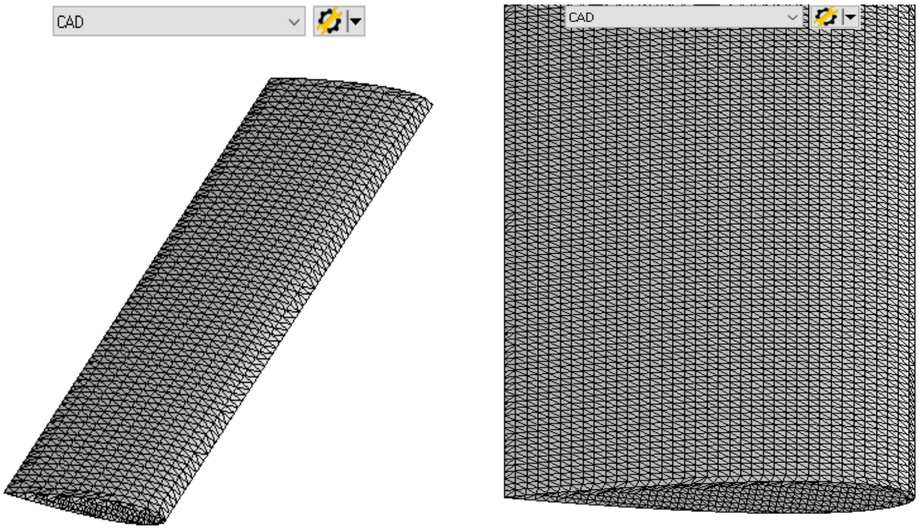

(a) Wing imported. (b) Wing with the modified mesh.

Figure 66: CAD of the wing in FlightStream.

The *Select edges* button is selected and then the edge on the trailing edge of the wing edge too, right-click and select: *Trailing edges->Apply*, Figure 67.

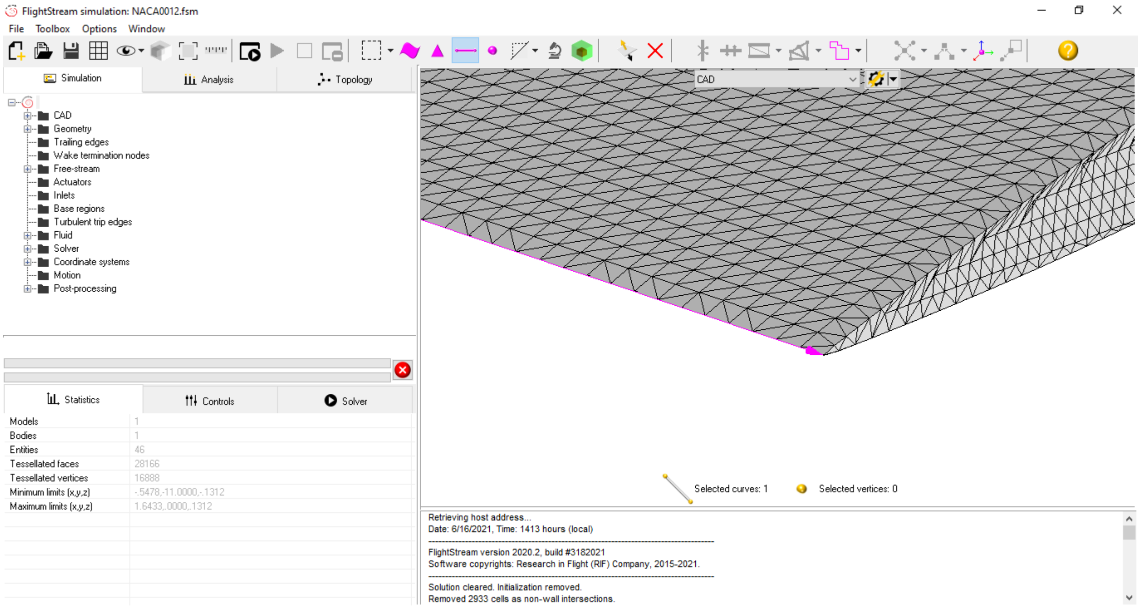
FlightStream simulation: NACA0012.fsm
File
Toolbox
Options
Window
Simulation
Analysis
Topology
CAD
CAD
Geometry
Trailing edges
Wake termination nodes
Free-stream
Actuators
Inlets
Base regions
Turbulent trip edges
Fluid
Solver
Coordinate systems
Motion
Post-processing
Statistics
Controls
Solver
Selected curves: 1
Selected vertices: 0

Models	1
Bodies	1
Entities	46
Tessellated faces	28166
Tessellated vertices	16888
Minimum limits (x,y,z)	-.5478,-11.0000,-.1312
Maximum limits (x,y,z)	1.6433,.0000,.1312

```
Retrieving host address...
Date: 6/16/2021, Time: 1413 hours (local)
------------------------------------------------------------------------
FlightStream version 2020.2, build #3182021
Software copyrights: Research in Flight (RIF) Company, 2015-2021.
------------------------------------------------------------------------
Solution cleared. Initialization removed.
Removed 2933 cells as non-wall intersections.
```

Figure 67: Configuring the trailing edge in FlightStream.

Next, the CAD is converted to geometry by right-clicking on the CAD file name and selecting *Convert to geometry*. The *Select vertices* button is selected and then the point on the trailing edge of the wing edge too, right-click and select: *Wake termination nodes -> Apply*, Figure 68. The same is done with the another edge of the wing.

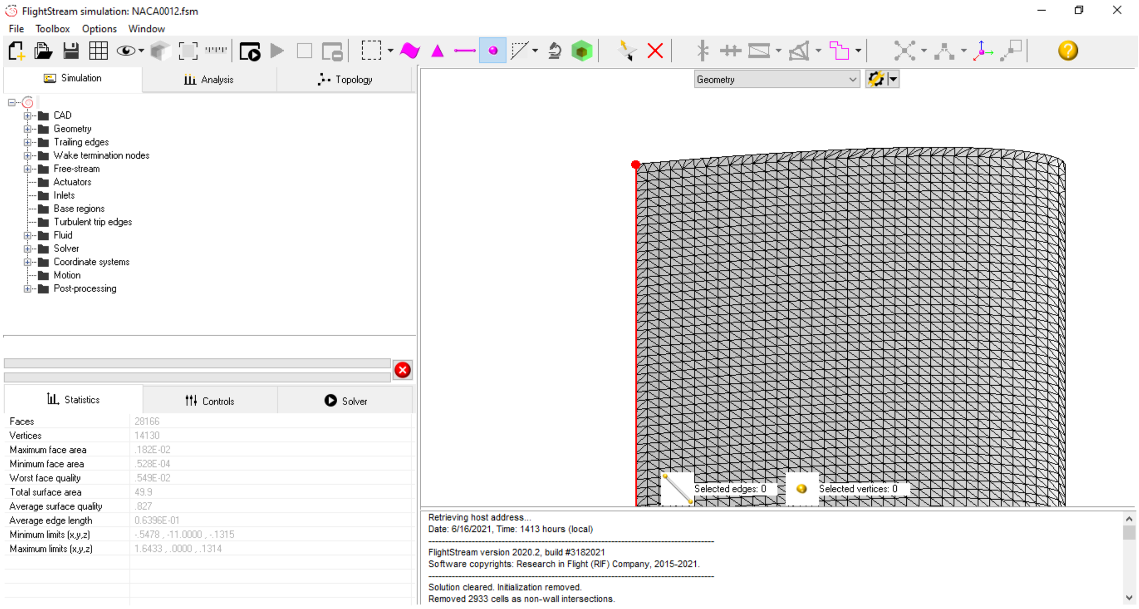
FlightStream simulation: NACA0012.fsm
File
Toolbox
Options
Window
Simulation
Analysis
Topology
Geometry
CAD
Geometry
Trailing edges
Wake termination nodes
Free-stream
Actuators
Inlets
Base regions
Turbulent trip edges
Fluid
Solver
Coordinate systems
Motion
Post-processing
Statistics
Controls
Solver
Selected edges: 0
Selected vertices: 0

Faces	28166
Vertices	14130
Maximum face area	.182E-02
Minimum face area	.528E-04
Worst face quality	.549E-02
Total surface area	49.9
Average surface quality	.827
Average edge length	0.6396E-01
Minimum limits (x,y,z)	-.5478 , -11.0000 , -.1315
Maximum limits (x,y,z)	1.6433 , .0000 , .1314

```
Retrieving host address...
Date: 6/16/2021, Time: 1413 hours (local)
------------------------------------------------------------------------
FlightStream version 2020.2, build #3182021
Software copyrights: Research in Flight (RIF) Company, 2015-2021.
------------------------------------------------------------------------
Solution cleared. Initialization removed.
Removed 2933 cells as non-wall intersections.
```

Figure 68: Configuring wake termination nodes in FlightStream.

The Solver button is selected and the case is configured as shown in Figure 69.

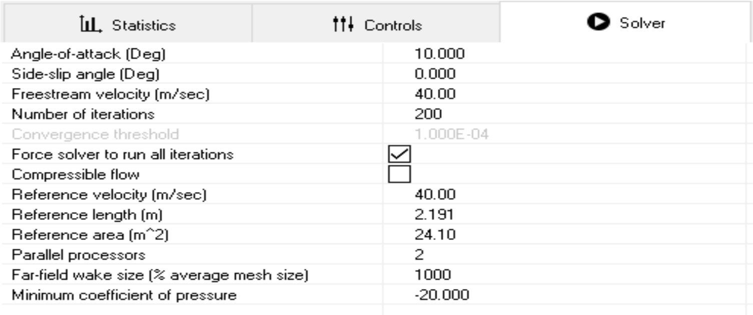

Angle-of-attack (Deg)	10.000
Side-slip angle (Deg)	0.000
Freestream velocity (m/sec)	40.00
Number of iterations	200
Convergence threshold	1.000E-04
Force solver to run all iterations	☑
Compressible flow	☐
Reference velocity (m/sec)	40.00
Reference length (m)	2.191
Reference area (m^2)	24.10
Parallel processors	2
Far-field wake size (% average mesh size)	1000
Minimum coefficient of pressure	-20.000

Figure 69: Case configuration in FlightStream.

A coordinate origin is created in the centre of the wing at $1/4\%c$ of the leading edge. It is also important to ensure that there are not degenerate or overlapping faces or free edges. In *Analysis->Loads* the way to obtain the loads is chosen. Figure 70 shows the way to obtain the loads in this work.

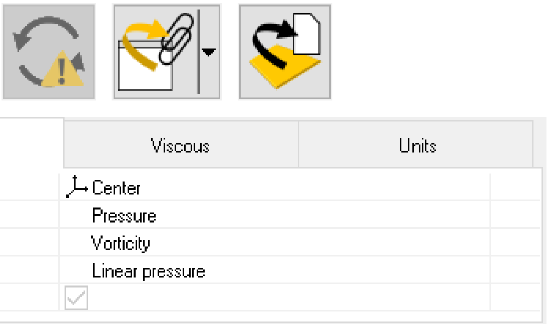

Coordinate system	Center
Lift model	Pressure
Drag model	Vorticity
Moments model	Linear pressure
Symmetry loads	☑

Figure 70: Obtaining loads in FlightStream.

To solve the case, the *Initialize solver* button is selected, the body and the *Initialize* button are selected after, Figure 71. Subsequently, the *play* button is clicked.

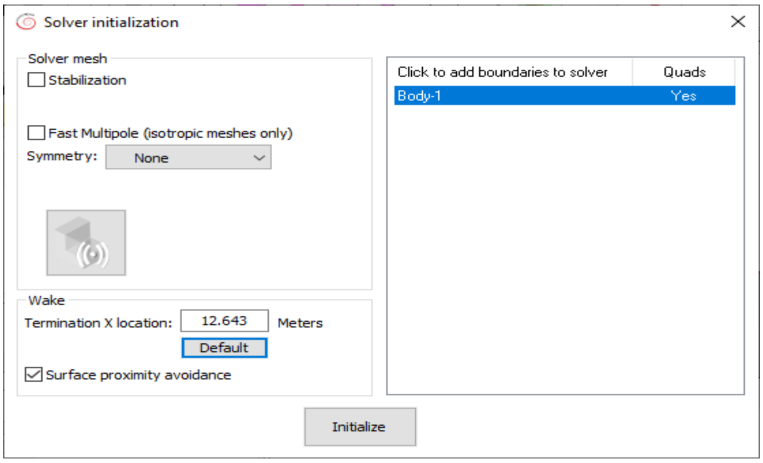

☐ Stabilization

☐ Fast Multipole (isotropic meshes only)

Symmetry: None

Termination X location: 12.643 Meters

☑ Surface proximity avoidance

Click to add boundaries to solver	Quads
Body-1	Yes

Figure 71: Solver initialization in FlightStream.

In Figure 72, the velocity field around the wing for the angle of attack 10° is shown.

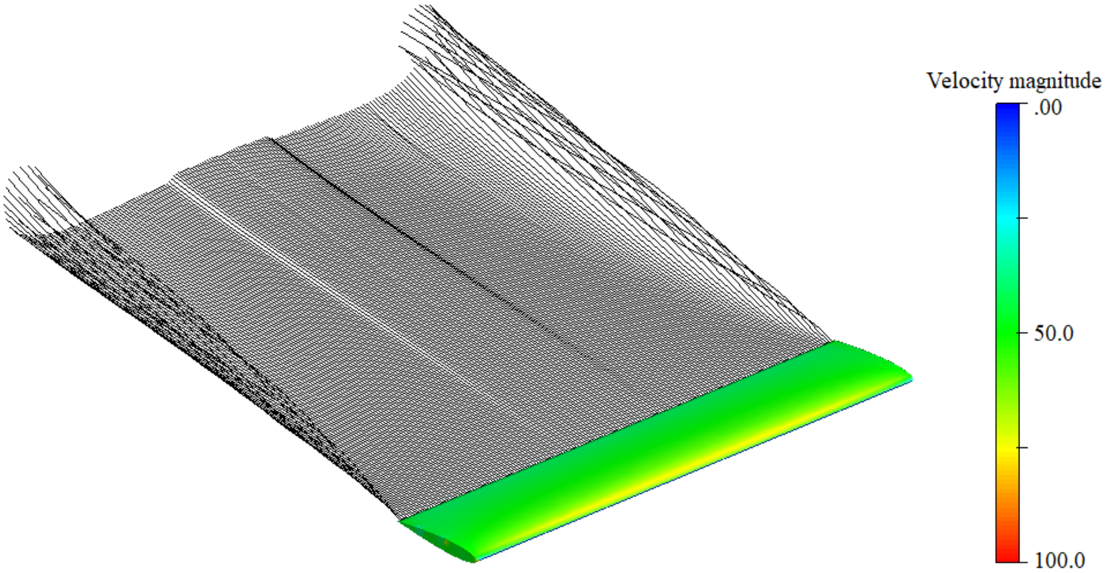
Velocity magnitude
.00
50.0
100.0

Figure 72: Velocity field around the wing for the angle of attack 10° in FlightStream.

Finally, to solve the case for different angles of attack, after having the case initialised, instead of selecting the play it is selected: *Toolbox -> Solver sweeper*, Figure 73. Finally, select *Run the sweep*.

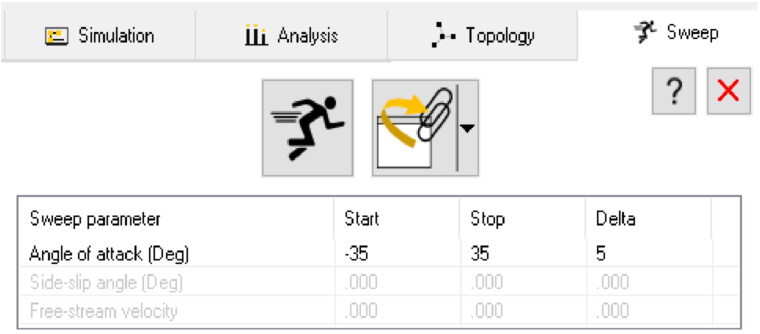
Simulation
Analysis
Topology
Sweep
?
X

Sweep parameter	Start	Stop	Delta
Angle of attack (Deg)	-35	35	5
Side-slip angle (Deg)	.000	.000	.000
Free-stream velocity	.000	.000	.000

Figure 73: Solving the case for different angles of attack in FlightStream.

B Annex B: Coordinates of the airfoil and the high-lift devices

Coordinates of the NACA 0012 airfoil:

x	y
1.643325	0
1.62754908	0.0049738
1.59926198	0.00887396
1.56339367	0.0137382
1.52182851	0.01923786
1.47570585	0.02521956
1.42585833	0.03150802
1.37289944	0.03801559
1.31735505	0.04465462
1.25964148	0.05133747
1.20015311	0.05802033
1.1391748	0.06463745
1.07701329	0.07116693
1.01393153	0.07754303
0.95017052	0.08372193
0.88594937	0.08968172
0.82148721	0.09540049
0.75695932	0.1007906
0.69254098	0.10587395
0.62840748	0.11058482
0.56473411	0.1149232
0.50165235	0.11880144
0.43931555	0.12221956
0.37787711	0.12515563
0.31744657	0.12756584
0.2581554	0.12940637
0.20015699	0.13069912
0.14353896	0.13137836
0.08841089	0.131466
0.03492613	0.13089631
-0.01684956	0.12971312
-0.06680664	0.1278726
-0.11481364	0.12539665
-0.16080483	0.12228529
-0.20464874	0.11853851
-0.24627964	0.11417822
-0.28560989	0.10918251
-0.32252992	0.10361712
-0.3569521	0.09750395
-0.38878878	0.0908211
-0.41797424	0.08363429
-0.44442081	0.07596544
-0.46804087	0.06783646
-0.48874677	0.05926926
-0.50647277	0.05030766
-0.52115314	0.04095166
-0.53270023	0.03122318
-0.54102641	0.02114412
-0.54606594	0.01073639
-0.547775	0
-0.54606594	-0.01073639
-0.54102641	-0.02114412
-0.53270023	-0.03122318
-0.52115314	-0.04095166
-0.50647277	-0.05030766
-0.48874677	-0.05926926
-0.46804087	-0.06783646
-0.44442081	-0.07596544
-0.41797424	-0.08363429
-0.38878878	-0.0908211
-0.3569521	-0.09750395
-0.32252992	-0.10361712
-0.28560989	-0.10918251
-0.24627964	-0.11417822
-0.20464874	-0.11853851
-0.16080483	-0.12228529
-0.11481364	-0.12539665
-0.06680664	-0.1278726
-0.01684956	-0.12971312
0.03492613	-0.13089631
0.08841089	-0.131466
0.14353896	-0.13137836
0.20015699	-0.13069912
0.2581554	-0.12940637
0.31744657	-0.12756584
0.37787711	-0.12515563
0.43931555	-0.12221956
0.50165235	-0.11880144
0.56473411	-0.1149232
0.62840748	-0.11058482
0.69254098	-0.10587395
0.75695932	-0.1007906
0.82148721	-0.09540049
0.88594937	-0.08968172
0.95017052	-0.08372193
1.01393153	-0.07754303
1.07701329	-0.07116693
1.1391748	-0.06463745
1.20015311	-0.05802033
1.25964148	-0.05133747
1.31735505	-0.04465462
1.37289944	-0.03801559
1.42585833	-0.03150802
1.47570585	-0.02521956
1.52182851	-0.01923786
1.56339367	-0.0137382
1.59926198	-0.00887396
1.62754908	-0.0049738

Table 15: Coordinates of the NACA 0012 airfoil.

Coordinates of the NACA 0012 airfoil with a plain flap (20%c 20°):

x	y
1.61690033	-0.1498822
1.60377565	-0.13981409
1.57853417	-0.12647029
1.54647838	-0.10964264
1.50929541	-0.0902295
1.46801509	-0.06884436
1.42331665	-0.04588163
1.37579169	-0.02166998
1.32585652	0.00357149
1.27392745	0.02957985
1.24323014	0.04423831
1.22028932	0.05352857
1.205105	0.05747255
1.20015311	0.05802033
1.1391748	0.06463745
1.07701329	0.07116693
1.01393153	0.07754303
0.95017052	0.08372193
0.88594937	0.08968172
0.82148721	0.09540049
0.75695932	0.1007906
0.69254098	0.10587395
0.62840748	0.11058482
0.56473411	0.1149232
0.50165235	0.11880144
0.43931555	0.12221956
0.37787711	0.12515563
0.31744657	0.12756584
0.2581554	0.12940637
0.20015699	0.13069912
0.14353896	0.13137836
0.08841089	0.131466
0.03492613	0.13089631
-0.01684956	0.12971312
-0.06680664	0.1278726
-0.11481364	0.12539665
-0.16080483	0.12228529
-0.20464874	0.11853851
-0.24627964	0.11417822
-0.28560989	0.10918251
-0.32252992	0.10361712
-0.3569521	0.09750395
-0.38878878	0.0908211
-0.41797424	0.08363429
-0.44442081	0.07596544
-0.46804087	0.06783646
-0.48874677	0.05926926
-0.50647277	0.05030766
-0.52115314	0.04095166
-0.53270023	0.03122318
-0.54102641	0.02114412
-0.54606594	0.01073639
-0.547775	0
-0.54606594	-0.01073639
-0.54102641	-0.02114412
-0.53270023	-0.03122318
-0.52115314	-0.04095166
-0.50647277	-0.05030766
-0.48874677	-0.05926926
-0.46804087	-0.06783646
-0.44442081	-0.07596544
-0.41797424	-0.08363429
-0.38878878	-0.0908211
-0.3569521	-0.09750395
-0.32252992	-0.10361712
-0.28560989	-0.10918251
-0.24627964	-0.11417822
-0.20464874	-0.11853851
-0.16080483	-0.12228529
-0.11481364	-0.12539665
-0.06680664	-0.1278726
-0.01684956	-0.12971312
0.03492613	-0.13089631
0.08841089	-0.131466
0.14353896	-0.13137836
0.20015699	-0.13069912
0.2581554	-0.12940637
0.31744657	-0.12756584
0.37787711	-0.12515563
0.43931555	-0.12221956
0.50165235	-0.11880144
0.56473411	-0.1149232
0.62840748	-0.11058482
0.69254098	-0.10587395
0.75695932	-0.1007906
0.82148721	-0.09540049
0.88594937	-0.08968172
0.95017052	-0.08372193
1.01393153	-0.07754303
1.07701329	-0.07116693
1.1391748	-0.06463745
1.20015311	-0.05802033
1.20146777	-0.05786695
1.23880412	-0.06689428
1.29531259	-0.08034764
1.34978333	-0.09312175
1.40175623	-0.10510707
1.45074922	-0.11625977
1.49614881	-0.12640456
1.53707856	-0.13543189
1.57246483	-0.14314456
1.60037944	-0.14914818

Table 16: Coordinates of the NACA 0012 airfoil with a plain flap (20%c 20°).

Coordinates of the NACA 0012 airfoil with a plain flap (30%c 15°):

x	y
1.620921	-0.1675096
1.60697465	-0.16124305
1.58065954	-0.15015608
1.54726718	-0.13617687
1.50855044	-0.12009419
1.46553915	-0.1023901
1.41902209	-0.08339327
1.36956897	-0.06341043
1.31761799	-0.04263881
1.26360737	-0.02123176
1.20786579	0.00061351
1.15067808	0.02280935
1.09232908	0.04518048
1.03303792	0.06766117
1.01518045	0.07386198
0.99951409	0.07804698
0.985995	0.08023808
0.95017052	0.08372193
0.88594937	0.08968172
0.82148721	0.09540049
0.75695932	0.1007906
0.69254098	0.10587395
0.62840748	0.11058482
0.56473411	0.1149232
0.50165235	0.11880144
0.43931555	0.12221956
0.37787711	0.12515563
0.31744657	0.12756584
0.2581554	0.12940637
0.20015699	0.13069912
0.14353896	0.13137836
0.08841089	0.131466
0.03492613	0.13089631
-0.01684956	0.12971312
-0.06680664	0.1278726
-0.11481364	0.12539665
-0.16080483	0.12228529
-0.20464874	0.11853851
-0.24627964	0.11417822
-0.28560989	0.10918251
-0.32252992	0.10361712
-0.3569521	0.09750395
-0.38878878	0.0908211
-0.41797424	0.08363429
-0.44442081	0.07596544
-0.46804087	0.06783646
-0.48874677	0.05926926
-0.50647277	0.05030766
-0.52115314	0.04095166
-0.53270023	0.03122318
-0.54102641	0.02114412
-0.54606594	0.01073639
-0.547775	0
-0.54606594	-0.01073639
-0.54102641	-0.02114412
-0.53270023	-0.03122318
-0.52115314	-0.04095166
-0.50647277	-0.05030766
-0.48874677	-0.05926926
-0.46804087	-0.06783646
-0.44442081	-0.07596544
-0.41797424	-0.08363429
-0.38878878	-0.0908211
-0.3569521	-0.09750395
-0.32252992	-0.10361712
-0.28560989	-0.10918251
-0.24627964	-0.11417822
-0.20464874	-0.11853851
-0.16080483	-0.12228529
-0.11481364	-0.12539665
-0.06680664	-0.1278726
-0.01684956	-0.12971312
0.03492613	-0.13089631
0.08841089	-0.131466
0.14353896	-0.13137836
0.20015699	-0.13069912
0.2581554	-0.12940637
0.31744657	-0.12756584
0.37787711	-0.12515563
0.43931555	-0.12221956
0.50165235	-0.11880144
0.56473411	-0.1149232
0.62840748	-0.11058482
0.69254098	-0.10587395
0.75695932	-0.1007906
0.82148721	-0.09540049
0.88594937	-0.08968172
0.95017052	-0.08372193
0.98323421	-0.08052293
0.99291888	-0.08212243
1.05549669	-0.09228913
1.11721998	-0.10208335
1.17782581	-0.11148317
1.23702933	-0.12042286
1.29450188	-0.12890241
1.34987098	-0.13687802
1.40272031	-0.14428394
1.4525021	-0.15109826
1.49858093	-0.15727716
1.54016801	-0.16271109
1.57608014	-0.16729049
1.60441106	-0.17084007

Table 17: Coordinates of the NACA 0012 airfoil with a plain flap (30%c 15°).

Coordinates of the NACA 0012 airfoil with a plain flap (40%c 10°):

x	y
1.63000311	-0.15219381
1.61534465	-0.14456878
1.5881531	-0.13580438
1.55366519	-0.12478315
1.51369952	-0.1121405
1.46930784	-0.09824892
1.42132275	-0.08339327
1.37029203	-0.06779263
1.31676346	-0.05162232
1.26108761	-0.03501378
1.20363696	-0.01809849
1.1447402	-0.000986
1.08466023	0.01623605
1.0236381	0.0334581
0.96191481	0.05061441
0.89970948	0.06763926
0.83721931	0.08446691
0.8063248	0.09239869
0.78290194	0.09754777
0.766885	0.09995798
0.75695932	0.1007906
0.69254098	0.10587395
0.62840748	0.11058482
0.56473411	0.1149232
0.50165235	0.11880144
0.43931555	0.12221956
0.37787711	0.12515563
0.31744657	0.12756584
0.2581554	0.12940637
0.20015699	0.13069912
0.14353896	0.13137836
0.08841089	0.131466
0.03492613	0.13089631
-0.01684956	0.12971312
-0.06680664	0.1278726
-0.11481364	0.12539665
-0.16080483	0.12228529
-0.20464874	0.11853851
-0.24627964	0.11417822
-0.28560989	0.10918251
-0.32252992	0.10361712
-0.3569521	0.09750395
-0.38878878	0.0908211
-0.41797424	0.08363429
-0.44442081	0.07596544
-0.46804087	0.06783646
-0.48874677	0.05926926
-0.50647277	0.05030766
-0.52115314	0.04095166
-0.53270023	0.03122318
-0.54102641	0.02114412
-0.54606594	0.01073639
-0.547775	0
-0.54606594	-0.01073639
-0.54102641	-0.02114412
-0.53270023	-0.03122318
-0.52115314	-0.04095166
-0.50647277	-0.05030766
-0.48874677	-0.05926926
-0.46804087	-0.06783646
-0.44442081	-0.07596544
-0.41797424	-0.08363429
-0.38878878	-0.0908211
-0.3569521	-0.09750395
-0.32252992	-0.10361712
-0.28560989	-0.10918251
-0.24627964	-0.11417822
-0.20464874	-0.11853851
-0.16080483	-0.12228529
-0.11481364	-0.12539665
-0.06680664	-0.1278726
-0.01684956	-0.12971312
0.03492613	-0.13089631
0.08841089	-0.131466
0.14353896	-0.13137836
0.20015699	-0.13069912
0.2581554	-0.12940637
0.31744657	-0.12756584
0.37787711	-0.12515563
0.43931555	-0.12221956
0.50165235	-0.11880144
0.56473411	-0.1149232
0.62840748	-0.11058482
0.69254098	-0.10587395
0.75695932	-0.1007906
0.76651251	-0.1000018
0.80408988	-0.10341992
0.86857395	-0.10900723
0.93283891	-0.11428778
0.99670948	-0.11926157
1.05994463	-0.12392862
1.12228142	-0.12831082
1.18347884	-0.13238626
1.24325205	-0.13613304
1.30125047	-0.13957307
1.35710161	-0.14268443
1.41036725	-0.14546713
1.46056535	-0.14792116
1.50701667	-0.15004653
1.5489105	-0.15184323
1.58508556	-0.15326745
1.61361368	-0.15434108

Table 18: Coordinates of the NACA 0012 airfoil with a plain flap (40%c 10°).

Coordinates of the NACA 0012 airfoil with a leading edge flap (15%c 20°) and a plain flap (20%c 20°):

x	y
1.6169	-0.149882
1.60377565	-0.13981409
1.57853417	-0.12647029
1.54647838	-0.10964264
1.50929541	-0.0902295
1.46801509	-0.06884436
1.42331665	-0.04588163
1.37579169	-0.02166998
1.32585652	0.00357149
1.27392745	0.02957985
1.24323014	0.04423831
1.22028932	0.05352857
1.205105	0.05747255
1.20015311	0.05802033
1.1391748	0.06463745
1.07701329	0.07116693
1.01393153	0.07754303
0.95017052	0.08372193
0.88594937	0.08968172
0.82148721	0.09540049
0.75695932	0.1007906
0.69254098	0.10587395
0.62840748	0.11058482
0.56473411	0.1149232
0.50165235	0.11880144
0.43931555	0.12221956
0.37787711	0.12515563
0.31744657	0.12756584
0.2581554	0.12940637
0.20015699	0.13069912
0.14353896	0.13137836
0.08841089	0.131466
0.03492613	0.13089631
-0.01684956	0.12971312
-0.06680664	0.1278726
-0.11481364	0.12539665
-0.16080483	0.12228529
-0.20464874	0.11853851
-0.21911	0.11702665
-0.24167833	0.11327987
-0.26321684	0.10694759
-0.28370363	0.09798599
-0.31893652	0.0798656
-0.35173728	0.06200813
-0.38197446	0.04447933
-0.40962615	0.02732302
-0.43458277	0.01058301
-0.45682244	-0.00567495
-0.47623559	-0.02138514
-0.49275648	-0.03652564
-0.50636321	-0.05103072
-0.51694622	-0.06483465
-0.5244617	-0.07791552
-0.5288439	-0.0902295
-0.53002709	-0.10173277
-0.52794555	-0.11240343
-0.52268691	-0.1219128
-0.51438264	-0.12997605
-0.50309847	-0.13659317
-0.48894397	-0.14178608
-0.47194103	-0.14555477
-0.45222113	-0.14792116
-0.42982809	-0.14888525
-0.40484955	-0.14844703
-0.37737315	-0.1466065
-0.34748655	-0.14338558
-0.31527738	-0.13876236
-0.28083329	-0.13273684
-0.24424192	-0.12535283
-0.21120013	-0.11785927
-0.20464874	-0.11853851
-0.16080483	-0.12228529
-0.11481364	-0.12539665
-0.06680664	-0.1278726
-0.01684956	-0.12971312
0.03492613	-0.13089631
0.08841089	-0.131466
0.14353896	-0.13137836
0.20015699	-0.13069912
0.2581554	-0.12940637
0.31744657	-0.12756584
0.37787711	-0.12515563
0.43931555	-0.12221956
0.50165235	-0.11880144
0.56473411	-0.1149232
0.62840748	-0.11058482
0.69254098	-0.10587395
0.75695932	-0.1007906
0.82148721	-0.09540049
0.88594937	-0.08968172
0.95017052	-0.08372193
1.01393153	-0.07754303
1.07701329	-0.07116693
1.1391748	-0.06463745
1.20015311	-0.05802033
1.20146777	-0.05786695
1.23880412	-0.06689428
1.29531259	-0.08034764
1.34978333	-0.09312175
1.40175623	-0.10510707
1.45074922	-0.11625977
1.49614881	-0.12640456
1.53707856	-0.13543189
1.57246483	-0.14314456
1.60037944	-0.14914818

Table 19: Coordinates of the NACA 0012 airfoil with a leading edge flap (15%c 20°) and a plain flap (20%c 20°).

Coordinates of the NACA 0012 airfoil with a leading edge flap (20%c 15°) and a plain flap (20%c 20°):

x	y
1.6169	-0.149882
1.60377565	-0.13981409
1.57853417	-0.12647029
1.54647838	-0.10964264
1.50929541	-0.0902295
1.46801509	-0.06884436
1.42331665	-0.04588163
1.37579169	-0.02166998
1.32585652	0.00357149
1.27392745	0.02957985
1.24323014	0.04423831
1.22028932	0.05352857
1.205105	0.05747255
1.20015311	0.05802033
1.1391748	0.06463745
1.07701329	0.07116693
1.01393153	0.07754303
0.95017052	0.08372193
0.88594937	0.08968172
0.82148721	0.09540049
0.75695932	0.1007906
0.69254098	0.10587395
0.62840748	0.11058482
0.56473411	0.1149232
0.50165235	0.11880144
0.43931555	0.12221956
0.37787711	0.12515563
0.31744657	0.12756584
0.2581554	0.12940637
0.20015699	0.13069912
0.14353896	0.13137836
0.08841089	0.131466
0.03492613	0.13089631
-0.01684956	0.12971312
-0.06680664	0.1278726
-0.109555	0.1256815
-0.12432301	0.12447639
-0.13685611	0.1225044
-0.14708854	0.11976553
-0.19069143	0.10486605
-0.23208131	0.08987892
-0.27117054	0.0748918
-0.30787146	0.05990467
-0.34207453	0.04498328
-0.37375784	0.03014954
-0.40278991	0.01546917
-0.42912694	0.00096408
-0.45268126	-0.01327807
-0.47338716	-0.02725728
-0.49117889	-0.04088593
-0.50596881	-0.05414208
-0.51773502	-0.06698193
-0.52634604	-0.07936164
-0.53180188	-0.0912374
-0.53397107	-0.10260921
-0.53285361	-0.11341134
-0.52842759	-0.12335893
-0.52084638	-0.13210142
-0.51019764	-0.13968263
-0.49652517	-0.14608064
-0.47993854	-0.15131737
-0.46048158	-0.15539281
-0.43826382	-0.15830698
-0.41335102	-0.16005986
-0.3858308	-0.16060763
-0.35576891	-0.15999412
-0.32327489	-0.15819742
-0.2884364	-0.15521752
-0.25134108	-0.15103252
-0.21207657	-0.14566433
-0.17073051	-0.13911294
-0.12739055	-0.13137836
-0.10070296	-0.12614163
-0.06680664	-0.1278726
-0.01684956	-0.12971312
0.03492613	-0.13089631
0.08841089	-0.131466
0.14353896	-0.13137836
0.20015699	-0.13069912
0.2581554	-0.12940637
0.31744657	-0.12756584
0.37787711	-0.12515563
0.43931555	-0.12221956
0.50165235	-0.11880144
0.56473411	-0.1149232
0.62840748	-0.11058482
0.69254098	-0.10587395
0.75695932	-0.1007906
0.82148721	-0.09540049
0.88594937	-0.08968172
0.95017052	-0.08372193
1.01393153	-0.07754303
1.07701329	-0.07116693
1.1391748	-0.06463745
1.20015311	-0.05802033
1.20146777	-0.05786695
1.23880412	-0.06689428
1.29531259	-0.08034764
1.34978333	-0.09312175
1.40175623	-0.10510707
1.45074922	-0.11625977
1.49614881	-0.12640456
1.53707856	-0.13543189
1.57246483	-0.14314456
1.60037944	-0.14914818

Table 20: Coordinates of the NACA 0012 airfoil with a leading edge flap (20%c 15°) and a plain flap (20%c 20°).

Coordinates of the NACA 0012 airfoil with a leading edge flap (25%c 10°) and a plain flap (20%c 20°):

x	y
1.6169	-0.149882
1.60377565	-0.13981409
1.57853417	-0.12647029
1.54647838	-0.10964264
1.50929541	-0.0902295
1.46801509	-0.06884436
1.42331665	-0.04588163
1.37579169	-0.02166998
1.32585652	0.00357149
1.27392745	0.02957985
1.24323014	0.04423831
1.22028932	0.05352857
1.205105	0.05747255
1.20015311	0.05802033
1.1391748	0.06463745
1.07701329	0.07116693
1.01393153	0.07754303
0.95017052	0.08372193
0.88594937	0.08968172
0.82148721	0.09540049
0.75695932	0.1007906
0.69254098	0.10587395
0.62840748	0.11058482
0.56473411	0.1149232
0.50165235	0.11880144
0.43931555	0.12221956
0.37787711	0.12515563
0.31744657	0.12756584
0.2581554	0.12940637
0.20015699	0.13069912
0.14353896	0.13137836
0.08841089	0.131466
0.03492613	0.13089631
0	0.13010752
-0.0115471	0.12934063
-0.02458414	0.12758775
-0.03913305	0.12482697
-0.08799458	0.1143316
-0.13484029	0.1035733
-0.17958256	0.09250824
-0.22213372	0.08120217
-0.26236231	0.06967698
-0.30022452	0.05793268
-0.33561079	0.04605692
-0.36845538	0.03402778
-0.39864873	0.02193291
-0.42614704	0.00979422
-0.45086265	-0.00236639
-0.47270791	-0.01446126
-0.49161711	-0.0264904
-0.50752449	-0.03840998
-0.52034243	-0.05017619
-0.53002709	-0.0617452
-0.53646892	-0.07311701
-0.53964602	-0.0842478
-0.53944882	-0.09511565
-0.53592115	-0.10541382
-0.52912874	-0.11476982
-0.51918115	-0.12324938
-0.50612219	-0.13080867
-0.49006143	-0.13749153
-0.47104268	-0.14323221
-0.44915359	-0.14807454
-0.4244818	-0.15199661
-0.39711496	-0.15495459
-0.36711881	-0.1569704
-0.33460288	-0.15800022
-0.29963293	-0.15806595
-0.26229658	-0.15712378
-0.22272532	-0.15519561
-0.18096295	-0.15228145
-0.13711904	-0.14835938
-0.09130314	-0.14342941
-0.04358098	-0.13753535
0.00591597	-0.1306772
0.00839191	-0.13030472
0.03492613	-0.13089631
0.08841089	-0.131466
0.14353896	-0.13137836
0.20015699	-0.13069912
0.2581554	-0.12940637
0.31744657	-0.12756584
0.37787711	-0.12515563
0.43931555	-0.12221956
0.50165235	-0.11880144
0.56473411	-0.1149232
0.62840748	-0.11058482
0.69254098	-0.10587395
0.75695932	-0.1007906
0.82148721	-0.09540049
0.88594937	-0.08968172
0.95017052	-0.08372193
1.01393153	-0.07754303
1.07701329	-0.07116693
1.1391748	-0.06463745
1.20015311	-0.05802033
1.20146777	-0.05786695
1.23880412	-0.06689428
1.29531259	-0.08034764
1.34978333	-0.09312175
1.40175623	-0.10510707
1.45074922	-0.11625977
1.49614881	-0.12640456
1.53707856	-0.13543189
1.57246483	-0.14314456
1.60037944	-0.14914818

Table 21: Coordinates of the NACA 0012 airfoil with a leading edge flap (25%c 10°) and a plain flap (20%c 20°).